Structural Study of Heterogeneous States in Lead-free NBT-based Single Crystals

Chengtao Luo

Dissertation submitted to the faculty of the

Virginia Polytechnic Institute and Sate University

In partial fulfillment of the requirement for the degree of

Doctor of Philosophy

in

Materials Science and Engineering

Dwight D Viehland, Chair

Jie-Fang Li

William T Reynolds

Guo-Quan Lu

11/10/2016

Blacksburg, Virginia

Keywords: lead-free ferroelectrics, single crystal, heterogeneous structure, x-ray diffraction, neutron inelastic scattering, diffuse scattering, transmission electron microscopy, polar nanoregion

Structural Study of Heterogeneous States in Lead-free NBT-based Single Crystals

Chengtao Luo

ABSTRACT

Growing environmental concerns now are requiring industries to develop non-lead-based compositions of ferroelectric and piezoelectric materials. These materials—now widely used in sensors, actuators, and transducers—are for the most part lead-based compounds such as $Pb(Zr,Ti)O_3$ (PZT). Indeed, PZT represents the dominant market share for use in these technologies. Moreover, next generation compounds, which include $Pb(Mg_{1/3}Nb_{2/3})O_3$-xat%$PbTiO_3$ (PMN-x%PT) crystals with ultrahigh piezo-/electromechanical properties, are also Pb-based systems and thus are problematic for meeting more restrictive environmental standards. As alternative, Pb-free ferroelectrics such as $(Na_{1/2}Bi_{1/2})TiO_3$ (NBT) -derived single crystals represent viable next-generation materials for use in ferro-/piezoelectric applications. Development of these types of NBT-based crystals has made important advancements in the last decade. In fact, the performances of NBT-based materials are beginning to approach the properties of the widely used commercial PZT ceramic material. Nonetheless, additional studies are needed before it being able to compete with PMN-x%PT and PZN-x%PT crystals in next-generation applications.

As a new type of piezoelectric material, much remains to be learned about Pb-free piezoelectric crystals. For instance, in addition to enhancing our understanding the nature of the piezoelectric third-rank tensor coefficients such as d_{33} and d_{15}, a thorough knowledge of the Curie temperature, leakage current, and electromechanical properties is also essential for increasing the applications potential of these crystals. As detailed herein, multiple dopants

may have to be incorporated into NBT to modify its microstructure and properties to meet these specific requirements, which may further complicate its chemical structure-property relationships.

This study, therefore, was designed to investigate the heterogeneous structure of NBT-based single crystals, using x-ray diffraction, transmission electron microscopy, and neutron inelastic scattering, with the goal of investigating the mechanism coupling of morphotropic phase boundary (MPB) and the maximum property responses in A-site disordered perovskite Pb-free piezoelectric systems. Using the framework of polar nanoregions and adaptive phase theory, I sought to determine how the nanostructure of these single crystals change with temperature and composition—and how these factors impact its properties. Diffuse scattering, domain morphology, and phonon dispersions were used to investigate both the static and dynamic properties of these heterogeneous structures.

Structural Study of Heterogeneous States in Lead-free NBT-based Single Crystals

Chengtao Luo

GENERAL AUDIENCE ABSTRACT

Growing environmental concerns, coupled with increasing regulatory restrictions, are requiring industries to develop non-lead-based compositions of ferroelectric and piezoelectric materials. These materials—now widely used in sensors, actuators, and transducers—are for the most part lead-based compounds such as $Pb(Zr,Ti)O_3$ (PZT). Indeed, PZT represents the dominant market share for use in these technologies. Moreover, next generation compounds, which include $Pb(Mg_{1/3}Nb_{2/3})O_3$-xat%$PbTiO_3$ (PMN-x%PT) crystals with ultrahigh piezo-/electromechanical properties, are also Pb-based systems and thus are problematic for meeting more restrictive environmental standards. As alternative, Pb-free ferroelectrics such as $(Na_{1/2}Bi_{1/2})TiO_3$ (NBT) -derived single crystals represent viable next-generation materials for use in ferro-/piezoelectric applications. Development of these types of NBT-based crystals has made important advancements in the last decade. In fact, the performances of NBT-based materials are beginning to approach the properties of the widely used commercial PZT ceramic material. Nonetheless, additional studies are needed before it being able to compete with PMN-x%PT and PZN-x%PT crystals in next-generation applications.

As a new type of piezoelectric material, much remains to be learned about Pb-free piezoelectric single crystals. In addition to enhancing our understanding the nature of the piezoelectric properties, increasing the applications potential of these crystals is also essential. And these specific requirements from different applications further push the researchers to

find a more effective model to lead the piezoelectric single crystals growth as well as developments.

This study, therefore, was designed to investigate the unique microstructure of NBT-based single crystals, using x-ray diffraction, transmission electron microscopy, and neutron inelastic scattering, with the goal of investigating the mechanism coupling between the chemical compositions and the maximum property responses in these specific Pb-free piezoelectric systems. Using the framework of an advanced microstructure description model, I sought to determine how the nanostructure of these single crystals change with temperature and composition—and how these factors impact its properties. The results from different experiment methods also successfully supported each other and brought new perspectives to the Pb-free material researches.

ACKNOWLEDGEMENT

First, I would like to express my sincerest thanks and gratitude to my advisor, Prof. Dwight Viehland, for providing the opportunity to begin my career as a scientist under his guidance. When we first met during a summer internship as an undergraduate student in 2008, I was immediately impressed by his scientific knowledge and passion for research. Now that I am completing my Ph.D. research, I have nothing but praise for his guidance and encouragement throughout these past five years. As a foreign student at Virginia Tech, his patience and wisdom were instrumental in helping me adjust to this new research environment. In particular, I would like to sincerely thank him for his thorough instruction on experiments, correcting my papers, and helping me practice my presentations. I know I will continue to learn from him throughout my future career.

I would also like to acknowledge the assistance of Prof. Jie-Fang Li, who was so supportive throughout my PhD studies. Her insightful professional advice and guidance was essential to my success. She helped me and many other Chinese students to communicate with Prof. Viehland more effectively, as well as provided amazing technical guidance through her rich experiences in research. I also credit Prof. Li for her constant day-day-day support, and for fostering a warm and accepting academic environment in our group.

I would also like to thank my other committee members, Prof. William Reynolds and Prof. Guo-Quan Lu, for their invaluable suggestions and creative inspiration for my research.

My gratitude also goes to Dr. Wenwei Ge for his insightful guidance with my research and for always being there to help with any problem—no matter the issue. This PhD study would not have been possible had I not the opportunity to learn from him. As a senior postdoc in our group, he taught me so much about experimentation involving XRD and neutrons, and I am happy to be able to continue his work now that he has left the Viehland Group.

I also acknowledge the help of Dr. Jianjun Yao for being my first teacher of TEM research; his vast experimental experience helped me quickly learn complicated experiment procedures, and his creative research solutions were a constant source of inspiration.

Regarding my TEM research, I must thank Dr. Christopher Winkler for the many useful discussions we shared when he was providing instrument support and training at the Nanoscale Characterization and Fabrication Laboratory in Virginia Tech.

I extend my gratitude to Dr. Yaojin Wang for his great discussions, guidance, and encouragement. He treated me like a younger brother and I will always retain wonderful memories of working with him.

Being a member of a group with many Chinese researchers, I would like to express my sincere thanks to Dr. Zhiguang Wang, Dr. Junqi Gao, Yin Shen, Menghui Li, Yanxi Li and Yue Zhang. Though it was sometimes challenging for me to understand all the details of their research, the exposure to so many different research areas was helpful and exciting. More importantly, I cannot adequately express how much their friendship meant to me.

I could not have completed this journey without the advice and guidance of Prof. Olivier Delaire at Oak Ridge National Lab. It was a fantastic experience to be able to work and study with him for more than a year, and I extend my sincerely gratitude to him for providing that opportunity. Not only did I learn the fine art of neutron scattering experimentation from him, but I also benefited immeasurably from his professional research attitude, incredible work ethic, and great thirst for knowledge.

I would also like to thank other members in my group at ORNL; although I only spent a year there, I learned so much about how to conduct independent research through their selfless assistance. In particular, I acknolwedge the help of Dr. Dipanshu Bansal for our engaging discussions and help with my research.

Finally, I would like to express my deepest thanks to my parents. There is an old saying in Chinese: "While his parents are alive, the son may not go abroad to a distance. If he does go abroad, he must have a fixed place to which he goes." It is my honor to have parents who supported my research career and always provided a warm haven for my soul.

TABLE OF CONTENTS

LIST OF FIGURES

LIST OF TABLES

1. Introduction

Growing environmental concerns, coupled with increasing regulatory restrictions, are requiring industries to develop non-lead-based compositions of ferroelectric and piezoelectric materials. These materials—now widely used in sensors, actuators, and transducers—are for the most part lead-based compounds such as $Pb(Zr,Ti)O_3$ (PZT). Indeed, PZT represents the dominant market share for use in these technologies. Moreover, next generation compounds, which include $Pb(Mg_{1/3}Nb_{2/3})O_3$-xat%$PbTiO_3$ (PMN-x%PT) [1] and $Pb(Zn_{1/3}Nb_{2/3})O_3$-xat%$PbTiO_3$ (PZN-x%PT) crystals [1, 2] with ultrahigh piezo-/electromechanical properties, are also Pb-based systems, making them problematic for meeting more restrictive environmental standards [1, 3, 4]. As an alternative, Pb-free ferroelectrics such as NBT-derived single crystals represent viable next-generation materials for use in ferro-/piezoelectric applications. Indeed, over the last decade, researchers have made important advancements in developing these types of NBT-based crystals [5-8]—so much so that they are beginning to approach the properties of the widely used commercial PZT ceramic materials [9]. However, advances are not yet sufficient to disrupt the ongoing use of PMN-x%PT and PZN-x%PT crystals in next-generation applications.

There are numerous similarities between lead-based and non-lead systems. First, many of these systems are based on relaxor ferroelectrics with a perovskite crystal structure (ABO_3). Second, the phase diagram structures of these systems are similar, and they also feature related morphotropic phase boundaries (MPBs) [10]. However, the intrinsic mechanistic difference between the two generic systems (Pb-based and non-Pb-based) is less distinct. For example, lead-base solid solutions such as PMN-x%PT are B-site disordering; in contrast, the non-lead systems such as NBT-x%BT are A-site disordering.

As a new type of piezoelectric material, there remains much to be learned about Pb-free piezoelectric crystals. For instance, in addition to enhancing our understanding the nature of the piezoelectric third-rank tensor coefficients such as d_{33} and d_{15}, a thorough knowledge of the Curie temperature, leakage current, and electromechanical properties is also essential for increasing their applications potential. As will be detailed herein, multiple dopants may have to be incorporated into NBT to modify its microstructure and properties to meet these specific requirements, which may further complicate its chemical structure-property relationships.

1.1. Ferroelectricity and Ferroelectric Materials

1.1.1. Piezoelectricity

Solid materials with piezoelectric characteristics generate an electrical charge in response to an applied mechanical stress. Piezoelectricity was first discovered in 1880 by the French physicists, Jacques and Pierre Curie, in connection with their research on the relationship between pyroelectricity and crystal symmetry. The piezoelectric effect represents the energy transformation from mechanical to electrical forms, while the reverse (or converse) piezoelectric effect represents a transfer in the opposite transfer direction. Piezoelectric materials feature both a piezoelectric effect and a converse piezoelectric effect, as illustrated in Figure 1.1[11].

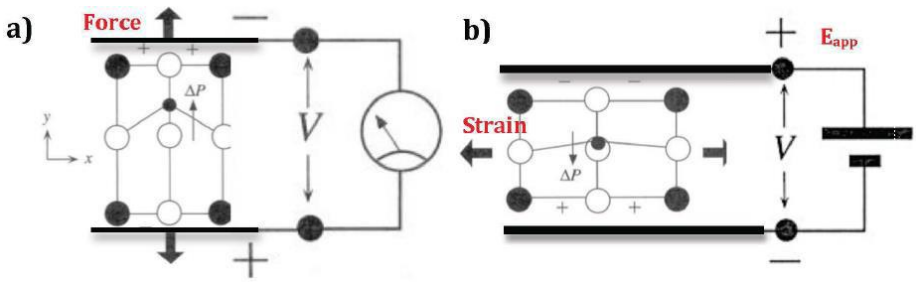

Figure 1.1: (a) Piezoelectric effect and (b) reverse piezoelectric effect. [11] Used under fair use, 2016.

Based on thermodynamic research, it has been proven that the piezoelectric effect is equal to the converse piezoelectric effect, following the piezoelectric equation of state shown below:

$$d_{ij} = \left(\frac{\partial D_i}{\partial T_j}\right)^E = \left(\frac{\partial S_i}{\partial E_j}\right)^T,$$

where D is the dielectric charge density displacement, E is electric field strength, S is strain, and T is stress. This equation is valid when the system is considered to be under adiabatic conditions. Notice that D and E are vectors, and T and S are symmetric tensors of rank 2. Using index expansion for i=1,2,3 and j=1,2,3,4,5,6 (where the indices can be changed from 2 notation to 1 notation: 11 → 1; 22 → 2; 33 → 3; 23 → 4; 13 → 5; 12 → 6), it can easily be seen that d_{ij} can have up to 18 independent tensor coefficients depending upon the crystal symmetry of the material systems. This factor is known as the piezoelectric coefficient and its unit are C/N (or pC/N in practicality). Among all the d_{ij}, longitudinal d_{33} is most commonly utilized to judge a material's piezoelectric properties. Piezoelectric materials can be used in electromechanical systems as both sensors (using the piezoelectric effect) and actuators (using the reverse piezoelectric effect). Additionally, piezoelectrics are widely used

in high voltage and other power systems, and in sensors, actuators, frequency standard and piezoelectric motors. [12]

1.1.2. Ferroelectricity and perovskite ferroelectrics

The underlying principle for ferroelectricity is the existence of a spontaneous polarization, P, which is a polar vector (i.e., 1st rank tensor). The spontaneous polarization in ferroelectric materials originates from internal electric dipole moments, which in turn are coupled to the crystal structure or lattice. Comparing the different relationships between polarization, P, and applied electric field, E, ferroelectrics feature unique P-E (polarization electric field) hysteresis loops, as shown in Figure 1.2. The nature of P-E loops can also identify important ferroelectric parameters, such as the coercive field (E_c) and remnant polarization (P_r).

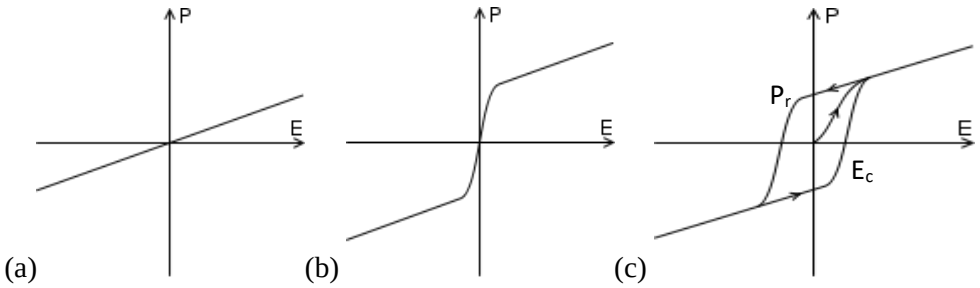

*Figure 1.2: Sketch of different polarization [*]: (a) dielectric polarization; (b) paraelectic polarization; (c) ferroelectric polarization (*Images modified from* https://en.wikipedia.org/wiki/Ferroelectricity*). Used under fair use, 2016.*

Ferroelectric materials are distinct in that they undergo spontaneous polarization, which can have two or more crystallographic equivalent directions, and where (under the application of an electric field) the direction may be switched. The coupling between electric dipoles and the lattice structure requires specific symmetry relationships within the 32 point groups.

Among these 32 point groups, only 10 of them are allowed to have a spontaneous polarization: 1(C1), 2(C2), m(Cs), mm2(C2v), 4(C4), 4mm(C4v), 3(C3), 3m(C3v), 6(C6) and 6mm(C6v). These 10 classes are known as the polar point group.

The internal electric dipoles of a ferroelectric crystal are coupled to the crystal lattice, so anything that alters the lattice will then alter the strength of the dipoles—in other words, a change in polarization will occur. This polarization change then results in a change in the surface charge, which can cause current to flow in the case of a ferroelectric capacitor, even without the presence of an external voltage across the capacitor. Two main stimuli that will change the lattice dimensions of a material are force and temperature. The generation of a surface charge in response to the application of an external stress to a material is called piezoelectricity. A change in the spontaneous polarization of a material in response to a change in temperature is called pyroelectricity.

Piezoelectricity and pyroelectricity require less crystal symmetry restrictions. Thus, both phenomena are more common amongst the point groups. Piezoelectricity only requires a non-centrosymmetric point group, while pyroelectricity is common in all crystals featuring polarization (and does not have to be reversible). It must be noted that although all ferroelectrics are piezoelectric and pyroelectric, but not vice versa. Figure 1.3 illustrates these basic relationships among groups. In general, piezoelectric materials that do not feature reversible spontaneous polarization have low piezoelectric properties and coupling coefficients—for example, quartz, which has unique linear piezoelectric properties that are nearly temperature independent. In order to obtain a large piezoelectric coefficient and coupling factor, a material must not only be piezoelectric, but must also be ferroelectric with a reversible spontaneous polarization that enhances the effects.

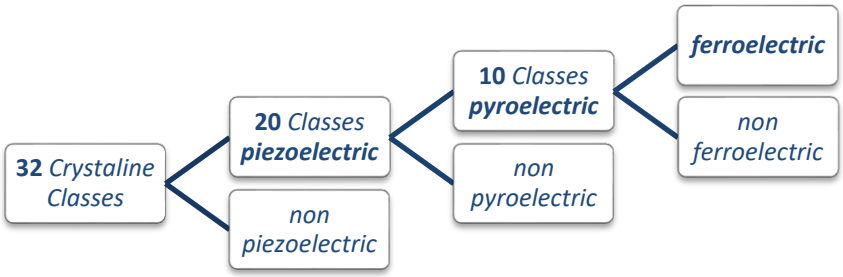

Figure 1.3: Brief classification of crystalline classes.

The spontaneous polarization in a crystal also has bound charges associated with it. Specifically, the bound charges generate a depolarization field, which has the opposite direction to the polarization, P. This phenomenon results from the increase in the electrostatic energy of the system. Under mechanical restraint, the strain from the spontaneous polarization will also raise the strain energy. To avoid such instability, the crystal can be divided into many small districts or regions, wherein the electric dipoles share the same direction. These small spatial regions are known as domains, and the boundaries between these distinct domains are referred to as domain walls. The appearance of domains lowers a crystal's electrostatic energy and its strain energy, but also introduces the influence of the domain wall energy. Thus, the static domain structure is defined by the minimum of a system's total free energy.

Typically, the spontaneous polarization of a material is strongly affected by temperature. Specifically, when the temperature is above the Curie temperature, T_C, spontaneous polarization disappears and the ferroelectric properties are transformed into a high-temperature paraelectric state, which no longer possesses a permanent dipole moment. The

phase transition between the ferroelectric and paraelectric states is typically known as the ferroelectric phase transition. This transition involves changes between asymmetric and symmetric point groups.

1.1.3. Perovskite ferroelectric relaxors

Among all ferroelectrics, the perovskite-types are the most widely used class of materials (although not the first to be discovered). The familiar chemical structure for perovskite is ABO_3, but can also feature a mixed cation valence combination of $A^{2+}B^{4+}$ or $A^{1+}B^{5+}$. The perovskite structure is usually shown in a simple (pseudo) cubic lattice (Figure 1.4a), where the A-site ion is usually larger than the B-site ion and the six face centers are occupied by oxygen ions.

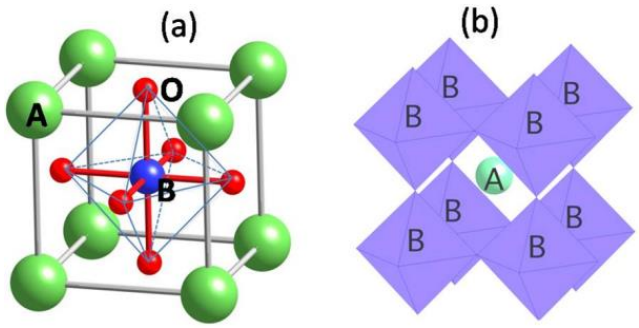

Figure 1.4: Perovskite structure [13] (a) in the form of a cubic cell, (b) in the form of an oxygen octahedron framework. Used under fair use, 2016.

The oxygen ions form an oxygen octahedron, with the B-site cations located in the center position of the cell. Thus, the crystal lattice can be treated as an oxygen octahedron framework, where the A-site cations are located at the gaps between the oxygen octahedrons, as shown in Figure 1.4b. The coordination numbers are 12 for A and of 6 for B. The high symmetry condition of the oxygen octahedron (at high temperatures) has 3 four-rotation, 4 three-rotation, and 6 two-rotation axes of symmetry. The spontaneous polarization in the

perovskite ferroelectric crystal originates from the B-site cation off-center displacements. Both these displacements and the spontaneous polarization can occur along three different types of symmetric axes, which are usually marked as [001], [110] and [111] in a cubic lattice.

The ABO_3 perovskite materials also can feature mixed-valence disorderings at both the A-site and B-site, which induces relaxor ferroelectric characteristics. Representatives of this type of mixed-cation perovskite material are the B-site disordered PMN ($Pb(Mg_{1/3}Nb_{2/3})O_3$), and the A-site disordered ($Na_{1/2}Bi_{1/2})TiO_3$ (NBT). Perovskite relaxors have been found to possess outstanding ferroelectric, piezoelectric, and pyroelectric properties, and can have a wide range of applications. Although they have been studied for over 50 years, the complex mechanisms associated with relaxor behavior are still not well understood—although ongoing research continues to reveal important information. For example, compared to normal ferroelectrics, like $BaTiO_3$, relaxor ferroelectrics have three distinct families of properties, which were summarized in a review paper published by Cross [14], and shown in Figure I.5.

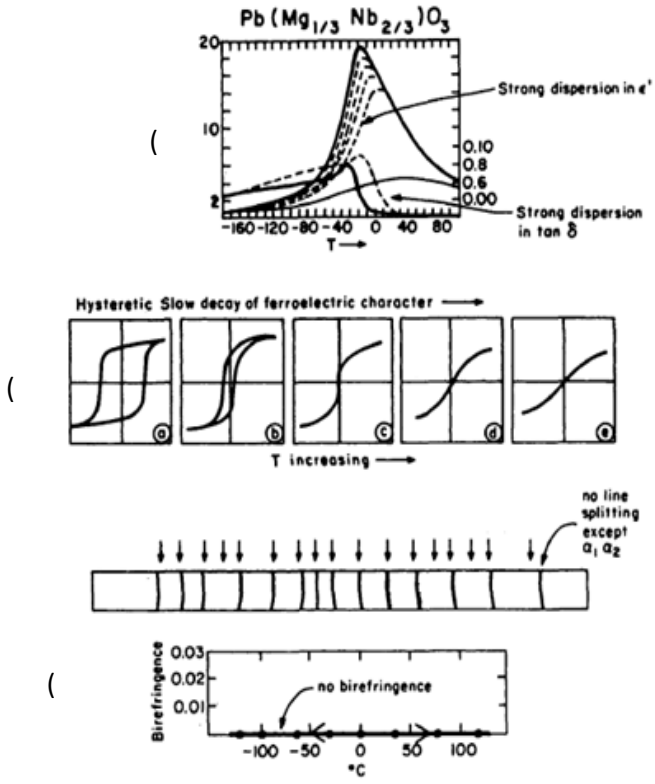

Figure 1.5: Characteristic features of a ferroelectric relaxor, using PMN as a representative. (a) Dielectric dispersion in PMN as a function of temperature and frequency; (b) Dielectric hysteresis in PMN as a function of temperature; (c) Optical and x-ray evidence for the absence of a macroscopic phase change below the TC. Reprint with permission from [14]. Copyright © 1987, Taylor & Francis.

The first significant characteristic of a relaxor is a diffuse phase transition between the ferroelectric and paraelectric phases, which is frequency dispersive (see Figure 1.5a). Ferroelectric relaxors have a dielectric constant peak near Tc, but the peak is broad and its location can change with frequency alterations. Near the peak temperature and with increasing frequency, the dielectric constant decreases, the dielectric loss increases, and both the peaks of the dielectric constant and loss shift towards higher temperature. The second characteristic is that the dielectric hysteresis in ferroelectric relaxors slowly degenerates as

the temperature is increased near T_c, as can be seen in Figure 1.5b. In this case, the spontaneous polarization gradually drops to zero near T_C, and will even persists above T_c. The third characteristic is that there are no macro-volume changes or apparent symmetry changes during the ferroelectric phase transition, as evidenced by optical and X-ray measurements (Figure 1.5c). These three characteristics of ferroelectric relaxors contribute to the fact that they are widely utilized in actuators, sensors, and transducers.

The most widely used piezoelectric system is the $Pb(Zr_{1-x}Ti_x)O_3$ (PZT) solid solution. PZT features a complex phase diagram containing rhombohedral and tetragonal ends, and a morphotropic phase boundary (MPB) [15, 16] between these two phases. Various compositions near the MPB have attracted considerable interest due to their high piezoelectric properties ($d_{33}\approx500$pC/N with strains $\approx0.15\%$) [17]. The development of PZT and La-doped PZT (PLZT) ceramics in the 1950s soon made them a dominant piezoelectric material in the commercial market, which displaced $BaTiO_3$ (BT) [18]. The advantages of PZT include its high d_{33} and electromechanical coupling coefficients. Additionally, PZT features (1) high T_c values, which permit a broader operation range within a range of temperatures, including higher processing temperature during device manufacturing, (2) low coercive field and easy polarization, (3) a wide range of dielectric constants, and (4) relatively easy sintering conditions.

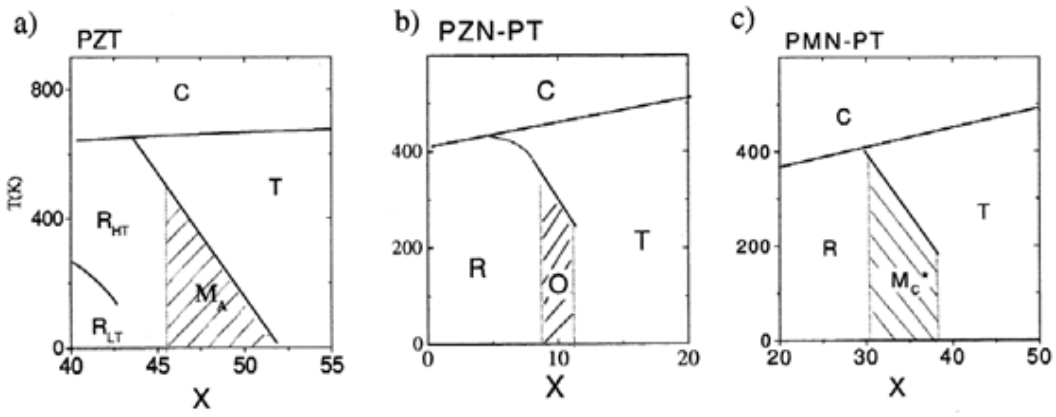

Figure 1.6: Phase diagram of lead-based ferroelectric relaxors. Phase diagrams of (a) PZT; (b) PZN-PT; (c) PMN-PT. Reprint with permission from [4]. Copyright © 2002, Elsevier Science Ltd.

Based on the success of PZT, further developments targeting lead-based relaxor materials have focused on the general chemical formula of $Pb(B_1B_2)O_3$ (B_1=Mg^{2+},Zn^{2+},Ni^{2+}, Sc^{3+}..., B_2=Nb^{5+},Ta^{5+},W^{6+}...). Among them, PMN-x%PT and PZN-x%PT single crystals are the most intriguing due to their ultra-high piezoelectric properties and electrostrictive properties, which are significantly higher than those of conventional PZT ceramics. Again, these are the relaxor ferroelectric single crystal systems. Interestingly, analogous to PZT, PMN-PT and PZN-PT feature similar phase diagrams with MPBs between rhombohedral and tetragonal phases [4], as shown in Figure 1.6. However, PMN-PT and PZN-PT crystals have well-known symmetry-bridging monoclinic phases within the MPB region, and their unique characteristics will be discussed later. For example, PMN-PT near its MPB region ($0.30<=x<=0.33$) exhibits ultrahigh piezoelectric (d_{33}>2500pC/N, d_{15}>5000pC/N [3]) and electromechanical coupling (k_{33}>94%). Figure 1.7 illustrates the strain response of these crystals to an applied electric field, comparing their induced strain characteristics to various common types of PZT ceramics and other Pb-based perovskites.

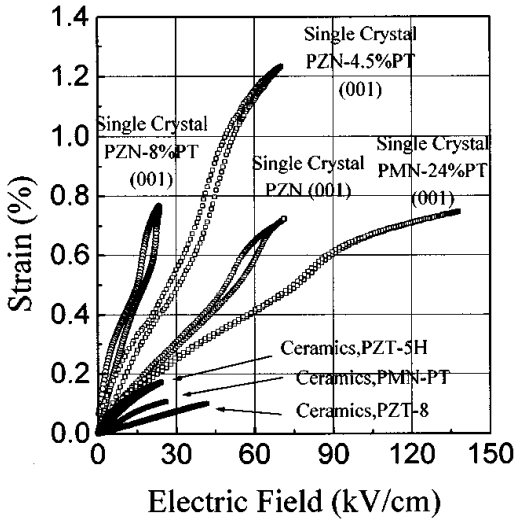

Figure 1.7: Electrostrictive properties of PMN-PT and PZN-PT: Strain vs E-field behavior for [001] oriented rhombohedral crystals of PZN-PT and PMN-PT and for various electromechanical ceramics. The maximum field was limited either by dielectric breakdown or by voltage limit of the apparatus. Reprint with permission from [1]. Copyright © 1997, AIP Publishing LLC.

1.1.4. Environmental concerns for Pb

The well-known toxicity of lead remains a pressing global concern. Even at low levels, lead intake negatively impacts human physiology, and prolonged contact can be catastrophic. To date, however, the global market of piezoelectrics is still dominated by conventional lead-based materials, such as PZT [19], making it increasingly urgent to develop alternative lead-free materials—especially given the growing number of potential applications, as shown in Figure 1.8 [19]. And indeed, as shown in Figure 1.9, scholarly reports describing the development of lead-free materials have increased dramatically—including a growing number of research publications on the topic of lead-free ferroelectrics and piezoelectrics. The data in this figure resulted from an inquiry targeting Pb-free-related publications (using

"lead-free OR non-lead OR Pb-free" as delimiters) using the *Web of Science* database. The resulting number of articles describing lead-free piezoelectric materials clearly indicates the rising interest in alternative environmentally friendly piezoelectrics.

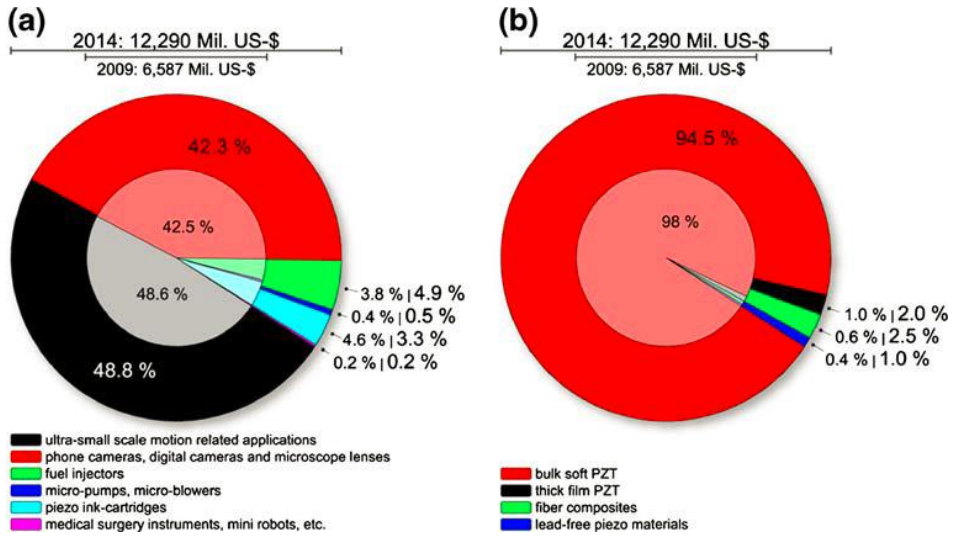

Figure 1.8: Global market shares of piezoelectric actuators with respect to (a) applications and (b) materials. The scale bars on top of each plot denote market size. Reprint with permission from [19] . Copyright © 2012, Springer Science+Business Media, LLC.

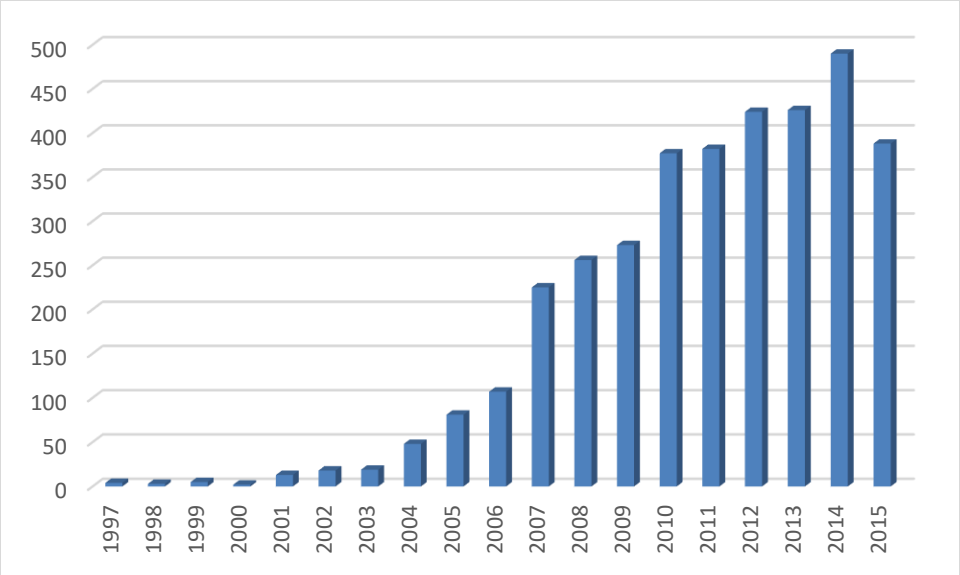

Figure 1.9: Publications on lead-free ferroelectric found in refereed journals.

In order to achieve the goal of replacing PZT with alternative lead-free materials, they must have properties close to that of PZT, including good thermal stability. Among all the next-generation Pb-free materials, $Na_{0.5}Bi_{0.5}TiO_3$-$BaTiO_3$ (NBT-BT) and other NBT-derived solid solutions attract the most attention due to the multiple similarities between NBT-BT and its successful predecessor, PMN-PT.

1.1.5. NBT and NBT-derived single crystal

Currently, research and development efforts directed toward Pb-free piezoelectric materials are focused on the $BaTiO_3$ (BT), $(Na_{1/2}Bi_{1/2})TiO_3$ (NBT) and $KNbO_3$–$NaNbO_3$ (KNN) systems [5-8]. NBT is a well-known lead-free perovskite piezoelectric material first reported by Smolenskii et al. in 1960. [20] Figure 1.10 [21] shows the mixed A-site cation perovskite structure of NBT.

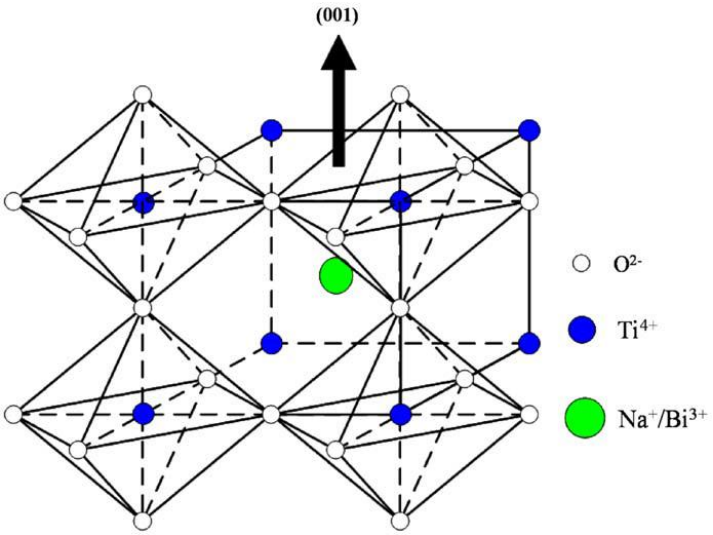

Figure 1.10: Perovskite structure of NBT. In the presence of oxygen octahedron frames, Na^{+}/Bi^{3+} ions occupy the A-site and Ti^{4+} ions occupy the B-site. Reprint with permission from [21]. Copyright © 2009, Elsevier B.V.

Structurally, NBT is quite similar to PMN, but where Ti^{4+} in NBT provides the high polarizability, in PMN that role is served by Pb^{2+}. Also analogous to PMN, NBT exhibits relaxor ferroelectric behavior and has a pseudocubic (i.e., distorted cubic) structure at room temperature. However, there are important differences between the two—principally that NBT is an A-site disordered system; in contrast, PMN is a B-site disordered one. NBT exhibits strong ferroelectric properties with a large remnant polarization (P_r=38C/cm^2) and a Curie temperature at T_c=320°C. Although the T_c of NBT is relatively high, NBT has a ferroelectric-to-antiferroelectric phase transition corresponding to the depolarization temperature (T_d), which is below 200°C. The depolarization results in a significant degradation of properties, making T_d more important for NBT- and NBT-derived materials. In addition, the use and application of NBT have been restricted by its difficult preparation, requiring a sintering temperature of over 1200°C, which in turn results in the vaporization of Bi ions at high temperature. The resultant high leakage currents (from the Bi deficiency) and

the high coercive field associated with NBT make polarization saturation and switching difficult to achieve in conventionally fabricated NBT samples [16].

Following the success of adding $PbTiO_3$ (PT) to PMN to create a solid solution of PMN-PT, NBT can also be expected to form a similar solid solution between relaxor and normal ferroelectrics, where an MPB between the rhombohedral (R) and tetragonal (T) phases would reside in the solid solution. Consequently, $(Bi_{1/2}Na_{1/2})TiO_3$–$xBaTiO_3$ (NBT-x%BT) [22] and $(Bi_{1/2}Na_{1/2})TiO_3$–$x(Bi_{1/2}K_{1/2})TiO_3$ (NBT-x%KBT) [23] have been developed. The ternary system, NBT-BT-KBT, has also investigated in an attempt to unify the NBT- and KBT-derived systems. Figure 1.11 [16] shows the ternary phase diagram and its MPB band.

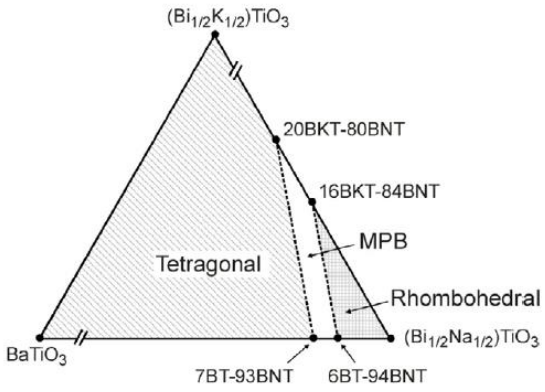

Figure 1.11: Ternary phase diagram of NBT-KBT-BT [16]. Copyright © 2010, National Institute for Materials Science.

The properties of these solid solutions fluctuate not only according to composition specifics, but also from the perspective of different preparation and growth methods. As described herein, high-performance single crystals of NBT-BT and NBT-KBT were grown via the top-seed solution growth (TSSG) method. For NBT-x%BT, in which the MPB is near x=5, the longitudinal piezoelectric d_{33} and thickness electromechanical k_t coefficients have

peak values of d_{33}=423 pC/N and k_t=68% at x=5, respectively. [24] Similar results have been reported by other investigators, including studies by Chiang et al., who reported that NBT-5.5%BT had a peak value of d_{33}=450 pC/N [25]. Compared to NBT-BT, synthesizing NBT-KBT is more complicated due to the chemical segregation effects within solid solution crystals during fabrication and growth [26]. Crystals grown by the TSSG method still cannot reach their respective MPBs even near x=0.2, and NBT-12KBT has been reported to have a maximum d_{33} value of 208 pC/N [27]. Meanwhile, ceramic sample using a solid-state reaction method displayed a peak value of d_{33}=134 pC/N, which was achieved at an MPB located near x=0.17~0.25 [28].

The NBT- and NBT-derived systems have many possible substituent/doping choices for both the single crystal and ceramic forms. [29] A popular choice is Mn because it can strongly affect the formation of oxygen vacancies and resultant defect dipoles. Mn is believed to occupy the B-site of the perovskite lattice as the ionic radius of Mn^{4+}(0.53 Å) is close to that of Ti^{4+}(0.61 Å). However, the high crystal growth temperature brings into play different oxidation states of Mn ions, making it difficult for them to be contained to only B-site occupancy. The different positional occupations must be considered in terms of their impact on industrial application. For example, a hysteretic P-E relation is required in memory applications that are based on polarization switching. But in high precision sensors, capacitors, and actuator applications, hysteresis should be avoided [30]. Applied in NBT-BT system, the highest d33 values for NBT-BT have been reported to increase from 280 pC/N to 480 pC/N [9]. This enhancement has been attributed to an increase in the resistivity enhanced by the presence of Mn. Further research has documented increased ferroelectric ordering and enhanced in-plane octahedral tilting in Mn:NBT-BT compared with NBT-BT [31].

Another substituent choice in doping and defect compensation is Fe. Similar to Mn-doping, Fe^{3+}(0.64 Å) occupies the Ti^{4+} position, and the presence of similar defect dipoles (Fe'Ti-Vo``)` have been verified by EPR spectra [32]. The defect dipole (Fe'Ti-Vo``)` lowers the concentration of free oxygen vacancies that originate from the compensation of Ti^{3+}, thereby decreasing the leakage current. Low levels of leakage current then make it easier to more completely pole the single crystals, which results in significantly higher piezoelectric properties. The d_{33} value of 0.2Fe-NBT-5BT has been reported to be 590 pC/N, which represents a nearly 40% improvement over the analgous value for its undoped prototype. Resulting drawbacks are also similar to those associated with Mn-doping, where with increasing dopant concentrations, the defect dipoles impact the lattice, favoring tetragonal phase stability and decreasing the value of T_C.

1.2. Phase boundaries, Landau-Devonshire theory, and soft modes

1.2.1. Phase boundaries in ferroelectric solid solutions: MPBs and PPTs

As mentioned above, the piezoelectric properties of solid solutions like PMN-PT, PZT and NBT-BT are closely related to their composition. The peak piezoelectric properties of these perovskite solutions are located near the MPB, which is a unique type of temperature-independent boundary occurring between the rhombohedral and tetragonal phases.

Characteristic phase diagrams for perovskite solid solutions are shown in Figure 1.12 [16]. Note that these phase diagrams exhibit either a morphotropic phase boundary in NBT-BT/NBT-KBT or an orthorhombic to tetragonal (O–T) polymorphic phase transformation (PPT) in BT/KNN. Due to the temperature independence of the MPB, high-performance piezoelectric materials near the MPB can work over a much wider temperature range compared to the PPT materials. As a result, most researchers studying the new generation of piezoelectric materials have focused on solid solutions near the MPB. However, the mechanisms associated with the MPB for the Pb-free piezoelectric systems remain unclear. For PZT, many theories have been formulated to explain its structural origin. Although similar MPBs have been found in NBT-BT and NBT-KBT, the question remains as to whether these theories are similarly applicable, and whether these lead-free materials will achieve the same high piezoelectric property values compared to those of PMN-PT crystals.

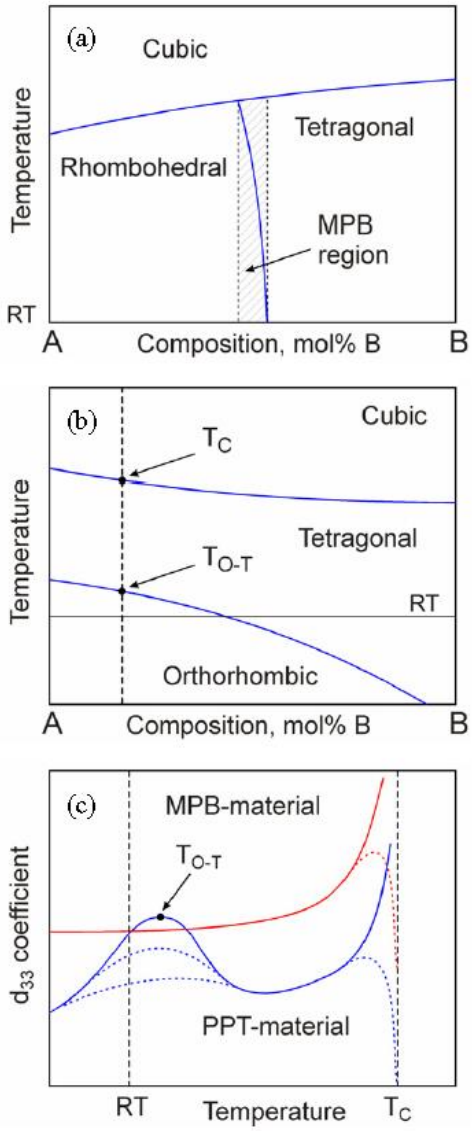

Figure 1.12: Characteristic (hypothetical) phase diagrams for perovskite solid solutions exhibiting either a (a) morphotropic phase boundary (MPB), or (b) orthorhombic to tetragonal (O–T) polymorphic phase transformation (PPT). The resulting temperature-dependence of the piezoelectric coefficient (c) for hypothetical MPB and PPT materials with the same room-temperature (RT) piezoelectric coefficient and same Curie temperature (Tc), where dotted trend lines indicate degradation of piezoelectric properties due to depolarization at temperatures near TO–T and TC [16]. Copyright © 2010, National Institute for Materials Science.

1.2.2. Phenomenological and macroscopic theories for ferroelectric transformations

When analyzing perovskite systems, one must consider ferroelectric transformation as a critical element amongst the macroscopic theories based upon structure. Ferroelectric transformations are typical structural phase transitions, which can be described using thermodynamic phenomenology with a Landau-Devonshire model. Here, ferroelectric transformations are based on a series expansion of the spontaneous polarization (P) order parameter in a Taylor series function. From the relationship D= $_0$E+P, the dielectric displacement (D) is suitable as the independent variable or order parameter, and where $_o$ is the permittivity of free space. The corresponding characteristic Landau-Devonshire function of D is the elastic Gibbs free energy G

$$dG = -SdT - x_i dX_i + E_m dD_m \qquad (i = 1\sim6, m = 1\sim3).$$

The generalized model considers the simplified conditions of constant temperature (dT=0) and mechanically free boundary conditions (dXi=0). The minimum G that will achieve the stable phase of the system is:

$$G = G_0 + \frac{1}{2}\chi\left(D_x^2 + D_y^2 + D_x^2\right) + \frac{1}{4}\xi\left(D_x^4 + D_y^4 + D_x^4\right) + \frac{1}{4}\lambda\left(D_x^2D_y^2 + D_y^2D_z^2 + D_z^2D_x^2\right)$$

$$+\frac{1}{6}\zeta\left(D_x^6 + D_y^6 + D_x^6\right) + \frac{1}{6}\eta D_x^2D_y^2D_x^2 + \cdots$$

Here, the factors before each terms among the expansion are functions of temperature. A further simplification can be achieved if one assumes that D is directed along one axis of the x, y, or z axis. Then, the scalar form of the function can be given as:

$$G = G_0 + \frac{1}{2}\alpha D^2 + \frac{1}{2}\beta D^4 + \frac{1}{2}\gamma D^6$$

Based on Devonshire's assumption that only the first-order expansion term is temperature dependent in a linear manner, $\alpha_0(T - T_0)$, and that β, γ are independent of T,

$$G = G_0 + \frac{1}{2}\alpha_0(T - T_0)D^2 + \frac{1}{2}\beta D^4 + \frac{1}{2}\gamma D^6.$$

This model is able to explain quite accurately some experimental results for the prototypic perovskite ferroelectric $BaTiO_3$, such as the Curie-Weiss law where T0 is Curie-Weiss temperature. This equation is widely used in classifying first-order ($\beta<0$) and second-order ($\beta>0$) phase transformations of homogeneous paraelectric-ferroelectric transformations in ordered perovskites.

1.2.3. Soft modes and microscopic theories

On the basis of Landau theory, the thermos-dynamical theory for ferroelectric transformations was advanced by the work of Muller, Ginzburg, and Devonshire in the 1950s. A decade later, atom-level ferroelectric microscopic theory was first reported in the early 1960s. The relatively late development of a microscopic theory can be linked to a number of factors. One such factor is the complexity of the origins of ferroelectricity, which is related to lattice structure, electronic structure, and both long- and short-range polar interactions. Indeed, most early ferroelectric materials—especially the early Rochelle salts and the water-soluble potassium dihydrogen phosphate (KDP) systems—featured highly complex microscopic structures that made a traditional microscopic approach to research difficult to achieve during this early scientific era.

A breakthrough was reported by Cochran and Anderson based on their work on lattice dynamics. The concept of soft modes was introduced to describe the “softening” of a transverse optical phonon mode (TO) during ferroelectric transformation. The “softening” of the TO mode made the displacement of the ions become static, and thus brings a permanent spontaneous polarization and crystal lattice distortion. The concept of the soft mode underscores the typical characteristics of all ferroelectric transformations in that all types of

such polar transformations, including anti-ferroelectric ones, are special conditions of structural phase transformations. The soft mode concept is strongly supported by experimental results obtained via neutron scattering and Raman scattering.

The basic concept of the ferroelectric soft mode theory is that ferroelectricity is generated by the softening of a single TO mode at the Brillouin zone center. Here, the term "softening" refers to the decreasing circular frequency ω of the simple harmonic oscillator that is representative of lattice displacement:

$$\omega \propto \sqrt{\frac{k}{m}},$$

where k is a force factor and m is the mass. A smaller value of k means "softer" and is consistent with a decreasing ω. When ω is softened to zero and atoms cannot return to their original balance position, it is referred to as mode "freezing." The optical modes represent the positive and negative ions oscillating in opposite directions, and the modes at the Brillouin center are those with a wave factor of q=0. In these TO mode types, ion displacement in every lattice cell have the same phase. In other words, when they are frozen, the same ion displacements will appear in all lattices and generate a uniform spontaneous polarization. Correspondingly, if the TO modes at the Brillouin boundary freeze, then the original paraelectric adjacent cell will feature electric dipoles equal and opposite in direction. As a result, the cell size is doubled in length of sides, generating the anti-ferroelectric structure.

The acoustic mode describes the oscillation of adjacent atoms in the same direction. Thus, the softening of the acoustic mode cannot lead to a net spontaneous polarization. However, the freezing of the acoustic mode at the Brillouin center may create spontaneous strain, corresponding to a ferroelastic transformation.

1.3. Structural origin of ultra-high electro-mechanical properties in PMN-PT and PZN-PT crystals.

Before considering the questions that guided this investigation of lead-free piezoelectric materials, it is first necessary to consider the extent to which existing theories apply to lead-based solid solutions. Researchers have developed numerous models to understand the structural origin of the high piezoelectric and electromechanical properties of MPB compositions of Pb-based systems. While some of these models have unavoidable restrictions that make it difficult to apply them to Pb-free systems, others are relevant to these new systems. Four models are particularly relevant: (a) the engineered-domain model proposed by Park and Shrout [1]; (b) various structurally bridging intermediate monoclinic phase models [4, 33]; (c) a polarization rotation model emphasized by Fu and Cohen [34]; and (d) the adaptive ferroelectric nano-twin model [35].

1.3.1. Engineered-domain model

The engineered-domain model was first introduced by Park, Shrout and colleagues [1]. Based on concepts of the Landau theory, an applied E-field favors the component of the polarization whose orientations is parallel to E; as a consequence, the relative ferroelectric phase distortion is along that same direction. Thus, the engineered-domain model uses E-field-induced ferroelectric phase transition to explain the strain response under increasing E-fields, as shown in Figure 1.13 in the case of PZN-8PT [1].

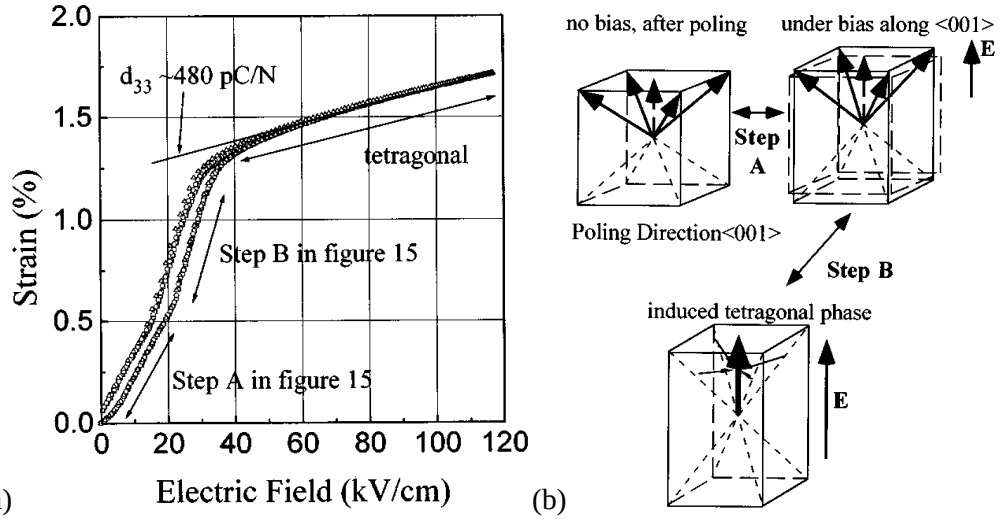

Figure 1.13: (a) Strain vs E-field behavior for a <001> oriented PZN-8%PT crystal. Maximum field is limited by the voltage limit of the apparatus. (b) Schematic diagram of domain configurations in <001> oriented rhombohedral crystals under bias (step A-piezoelectricity, step B-induced phase transition). Reprint with permission from [1]. Copyright © 1997, AIP Publishing LLC.

As illustrated in Figure 1.13b, the increasing E-field in Step A enhances R phase lattice distortion. And in Step B, the strain jump is believed to originate from the E-field-induced ferroelectric phase transition. As a consequence, a larger value of d_{33} was also expected in this step from the c/a ratio jump from R-phase to T-phase. Here, T phase distortion is parallel to the E//[001] and the initial R phase distortion is along <111>. While the model is useful for explaining some experiment results—most notably the anisotropy of the piezoelectric property enhancement—it is inadequate for explaining the piezoelectric properties, or d_{33} peak, near MPB.

1.3.2. Bridging monoclinic phases.

The field-induced phase transition theory has been useful for explaining the origin and nature of ε-E curves. This model was further supported by the discovery of various intermediate monoclinic phases that structurally bridge the R and T-phases, as confirmed by both X-ray diffraction and neutron diffraction results. For example, two types of monoclinic distortions, M_A and M_C, have been reported in all lead-based ferroelectrics, including PZT, PMN-PT, and PZN-PT [4]. Here, the notations follow results obtained by Vanderbilt and Cohen [34], and M_B was predicted.

The notations are based on the different spontaneous polarization paths of each phase. With respect to the pseudocubic lattice framework, P is constrained to the [001] direction in the T-phase (P4mm) [111], for the R phase, and [011] for the O-phase (Amm2). The bridging monoclinic M-phases correspond to lattice types whose polarization vectors are located on different mirror planes. The M_C-phase belongs to the Pm space group, in which P is along [0uv]. The M_A phase and M_B phase belong to the Cm(Bm) space group, in which P is along [uuv], with $u>v$ in M_A-phase and $u<v$ in M_B-phase, respectively.

These M phases help to identify the MPB structure in PMN-x%PT, as well as describe the phase diagram changes under an applied E-field along different directions [33]. In the case of PMN-x%PT and E//[001], the R-phase in the zero-field-cooling (ZFC) is replaced by the M_A or M_C phases. When the applied E-field direction is changed to [110], the M_C phase is replaced by O phase (or special M_C phase with u=v, thus P is along [0uu]), and the M_A phase is replaced by a M_B phase. The O phase field is tilted into the boundary region of the C and M_B phase, as shown in Figure 1.14, and the corresponding field cooling (FC) transformational sequence with E//[110] is $C \rightarrow M_B$ for $x \leq 0.2$; $C \rightarrow O \rightarrow M_B$ for $0.22 \leq x < 0.3$; $C \rightarrow T \rightarrow O \rightarrow M_B$ for $x \approx 0.3$; $C \rightarrow T \rightarrow O$ for $0.31 < x \leq 0.36$; and $C \rightarrow T$ for $x > 0.37$.

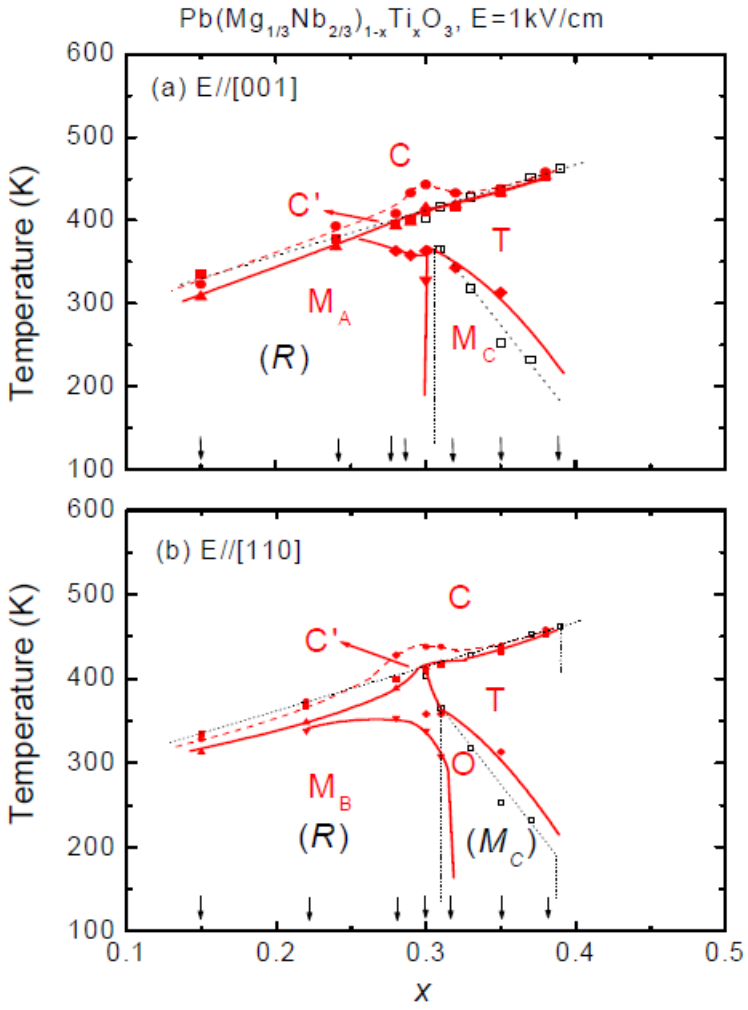

Figure 1.14: Modified phase diagrams of (a) [001] and (b) [110] electric field-cooled PMN-x%PT crystals. Reprint with permission from [36]. Copyright © 2006, American Physical Society.

The different M phases described above were identified via *in-situ* X-ray diffraction studies [33], which resulted in different types of Bragg peak splitting under the application of an electric field. This approach can help determine the specific type of M phase, as shown in Figure 1.15.

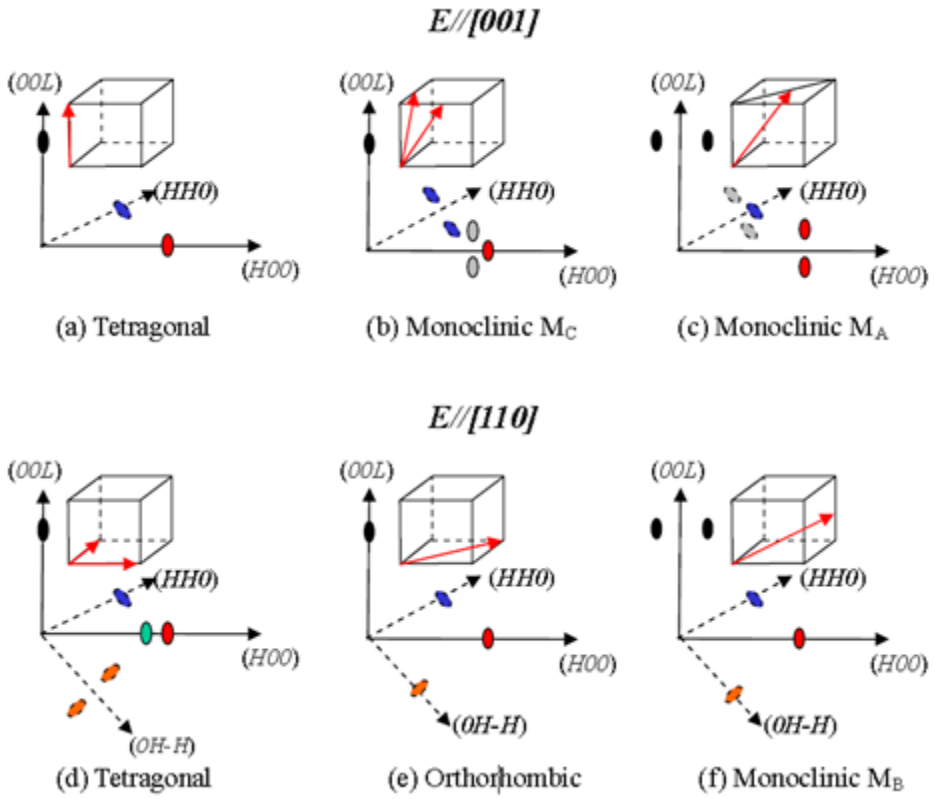

Figure 1.15: Domain configurations in reciprocal space with the application of electric field along [001] for (a), (b) and (c); and along [110] for (d), (e) and (f) [33]. Used under fair use, 2016.

1.3.3. Polarization rotation theory

Based on the experimentally established presence of apparent M phases, a new polarization rotation theory was proposed to explain the high piezoelectric and electromechanical properties of lead-based materials at MPB compositions. Proposed by Fu and Cohen, the polarization rotation theory is based on a first-principles study of BT [37]. The researchers' calculations confirmed that the free energy that gradual changes in the polarization vector orientation along a particular pathway was essential to the resulting piezoelectric properties. In the case of the R-phase of PMN-PT, the polarization rotation in the plane of (110), from the R-phase to the M_C phase, does not inhibit rotation due to a flat

free energy functionality. In turn, under the application of E, an ultra-large piezo-response occurs. Thus, the Fu and Cohen model of polarization rotation is based upon the concepts that (a) the M phases are homogenous, and (b) the polarization rotation and resultant high electromechanical properties are intrinsic to the structure. Accordingly, this model does not consider either domain contributions or nanodomain contributions as contributing significantly to the enhanced piezoelectricity of these Pb-based crystals near their MPBs. Based on Fu and Cohen's calculations, it is suggested that good candidate materials for ultrahigh piezoelectricity need to feature three elements: (1) a flat energy surface with a corresponding MPB; (2) large effective charges and large c-axis polarization variations under applied E, such as an R→T phase transformation; and (3) strong coupling between the internal degrees of freedom and strain.

The ability to predict the behavior of high-performance materials such as PMN-PT and PZN-PT using the polarization rotation theory was previously supported by experimental observation (i.e., prior to the development of the theory) of the bridging M phase at the MPB. Although different solid solutions could be expected to have different polarization rotation paths, the thermodynamic relationship between the paths and lowest free energy remains the same.

1.3.4. Ferroelectric adaptive phase theory

It must be noted, however, that there is a key aspect of the polarization rotation theory that must be taken into account. Consider the case when there is structural heterogeneity on the length scale that is less than the coherence length of the x-rays, which diffract. In this unusual case, which consists of nanotwins, the apparent symmetry obtained during diffraction could, in fact, represent the average over multiple nanotwins. This outcome, in turn, could result in the apparent symmetry being different than the local symmetry.

It is well established that PMN-x%PT relaxor single crystals consist of miniaturized domains that self-assemble into geometrically constrained hierarchical patterns. This observation implies that the domain wall energy is very small. This relationship represents both a key experimental and theoretical observation, as such that it now becomes possible to build an array of nanotwins. In fact, this key observation of high twin wall density requires that the free energy surface is flat, thereby providing only a slight anisotropy barrier. Interestingly, this is the same key assumption made by Fu and Cohen in their polarization rotation theory.

Accordingly, the ferroelectric adaptive phase theory was originally proposed by Viehland [35], and further developed by Jin and Wang [38] and Cao [33]. This theory is built upon the conformal miniaturization of stress accommodation twins. The adaptive phase structure can be considered to be analogous to the case of a martensite transformation, where the twin wall energy is reduced to near zero. The hierarchical arrangement of domains in an adaptive martensite was previously reported for a CuAu alloy [39]. In this case, domains self-organize into groups, which then self-organize into bands, which then occupy the entire space of the

crystal. This geometrical arrangement occurs as a self-assembly process driven to minimize the elastic free energy and to achieve near-complete stress accommodation.

However, in the case of PMN-x%PT crystals for compositions near the morphotropic phase boundary, the domain size has been found to be unusually small (as noted above); these miniaturized polar regions and twin boundaries are commonly referred to as polar nanodomains (PND) with T or R symmetry [40]. Transmission electron microscopy (TEM) and piezo force microscopy (PFM) studies have revealed that these PNDs near the MPB self-assemble into tweed-like structures similar to premartensitic states, which are known as adaptive martensite. [40] Due to its nanoscale size, the adaptive phase is, in fact, structurally inhomogeneous on a micro scale (~10nm), but could appear to be homogeneous using probes whose characteristic probe length-scales are longer, such as conventional X-rays. The new adaptive model was first used successfully to explain the characteristic transformations in the lattice parameters with temperature. This model can also explain changes in the ε-E curves from the redistribution of polar nanodomains. Generally, the adaptive model is based on an inherent structurally inhomogeneous state, which is in contrast to the homogeneous M phases associated with polarization rotation theory.

1.4. Polar nanoregions (PNR) and polar nanodomains (PND) in NBT-derived single crystals

It is widely believed that PNDs play an important role in both Pb-based and Pb-free piezoelectric systems. In PMN-x%PT, the presence of PNDs that self-assemble into hierarchical domains over various length scales has been reported [41, 42], which results achieving compatibility conditions in the elastically relaxed state. Under such circumstances,

adaptive phase theory predicts that the macroscopic structurally bridging M phases are, in fact, composed of nano-domains with R and T symmetries, and that the high piezoelectric properties result from a redistribution of the PNDs.

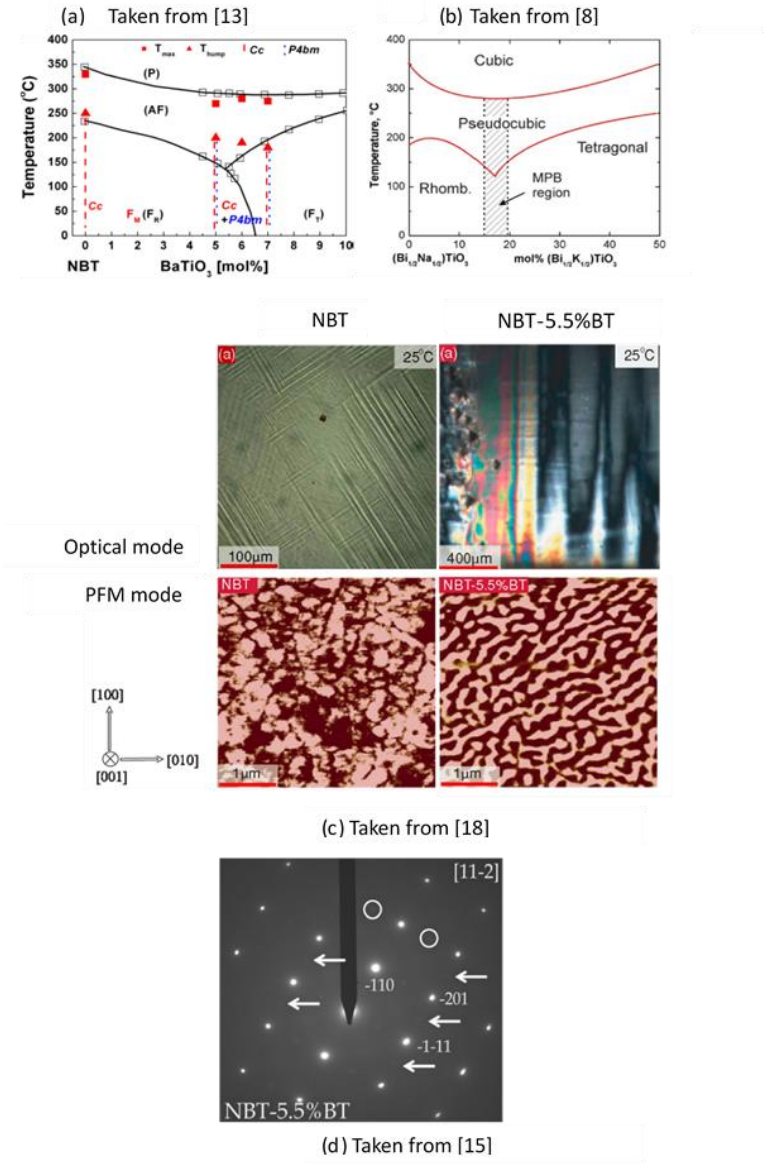

Figure 1.16: NBT-x%BT background introduction. (a) Phase diagram and MPB of NBT-x%BT. Reprint with permission from [24]. Copyright © 2014, AIP Publishing LLC; (b) Phase diagram and MPB of NBT-x%KBT [16]. Copyright © 2010, National Institute for Materials Science; (c) Domain morphology under optical mode and PFM mode. Reprint with permission from [43].Copyright © 2011 American Physical Society; (d) Phase coexistence in NBT-5.5%BT. T (P4bm) structure with $a^0a^0c^+$ tilt system is marked by arrows, and R (R3c) structure with $a^-a^-a^-$ tilt system is marked by circles (Glazer notation [44]). Reprint with permission from [45]. Copyright © 2012, AIP Publishing LLC.

Here, we utilize NBT-BT as an example of lead-free materials whose solid solution contains an MPB. In NBT, hierarchical domains have also been reported wherein a high-temperature ferroelastic T domain structure is elastically incorporated into the R ferroelectric phase field, and where polar domains of about micron-size form within this geometrical constraint, as illustrated in Figure 1.16c [43]. With increasing BT content, and as the MPB of NBT-x%BT was approached, the size of the polar domains became more regularized and the degree of self-organization in the domain hierarchy was enhanced. Furthermore, high-resolution transmission electron microscopy (HRTEM) images have confirmed the presence of multiple oxygen octahedral tilt domains, of a few nanometers in size, within the lamellar domains. Additionally, based on TEM select area electron diffraction (SAED) results, both kinds of superlattice reflections, in-phase tilt ½(ooe) and anti-phase tilt ½(ooo) (where o designates odd values of the Millers indices, and e even), were reported in NBT-5.5%BT, as illustrated in Figure 1.16d. These reflections originated from a T (P4bm) structure with an a0a0c+ tilt system, and an R (R3c) structure with an a-a-a- tilt system (Glazer notation), respectively, as summarized in Table 1.1.

Superlattice points in NBT-BT	M-point	R-point
Reciprocal space	½(ooe)	½(ooo)
Space group	P4bm	R3c
Crystal system	Tetragonal	Rhombohedral
Tilt system (O-octahedron)	$a^0a^0c^+$ One-tilt system	$a^-a^-a^-$ Three-tilt system
	In-phase 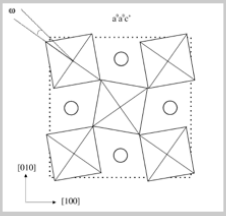	Anti-phase 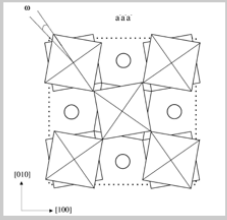

Table 1.1: Comparison of superlattice points and the tile systems. Sketches of oxygen octahedron tiltings are from the work of Jones et al. [46] (Copyright © International Union of Crystallography).

The coexistence of these two superlattices generates the corresponding phase coexistence, R and T phase, in the form of PNDs. With increasing BT content (approaching the MPB), the intensity of the ½(ooe) reflections and the volume fraction of the in-phase tilt PNDs were found to increase. It should also be noted that both types of tilt domains were found to be present over a large temperature range, with their respective volume fractions changing gradually with temperature. These results indicate the presence of PNDs with a structural frustration on the nm-scale between tilt clusters, which gradually evolve with changes to either temperature or composition.

In addition to TEM, other experimental techniques such as Raman spectroscopy, inelastic measurements, and x-ray diffraction have been utilzed in research targeting the NBT-BT. But to date, there is still much to be discovered about NBT-BT, including its phase boundary, the

microstructure of its nanodomain distribution, and related MPB mechanisms. We do know that phase diagrams of NBT-derived solid solutions share a similar shape, as shown in Figure 1.16a-b. Specifically, the MPB is located between rhombohedral on the left and tetragonal on the right near x=5-7 for NBT-x%BT single crystal (Figure 1.16a), and near x=0.16-0.20 for NBT-x%KBT ceramics (Figure 1.16b).

Based on dielectric measurements combined with x-ray diffraction, Jo et al. reported that there are two kinds of phase boundaries for unpoled NBT-x%BT: (1) R (R3c) → R (R3m) at x=6 and (2) R (R3m) → T (P4mm) at x=11. Upon poling, a range of NBT-x%BT ($6 \leq x \leq 11$) compositions were transformed into a two-phase mixture, where the maximum piezoelectric coefficient was observed near x=7. Notice that Jo et al.'s research is based ceramic samples, which makes his phase diagram unique. In contrast, Ma et al. reported other measurements for polycrystalline ceramic samples that indicated two types of phase boundaries: R (R3c) → T (P4bm). and T (P4bm) → T (P4bm) [47].

Also, some researchers prefer the M phase to phase coexistence. Recent single-crystal neutron diffraction experiments by Gorfman et al. [48], and high-resolution x-ray powder diffraction studies of polycrystalline materials by Aksel et al. [49-51], have indicated that the structure of NBT at room temperature is the M phase of space group Cc, rather than rhombohedral R3c. In light of polarization rotation theory, we know that the bridging M phase alone cannot impart good piezoelectric properties to NBT. This theory also confirms that the M phase here is not related to MPB. Conversely, based on PNDs and ferroelectric adaptive phase theory, the macroscopic M phase can be constructed by R3C lattice and P4bm PNDs.

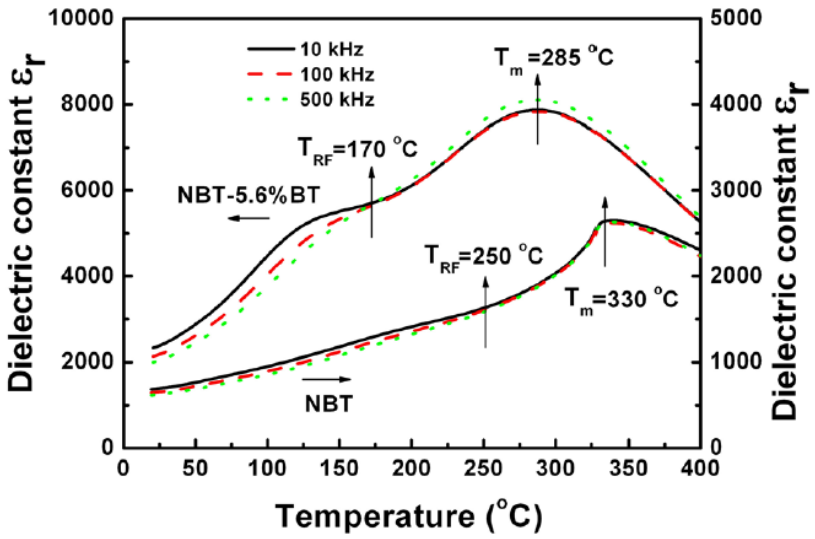

Figure 1.17: Dielectric constant ε_r of $[010]_{PC}$ oriented NBT and NBT-5.6%BT crystals as a function of temperature measured at frequencies of 10 kHz, 100 kHz, and 500 kHz. Reprint with permission from [24]. Copyright © 2014, AIP Publishing LLC.

Temperature-dependent structural changes and electric field-induced phase transition changes are also essential for understanding the precise mechanisms of these NBT-derived single crystals materials. The temperature-dependent dielectric constant curve (ε-T curve) is a common tool for determining phase boundary positioning. As shown in Figure 1.17 [24], ε-T curves of NBT-x%BT are much different from those of lead-based materials (see Figure 1.5a). Additionally, based on data obtained from phase diagrams (Figure 1.16a), NBT-x%BT only exhibits relaxor behavior near T_d, and no frequency dispersion is found near T_m. Another difference is that the dielectric constant peaks near T_d does not shift in temperature with frequency changes. As mentioned above, Ma et al. [52, 53] reported modified phase diagrams of NBT-x%BT ceramics. Based on hot stage TEM results, it was noted that PNDs with P4bm symmetry and corresponding phase coexistence account for the origin of the NBT-x%BT relaxor behavior near T_d.

Schütz et al. [54] also contributed to our understanding of these compounds. Specifically, they employed *in situ* Raman spectroscopy to confirm that the complex Bi-O bonding was broken near T_d and generated the pseudocubic structure of PNDs. These broken bonds are the source of the depolarization and subsequent external-phase-induced phase transition. Other investigators have also examined phase-induced phase transition. For example, Kling and Tan et al. [55] utilized *in situ* TEM to confirm that large ferroelectric domains form under applied electric fields in NBT-x%BT. The rapid disappearance of these domains in response to a diminishing external electric field is also consistent with the low P_r in the P-E loop. The reversible non-polar relaxor-like to ferroelectric phase transition was introduced to describe the domain evolution, and represents evidence of the existence polar nanodomains.

1.5. Objectives and significance of the study

The purpose of this investigation was to investigate the mechanism coupling between the MPB and the maximum property responses in A-site disordered perovskite Pb-free piezoelectric systems. Utilizing the theoretical framework of polar nanoregions and adaptive phase theory, this study sought to determine how the nanostructure and average structure changes with temperature and composition, as well as how these parameters impact material properties—and, in turn, how are these altered by composition, dopants, and temperature.

The specific goals of my dissertation are as follows:

- Track the structural changes with temperature variations. Specifically, I used conventional x-ray diffraction (XRD) to identify average structure with composition, temperature, and DC electric field conditions. Also, I utilized high-energy x-ray methods to study the diffuse scattering evolution (i.e., the local

structure) at Argonne National Lab, and how it evolved with changes in composition and DC electric field conditions. I also performed selected studies on ternary Pb-based MPB perovskites by x-ray diffraction in order to compare those results with analogous findings for Pb-free crystals, which represent the primary focus of my dissertation.

- Determine how temperature, composition, and dopants affect the nano-domain structure and its distribution in Pb-free piezoelectric perovskites. To achieve this goal, I used transmission electron microscopy (TEM) and selected area electron diffraction (SAED) to determine domain morphology and related distribution changes, as well as to identify various superlattice reflections and their representative tetragonal/rhombohedral phases.
- Determine the temperature-dependent phonon changes near the (200) and M-point zones using HYSPEC at Oak Ridge National Laboratory. Measurements include different compositions of NBT-x%BT crystals across the MPB. These measurements provide important insights into the dynamic nature of the underlying local structure.

The findings that emerged from these three specific goals are expected to afford a more thorough understanding of structural heterogeneous states in Pb-free piezoelectric perovskites for compositions near their MPB. The results described herein will provide insights into the average, local, and nano-sized structures of these crystals and the role of both polar and oxygen rotational order parameters over different hierarchical length scales. This information may generate additional insights into how to achieve optimum piezoelectric properties in Pb-free systems in the future.

2. Experimental procedure

2.1. Sample preparation

2.1.1. Single crystal

Compared to ceramic materials, single crystals have many advantages. For example, because there are no grain boundaries in single crystals, it is easier to determine the underlying physical mechanisms behind their structure-property relationships. Single crystals feature macroscopic symmetries that are directly related to their crystal lattice structure; thus, the resulting anisotropic properties tend to simplify fundamental research about these materials, which can then extend to their streamlined application in a variety of areas. At present, there are four principal methods for producing NBT-based single crystals: (1) the flux method, (2) the solid state growth method; (3) the Bridgman method; and (4) the top seeded-solution method, TSSG. In this investigation, all single crystals were grown using the TSSG method. The single crystals for my experiments were obtained from Prof. Haosu Luo's group (Shanghai Institute of Ceramics, Chinese Academy of Science). The compositions of each of the solid solutions for the "as-grown" condition were determined by inductively coupled plasma atomic emission spectrometry (ICPAES).

2.1.2. TEM sample preparation

TEM samples were prepared via mechanical polishing. The crystals were first cut into 2*2 mm^2 plate in order to fit the size of TEM sample holder. To meet the thickness parameters for TEM measurements, the samples were polished following a hand-to-machine polishing process. The samples were first hand-polished to less than 30um thick using a tripod and a diamond lapping film, after which copper rings were used to support the samples,

which were attached by epoxy. Finally, the samples were milled using argon ions. Liquid nitrogen was used in the ion milling process in order to reduce any associated milling damage.

2.1.3. XRD sample preparation

XRD samples were also prepared by mechanical polishing. In contrast to the TEM samples, however, there were no restrictions as to the thickness of the XRD samples. The XRD samples were typically cut into 5*5*1 mm^3 dimensions with the two larger surface planes being pseudocubic (001) or (110). Due to the large penetration depth of high-energy x-rays, XRD scattering samples were cut into small cubes along the pseudocubic (001)/(100)/(010) planes with dimensions of 2*2*2 mm^3. Silver paint electrodes were made for all XRD measurement, while any electric field was applied *in situ*.

2.2. Analysis tools

Polarization hysteresis (P-E) and strain vs E-field (ε-E) curves were measured at a frequency of 1 Hz using a modified Sawyer-Tower circuit and a linear variable differential transducer driven by a lock-in amplifier (Stanford Research, SR850). Temperature-dependent dielectric constant measurements were performed using a multi-frequency LCR meter (HP 4284A).

XRD studies were performed using a Philips MPD high-resolution x-ray diffraction (XRD) system, while XRD scattering was studied on beamline 11-ID-C at the Advanced Photon Source (APS), Argonne National Laboratory. All TEM experiments were carried out at the Virginia Tech Institute for Critical Technology and Applied Science (ICTAS), the Nanoscale Characterization and Fabrication Laboratory (NCFL). All neutron experiments

were conducting using the hybrid spectrometer (HYSPEC, BL-14B) located at the spallation neutron source (SNS) at Oak Ridge National Lab (ORNL).

2.2.1. XRD

A Philips MPD high-resolution x-ray diffraction (XRD) system was equipped with a two-bounce hybrid monochromator, an open 3-circle Eulerian cradle, and a domed hot-stage. A Ge (220)-cut crystal was employed as an analyzer, which had an angular resolution of 0.0068º. The x-ray wavelength used was CuKα = 1.5406 Å, and the x-ray generator was operated at 45 kV and 40 mA. All *in situ* XRD measurements with an applied electric field were conducted with silver paint electrodes on the samples.

2.2.2. XRD scattering

Detailed x-ray scattering was studied on a beamline 11-ID-C at the Advanced Photon Source (APS), Argonne National Laboratory, which was useful for scattering studies at extreme conditions. The high energy X-ray beam (115 keV) was highly penetrating and enabled a wide coverage of reciprocal space over a small angular scattering range. This feature is particularly advantageous for experiments that require bulky sample environments (e.g. magnets, cryostats, levitator).

Due to the large penetration depth of high-energy x-rays, diffraction information was collected from the bulk of the samples. The beam size was set to be 0.3*0.3 mm^2 by tungsten slits. The diffraction images were collected in the forward direction using a Perkin-Elmer large area detector. The samples were oscillated near the required reciprocal plane at the point at which the image was taken. This method represents a very efficient technique for measuring diffuse scattering patterns around Bragg peaks. Two-dimensional diffraction

images were integrated using the software package FIT2D, in order to obtain one-dimensional diffraction patterns of two-theta scans. The wavelength and instrumental parameters were determined by refining the profiles from standard CeO_2 samples.

In order to obtain measurements while an electric field was applied *in situ*, a dc electrical bias field was applied along the [010] direction. The sample was mounted according to the image presented in Figure 2.1. For measurements of temperature-dependent diffuse scattering changes, a Linkam TS150 was used as the hot stage. Argon air was applied during the hot stage to provide the reducing atmosphere.

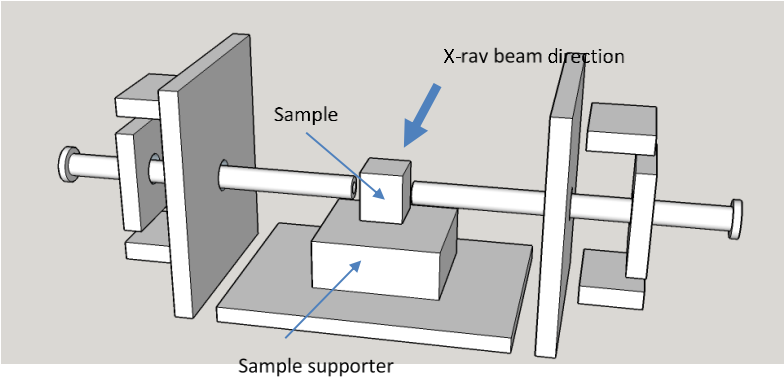

Figure 2.1: Sample mounting sketch for in situ XRD scattering measurement

2.2.3. TEM

Selected area electron diffraction (SAED) and bright field image studies were performed using a Philips EM 420 electron microscope working at 120 kV, with a double-tilt sample holder to enable access to the various zone axes. The Bragg peaks were labeled in a pseudocubic lattice index. High-resolution TEM images were obtained using a JEOL TEM working at 200kV, which elucidated nm-scale features. Note that in order to obtain the best contrast of domain structures, small tiltings of samples were performed prior to imaging. The

principal contrast mechanism of domains can be considered as diffraction contrast due to the atom displacement of dipoles.

2.2.4. Neutron scattering

All neutron experiments were conducted at the hybrid spectrometer (HYSPEC, BL-14B), which is located at the spallation neutron source (SNS) of Oak Ridge National Lab (ORNL). The layout and photo of beam line 14B, or HYSPEC/BL-14B, are showed in Figure 2.2a-b.

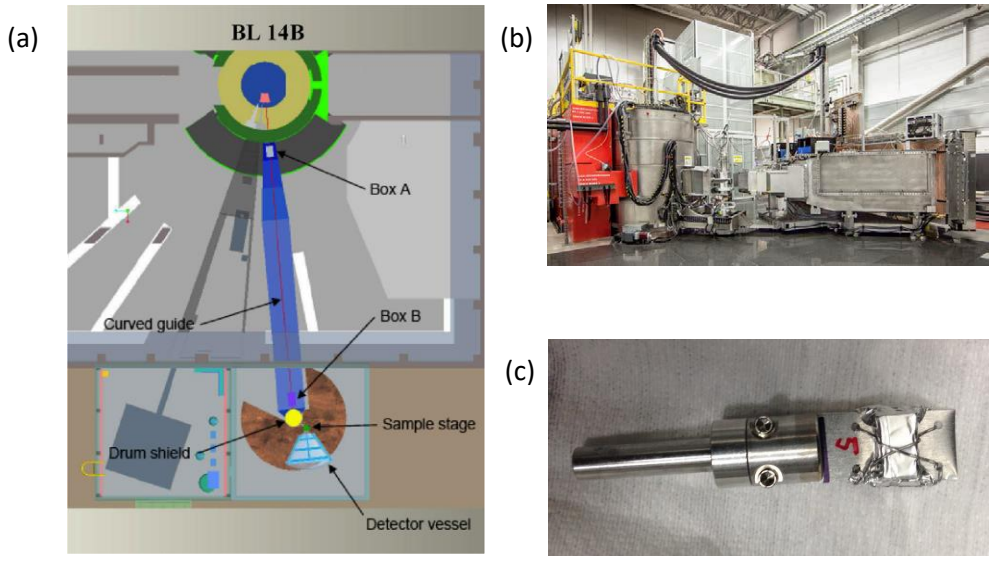

Figure 2.2: (a) HYSPEC layout. Reprint with permission from [56]. Copyright © 2006, Elsevier B.V.; (b) Photograph of the HYSPEC secondary spectrometer; (c) Single crystal alignment on Al blade.

Developed by a team from leading U.S. universities and national laboratories, in collaboration with an international group of neutron scattering experts, HYPSEC is a new concept in high-flux inelastic neutron spectrometry. This approach combines the time-of-flight technique used at pulsed sources, such as SNS, with the advantages of crystal spectrometers that use continuous neutrons. The incident neutron beam is monochromated

using a Fermi chopper and is then focused by Bragg scattering onto the sample position by either a highly oriented pyrolytic graphite (unpolarized) or a Heusler (polarized) crystal array. Neutrons are detected in a bank of position-sensitive detector tubes that can be positioned over a wide range of scattering angles around the sample axis. The combination of Fermi chopper and Bragg focusing optics, plus a position-sensitive detector bank, leads to a highly flexible instrument whereby the energy and wave vector resolution can be independently varied by nearly an order of magnitude. The region around the sample position is designed to accommodate polarization analysis. Two evolving methods of analyzing the polarization state of the scattered beam are in development: an in-house designed wide-angle quartz 3He cell to be placed in the uniform magnetic field electromagnet system, and an array of polarizing supermirrors with a m=3 polarizer coating (FeCoV) designed and constructed at the Paul-Scherrer Institut.

Neutron diffuse scattering and inelastic scattering measurements are powerful techniques for unraveling the microstructure and mechanisms underpinning the behavior of bulk piezoelectric compounds [57]. A recent study of neutron diffuse scattering comparing NBT and PMN reported both similarities and differences in the geometry of the diffuse scattering and the morphology of polar nanoregions [57, 58]. This investigation identified prominent ridges in the elastic diffuse scattering intensity contours that extend along <110>, with the same zone dependence as in PMN and other lead-based relaxors. These ridges disappear gradually on heating above the cubic-to-tetragonal phase transition temperature, T_{CT} = 523°C. It was concluded that <110>-oriented ridges are a relaxor-specific property. In addition, further ridges were also identified, which are perhaps related more to those seen in $BaTiO_3$ and $KNbO_3$, and could be related to either correlated off-centerings or anisotropic transverse acoustic phonons. This latter point remains to be elucidated.

3. Crystallographic direction-dependence of direct current field-induced strain and phase transitions in Na0.5Bi0.5TiO3-xat%BaTiO3 single crystals near the morphotropic phase boundary

Ferroelectrics with large field-induced strains are important for high-performance piezoelectric actuators. Solid solutions of $Na_{0.5}Bi_{0.5}TiO_3$-xat%$BaTiO_3$ (abbreviated as NBT-x%BT) represent potentially important lead-free piezoelectric systems—principally due to their rhombohedral (R)-to-tetragonal (T) phase transition at a morphotropic phase boundary (MPB) near 6<x<8 [5, 59]. Large field-induced strains of ~0.45% have been reported for NBT-based materials, including NBT-x%BT [25] and NBT-x%BT-y%$K_{0.5}Na_{0.5}NbO_3$ (NBT-x%BT-y%KNN) [60, 61], near the so-called depolarization temperature (T_d) below which notable frequency dispersion of the dielectric constant was identified.

The structural origin of the large strain in NBT-x%BT-based materials was recently studied using *in-situ* x-ray and neutron diffraction [62-65]. Based on the splitting of the pseudocubic (200) reflection of NBT-7%BT ceramics under an applied E-field, Daniels et al. [62, 63] proposed that the combination of an E-field-induced phase transformation from pseudocubic to tetragonal (T) structures, domain texture, and anisotropic lattice strains all contribute to the large induced strain. However, *in-situ* neutron diffraction studies have shown that large E-field-induced strain in NBT-6%BT-2%KNN [64] and NBT-6%BT [65] ceramics are accompanied by a change in the oxygen octahedral tilt system from $a^0a^0c^+$ (P4bm) to $a^-a^-a^-$ (R3c) following the Glazer notation [44]. Subsequently, an E-field-induced T (P4bm) → rhombohedral (R, R3c) transformation was proposed to be responsible for the large strain, contradictory to Daniels' results [62, 63]. Unfortunately, this contradiction has yet to be explained scientifically. Considering that a proper understanding of the correlation

between structure and properties is crucial in developing new materials, identifying the structural origin of the large induced strain in NBT-x%BT could be essential for developing lead-free piezoelectric systems with electromechanical properties approaching those of the Pb-based ones [66].

Here, I have investigated the crystallographic dependence of DC field-induced phase transitions in $Na_{0.5}Bi_{0.5}TiO_3$-5.6%$BaTiO_3$ single crystals. An induced pseudocubic → T transformation was observed for E//<001>, whereas an induced pseudocubic → R transformation was observed for E//<111>.

Figure 3.1a-b show ε-E curves for NBT-5.6%BT measured at various temperatures under a maximum DC electric field of E=20 kV/cm applied along [001] and [111]. For the [001] orientation, the ε-E curves were nearly linear and anhysteretic below 130°C. The maximum strain at 25°C was ε_{max}=0.09%. With increasing temperature, ε_{max} increased modestly to 0.12% at 80°C. At 130°C, a large increase in ε was found near E=8 kV/cm, reaching values of ε_{max}=0.60% under E=20 kV/cm. With a further increase in temperature to 150°C, ε_{max} decreased to ~0.45%. Strong hysteresis was observed for the ε-E curves at 130°C and 150°C. At 180°C, no significant induced strains were found, even for E=20 kV/cm. For [111]-oriented crystals, the ε-E curves were nearly linear and anhysteretic at 25°C. However, strongly hysteretic -E curves were observed above 80°C. The value of $_{max}$ was 0.01% at 25°C and increased by a factor of 9 to 0.09% at 80°C. The largest value for ε_{max} was 0.13%, which was obtained at 130°C; it then decreased to 0.11% upon heating to 150°C. Again, at 180°C, significant induced strains were not found for E//[111].

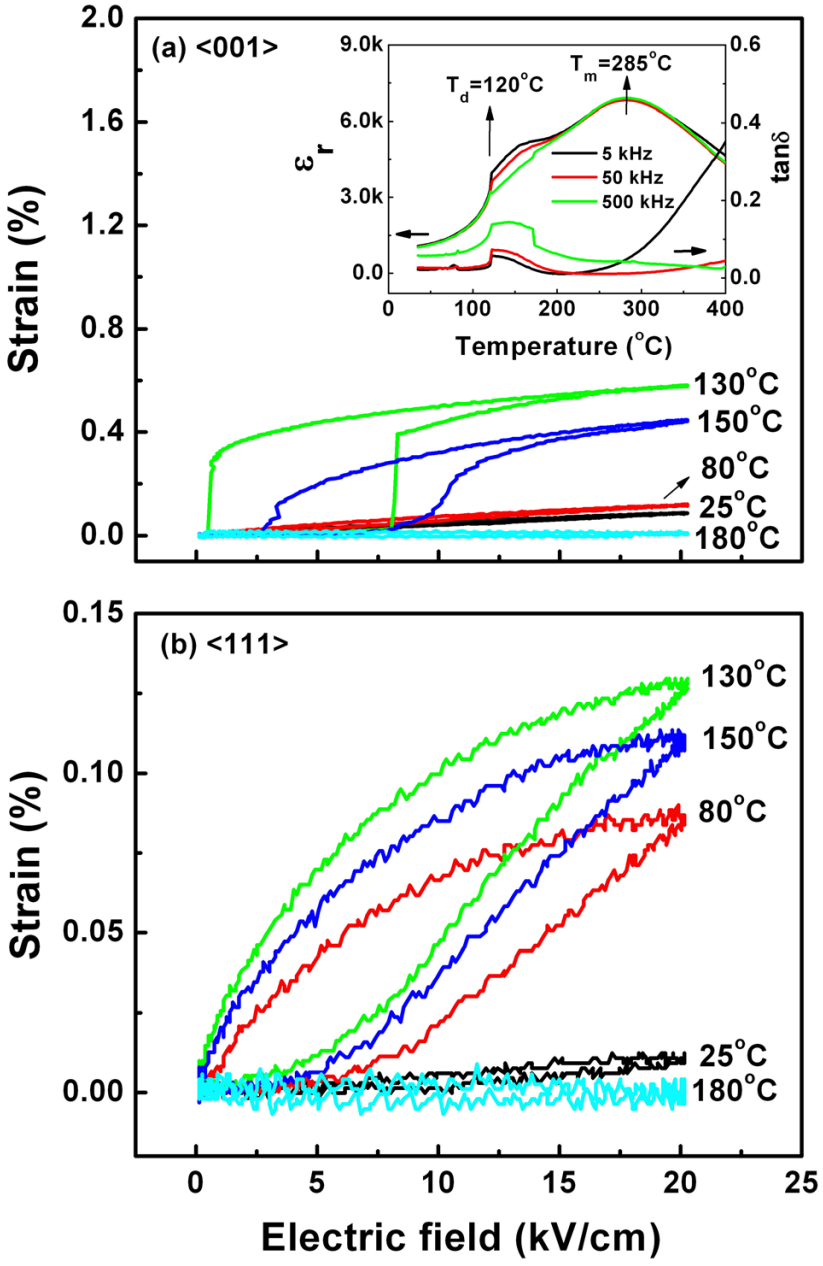

Figure 3.1: Unipolar E-field dependent strain curves measured along (a) [001] and (b) [111] under 20 kV/cm at various temperatures for NBT-5.6%BT. The inset of (a) shows the temperature dependence of the dielectric constant εr and loss factor tanδ for NBT-5.6%BT measured at frequencies of 5kHz, 50kHz, and 500 kHz.

A comparison of the normalized strain ε_{max} /E_{max}, which is an important parameter for actuator applications, was obtained for NBT-5.6%BT single crystals; our results and previously reported data for KNN-modified NBT-x%BT ceramics [60, 61] is provided in Table 3.1. This table reveals that (1) the value of $\varepsilon_{max}/E_{max}$ for NBT- 5.6%BT crystals along [001] is much higher in comparison to analogous results for the [111] orientation; and (2) the value of ε_{max} /E_{max} along both [001] and [111] significantly increased at 130^{o}C, near the depolarization temperature (T_d), above which the dielectric constant became notably frequency dispersive (see inset of Figure 3.1a). The value of T_d for NBT-x%BT compositions near the MPB was shifted to lower temperatures by doping with KNN, which also enhanced the electrically induced strain. Upon doping NBT 6%BT with 1mol.% KNN, the value of $\varepsilon_{max}/E_{max}$ increased from 240 pm/V to 310 pm/V at 25^{o}C, while T_d was decreased from 130^{o}C to 60^{o}C [61]. Similar to NBT-5.6%BT crystals (as shown in Figure 3.1), $\varepsilon_{max}/E_{max}$ was previously reported to increase to 680 pm/V near T_d (see Table 3.1) for ceramics doped with 1 mol. % KNN [61]. With a further increase of KNN content to 2mol. %, T_d was shifted to room temperature and the value of ε_{max} /E_{max} increased to 560pm/V at 25^{o}C. On the basis of temperature-dependent P-E hysteresis measurements, Jo et al. [61] proposed that the presence of a nonpolar phase results in KNN-modified NBT-6%BT returning to its unpoled condition after the removal of E, which in turn results in an enhancement of ε_{max} /E_{max} near T_d. Previous structural investigations have suggested two different explanations for this enhancement of $\varepsilon_{max}/E_{max}$ near T_d: (1) pseudocubic → T [62, 63], and (2) T (P4bm) → R (R3c) [64, 65] transformations. However, as documented in Table 3.1, it can be seen that the enhancement of $\varepsilon_{max}/E_{max}$ near T_d for NBT-5.6%BT crystals is dependent upon the crystallographic direction along which E is applied. It is important to note that this enhancement was more pronounced for crystals relative to ceramics. Thus, it is important to further identify the mechanisms associated with this $\varepsilon_{max}/E_{max}$ enhancement in crystals. Such an understanding

could be important to the development of lead-free piezoelectrics with giant strains for actuator applications.

Material	$\varepsilon_{max}/E_{max}$ (pm/V)	Measured temperature (°C)
⟨001⟩-oriented NBT-5.6%BT crystal	450	25
⟨111⟩-oriented NBT-5.6%BT crystal	50	25
⟨001⟩-oriented NBT-5.6%BT crystal	3000	130
⟨111⟩-oriented NBT-5.6%BT crystal	650	130
94NBT-6%BT ceramics	240	25
93NBT-6%BT-1%KNN ceramics	310	25
93NBT-6%BT-1%KNN ceramics	680	60
92NBT-6%BT-2%KNN ceramics	560	25

Table 3.1: The comparison of εmax/Emax for NBT-5.6%BT crystals with previously reported data for KNN-modified NBT-6%BT ceramics.

Figure 3.2a and Figure 3.2b show ω-2θ area scans at 130℃ for NBT-5.6%BT crystals under E=0 kV/cm taken at about $(002)_{PC}$ and $(111)_{PC}$, where PC stands for pseudocubic. A single sharp peak can be seen along each zone. No information concerning oxygen octahedral tilt reflections was obtained since the reflections were too weak to be measured using a high-resolution lab diffractometer. Prior transmission electron microscopy (TEM) studies have revealed the coexistence of ferroelectric PNR of R3c and P4bm symmetry in NBT-x%BT near the MPB [59, 67], but the average long-range symmetry may be cubic. Thus, the phase structure of NBT-5.6%BT for E=0 in the present study is referred to as pseudocubic, as previously reported [62, 63, 65]. The pseudocubic lattice parameters were a=3.9096+-0.002A ° for E=0 kV/cm at 25℃.

Two different E-field-induced transformations were then observed for NBT-5.6%BT crystals under E applied along [001] and [111] at 130°C. For E//[001], the (200) reflection in the ω-2θ area scan for E=10 kV/cm split along both the 2θ and ω axes (see Figure 3.2c); in contrast, the (111) reflection [65]n split only along the x-axis in the ω-2θ area scan (see Figure 3.2d). The 2ω positions of these peaks were found at 2θ=46.073, 46.662, and 39.952 for the (200) and (111) reflections. These results revealed two d spacings for the (200) reflection and one d spacing for the (111) reflection according to the Bragg law, i.e., $2d_{hkl}\sin\theta_{hkl}=n\lambda$, where (hkl) is reflection indices. These results demonstrate an E-field-induced pseudocubic to T transition for E//[001] under 10 kV/cm. The lattice parameters for the induced T phase were (a_t, c_t)=(3.890, 3.937)±0.002Å. Despite the fact that the peaks split along the x-axis for the $(200)_T$ and $(111)_T$ reflections, these peaks are at the same 2θ positions. This result indicates that these reflection peaks resulted from tilted domains having the same d-spacing to release strain generated during E-field-induced pseudocubic → T transition. However, for E//[111], a 2θ splitting was observed about the (111) reflection in the ω-2θ for E=4 kV/cm (see Figure 3.2f), but no splitting was observed around the (200) (see Figure 3.2e). These data demonstrate that an E-field induced pseudocubic to R transition occurs under E//[111] for 4 kV/cm. The lattice parameters of this induced R phase were (a_r, a_r)=(3.908Å, 89.78°).

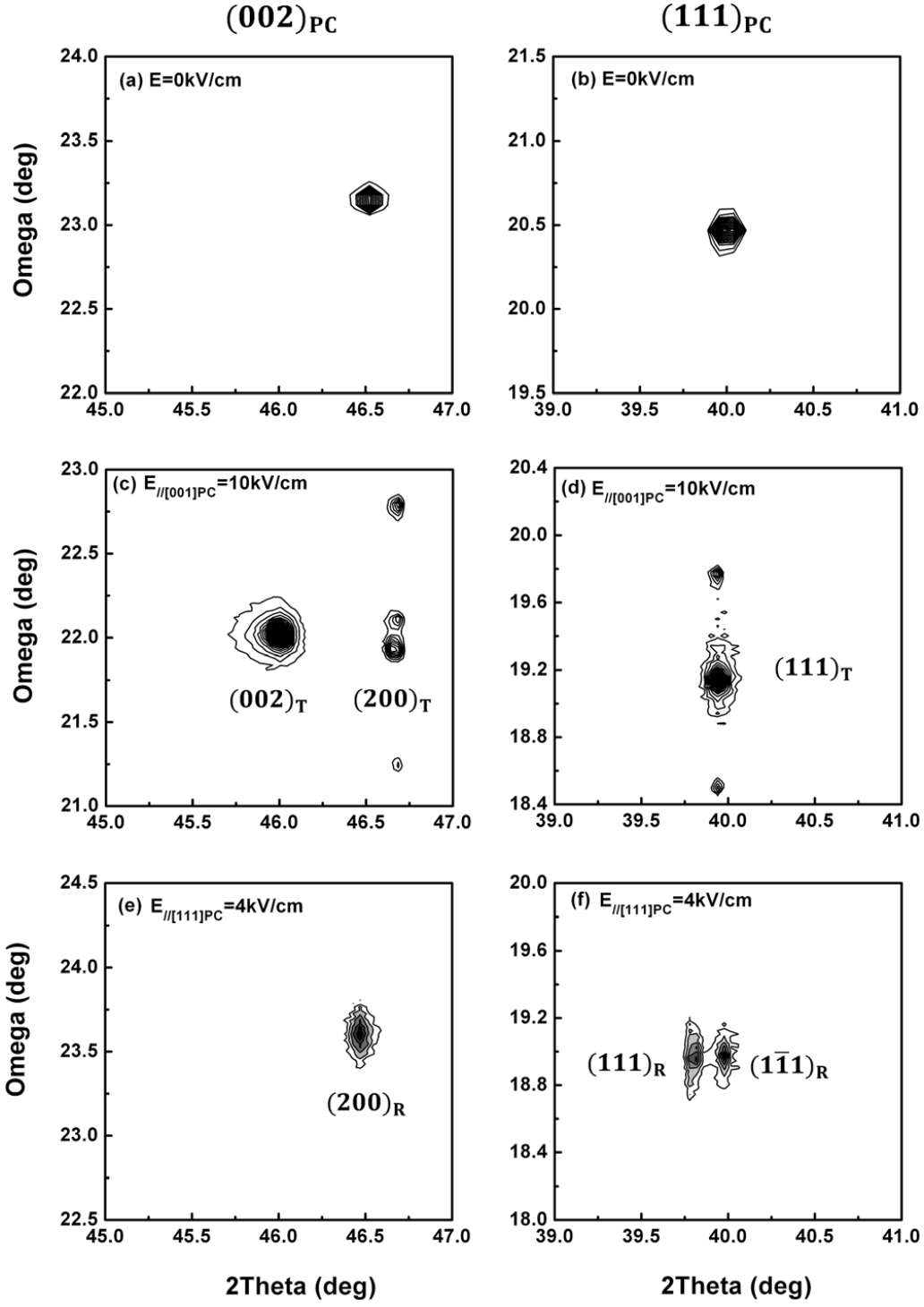

Figure 3.2: ω-2theta maps taken along the (002)PC and (111)PC zones at 130℃: [(a) and (b)] under zero E, [(c) and (d)] under E//[001]$_{PC}$=10 kV/cm, and [(e) and (f)] under E//[111]$_{PC}$=4 kV/cm.

Figure 3.3a and Figure 3.3b show the E-field-dependent lattice parameters at 130°C for E applied along the [001] and [111] directions, respectively. For E//[001], the lattice parameters of the pseudocubic structure increased with increasing field for E=8 kV/cm. With increasing E to 10 kV/cm, a tetragonal splitting of c/a=1.012 became apparent, demonstrating an induced phase transformation. Please note that the ε-E curve for [001] at 130°C exhibited a jump at E=8 kV/cm (see Figure 3.1a), near to where the induced pseudocubic → T transition occurs. These data show that the enhancement of $\varepsilon_{max}/E_{max}$ near T_d for [001]-oriented crystals is due to this induced transformation. For E//[111], an obvious R distortion appeared with increasing field near E=4 kV/cm, where the rhombohedral angle was a_r=89.78°.

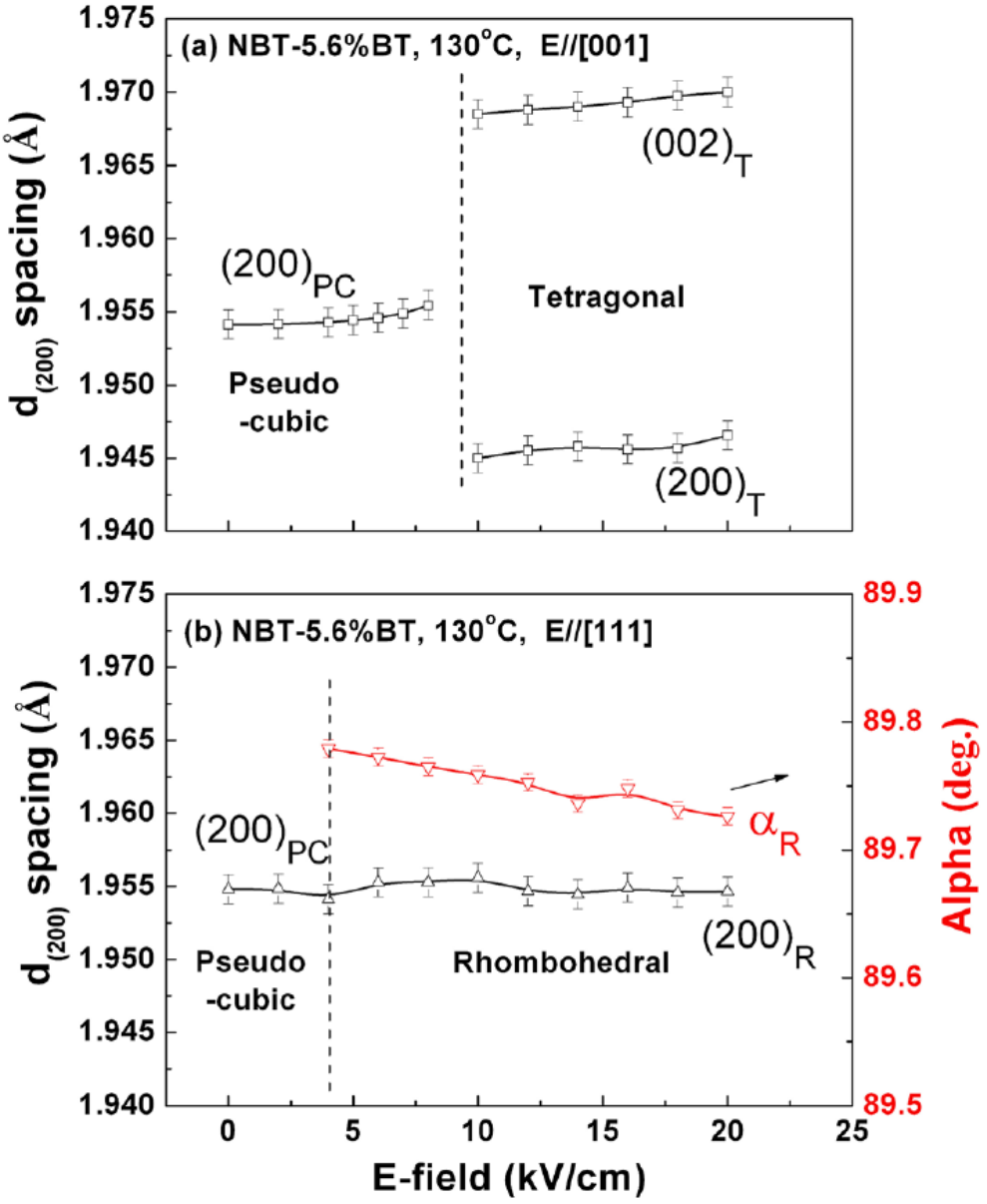

Figure 3.3: Electric field-dependent d spacing of (200) for NBT-5.6%BT at 130°C under (a) E//[001], and (b) E//[111].

These structural results show that the E-field-induced phase transformations in NBT-5.6%BT crystals are dependent on the crystallographic direction along which E is applied. Specifically, an induced pseudocubic → T transition was observed near E=10 kV/cm for E//[001], whereas an induced pseudocubic → R one was found for E//[111]. Although NBT-x%BT crystals of

compositions close to the MPB have been found to be pseudocubic under zero field, TEM studies have revealed the coexistence of polar nanoregions with an $a^0a^0c^+$ in-phase oxygen octahedral tilting (P4bm structure), and an $a^-a^-a^-$ anti-phase oxygen octahedral tilting (R3c structure). [67] In the polar nanoregions with a P4bm structure, the Na^{1+}/Bi^{3+} and Ti^{4+} cations displace almost equally in opposite directions along the $[001]_{PC}$, resulting in the T (P4bm) phase being only weakly polar. [46] In the polar nanoregions with an R3c structure, the displacement of the Na^{1+}/Bi^{3+} and Ti^{4+} cations are parallel along the $[111]_{PC}$ axis. [46] The crystallographic dependence of the induced phase transformations can be attributed to the response of T and R polar nanoregions under E applied along their respective polar directions. Near the MPB, either the R or T phases can be induced, depending on the direction along which E is applied, as the two phases are nearly thermodynamically degenerate.

The crystallographic orientation-dependent E-field phase stability has previously been reported for PMN-x%PT near the MPB [68-70]. For PMN-30%PT single crystals, an E-field-induced R → Monoclinic A (Cm) → Monoclinic C (Pm) → T phase transformation sequence was reported for E applied along [001] [70]. In contrast, an E-field-induced R → Monoclinic B (Cm) sequence was found for E applied along [111] [69]. These low symmetry monoclinic phases allow the polarization vector to rotate within a plane under E, which gives rise to an enhanced piezoelectric response near the MPB [71]. Compared to PMNx%PT, NBT-x%BT near its MPB has a unique feature: its polar nanoregions feature both $a^0a^0c^+$ in-phase oxygen octahedral tilting (P4bm structure) and $a^-a^-a^-$ anti-phase oxygen octahedral tilting (R3c structure) simultaneously [67]. However, no low symmetry monoclinic phases and only T and R phases were induced from the initial pseudocubic one under E//[001] and E//[111] for NBT-5.6%BT crystals. These results indicate that both E-field-induced pseudocubic → T and pseudocubic → R transitions contribute to the enhanced strain properties in NBT-x%BT

ceramics near the MPB compositions. However, the induced phases showed strong domain texture in ceramics with the polarization aligning preferentially parallel to the E-field [62, 65]. Thus, only splitting of (002)/(200) peaks for the tetragonal distortion was detected in NBT-7%NBT [62] and NBT-x%BT-y%KNN [63] ceramics under the experiment configuration of scattering vectors parallel to the E-field in prior high-energy x-ray scattering experiments. The splitting of (111)/(1$\bar{1}$1) peaks for the rhombohedral distortion in NBT-6%BT ceramics were reported at an angle of 30^{o}–50^{o} for the scattering vectors with respect to the E-field, which is consistent with crystallographic orientation-dependent E-field phase stability in NBT-5.6%BT single crystals described herein.

In summary, the crystallographic dependence of DC electric field-induced strains and phase transitions in $Na_{0.5}Bi_{0.5}TiO_3$-5.6%$BaTiO_3$ single crystals were investigated. An induced transition between pseudocubic and T structures was observed under E=10 kV/cm for E//[001], whereas an induced transition between pseudocubic and R structures was observed for E//[111]. Our results indicate that phase stability for compositions close to the MPB boundary is dependent on the direction along which E is applied.

4. Evolution of structure in Na0.5Bi0.5TiO3 single crystals with BaTiO3.

The piezoelectric properties of NBT can be enhanced via the incorporation of x mol.% $BaTiO_3$ (BT) to form an MPB between T and R phases near x=6–8 [5]. Structural investigations have shown that the T (P4bm) phase of NBT shifts to lower temperatures after BT modification, and that the tetragonal distortion c/a is significantly decrease. [64, 65, 72]. Recently, the phase diagram of NBT-x%BT has been extensively studied using different experimental techniques, including Raman spectroscopy [73], anelastic measurements [74], x-ray diffraction [59], and transmission electron microscopy [52, 53]. To date, however, there is still disagreement as to the nature of the phase boundary of NBT-x%BT. According to dielectric measurements combined with x-ray diffraction obtained by Jo et al. [59], there are two kinds of phase boundaries for unpoled NBT-x%BT: (1) R (R3c) → R (R3m) at x=6 and (2) R (R3m) → T (P4mm) at x=11. The researchers reported that a range of compositions, from NBT-6%BT to NBT-11%BT, became two-phase mixtures upon poling, where the maximum piezoelectric coefficient was observed near x=7 [59]. However, based on domain morphology and electron diffraction pattern changes as a function of composition, which were noted via TEM, two types of phase boundaries have been reported for unpoled NBT-x%BT [52, 53], but of different phase sequence: (1) R3c → P4bm near x=6.5 and (2) P4bm → P4mm near x =10. The principal difference between the phase diagrams reported by Jo et al. [59] and Ma et al. [52, 53] pertain to whether the R3m or P4bm phases are sandwiched between R3c and P4mm phases near the MPB. In 2013, a possible phase boundary of Cc → R3c near x=3–4 in NBT-x%BT was also suggested by analyzing the superlattice diffractions corresponding to the octahedral tilting using selected area electron diffraction [75].

Recent single-crystal neutron diffraction experiments [48] and high-resolution x-ray powder diffraction studies of polycrystalline materials [49-51] have indicated that the room-temperature structure of NBT is the monoclinic (M) of space group Cc rather than rhombohedral R3c. High-resolution x-ray powder diffraction studies have confirmed that the phase transition near the MPB between the R and T phases in lead-based piezoelectric materials occurs via structurally-bridging M phases. The high electromechanical response is believed to be related to symmetry-allowed polarization rotations via the M phases [37, 76]. However, a number of earlier investigations have shown that unmodified NBT exhibits low piezoelectric coefficients [5, 59]. The identification of an M phase in NBT-x%BT implies that the M phase in and of itself might not guarantee high piezoelectricity [10]. Therefore, it would be interesting to study the structures of compositions of NBT-x%BT near the MPB using high-resolution x-ray powder diffraction in order to determine the degree of structural similarity between lead-free NBT-x%BT and lead-based PMN-x%PT crystals. Such an investigation might be useful in understanding the overall mechanisms by which high piezoelectricity is obtained in NBTx% BT—and in particular whether the R3m or P4bm phases are sandwiched between the R3c and P4mm phases in NBT-x%BT near the MPB [52, 53, 59].

Herein, we report high-resolution x-ray powder diffraction studies of NBT-x%BT single crystals near the MPB for x=0, 5, 6, and 7. Our results are summarized in Figure 4.1 with solid symbols. To summarize, we found that the M (Cc) and T (P4bm) phases coexisted near the MPB for NBT-x%BT.

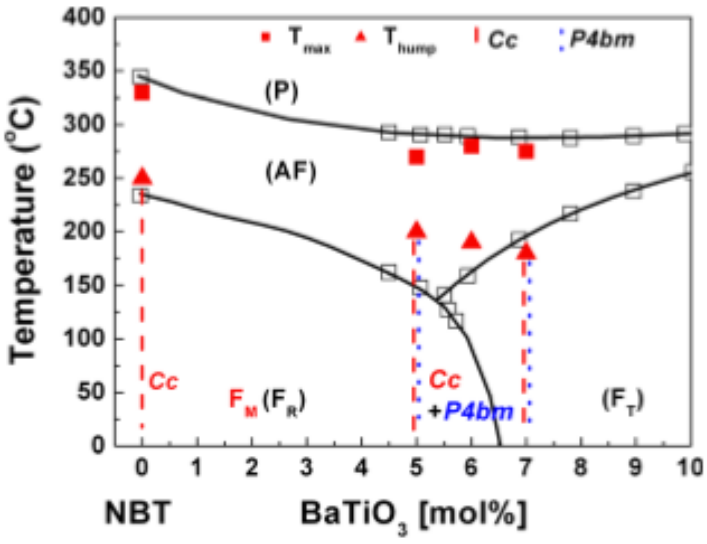

Figure 4.1: Modified $Na_{0.5}Bi_{0.5}TiO_3$-xat%$BaTiO_3$ phase diagram. Data provided by Takenaka et al. [5] are plotted as open squares. The T_{max} and T_{hump} of this work are plotted as solid squares and triangles. M=monoclinic, T=tetragonal, R=rhombohedral, P=paraelectric, AF=antiferroelectric, F=ferroelectric. Solid lines drawn through these data point serve as visual guides. The dashed line represents the structural refinement using Cc model for NBT. The bundle of dashed lines and dotted lines represents the structural refinements using CcþP4bm models for NBT-x%BT. The bracketed P, AF, FR, and FT are based on prior studies by Takenaka et al. Adapted with permission from Takenaka et al., Jpn. J. Appl. Phys., Part 1 30(9B), 2236 (1991). @ Copyright 1991 by The Japan Society of Applied Physics.

High-resolution x-ray diffraction studies was performed in a transmission mode geometry using the synchrotron radiation diffraction beamline 11-BM (λ=0.413629Å) at the Advanced Photon Source (Argonne National Laboratory). The diffractometer had a unique multi-analyzer detection assembly, consisting of 12 independent Si (111) crystal analyzers and $LaCl_3$ scintillation detectors. This configuration enables simultaneous high-speed (~1 h) and high-resolution ($\Delta Q/Q \sim 2x10^{-4}$) data collection. Powdered NBT-x%BT (x=0, 5, and 7)

samples for x-ray diffraction were obtained from ground crystals. The powders were then loosely packed in 0.8mm Kapton capillaries and spun at 60 Hz during data collection to improve powder crystallite averaging. The diffraction patterns were measured at room temperature using a monochromatic x-ray beam. Crystal structure analysis was carried out via Rietveld refinement using the GSAS program package [77]. Pseudo-Voigt peak shape [78] and cosine Fourier series background functions were chosen. The wavelength and instrumental parameters were determined by refining the profiles from standard LaB_6 samples.

Figure 4.2a-d illustrates the dielectric constant ε_r and loss factor tanδ as a function of temperature for $(001)_{PC}$-oriented NBT-x%BT crystals (x=0, 5, 6, and 7), obtained upon heating. The results reveal a diffuse phase transformation with a broad dielectric maximum near T_m=330ºC for NBT—near but just below the point at which the dielectric constant was frequency-independent. Below a lower temperature of T_{hump} ($<T_m$), the dielectric constant exhibited a strongly frequency-dependent anomaly [73]. The dielectric anomaly near T_{hump} has been attributed to the thermal evolution of polar nanoregions (PNRs) from R3c to P4bm symmetries [79]. Neutron diffraction studies have revealed that the R3c PNRs coexist with P4bm PNRs in NBT and NBT-x%BT below T_{hump}, but then gradually disappear with increasing temperature above T_{hump}. In contrast, the P4bm PNRs evolve into long range ordered P4bm structures above T_{hump}; therefore, the dielectric frequency dispersion disappears above the T_{hump} temperature. [57] In crystals substituted with x%BT, both T_m and T_{hump} shifted towards lower temperatures. The magnitude of the dielectric constant and frequency dispersion was strongly increased with increasing BT content for $0<x<7$ at. %. Figure 4.2e shows the room temperature values of ε_r and tanδ as a function of x%BT. It can be seen that the value of ε_r was increased by >400% with increasing BT content for compositions near the

MPB. The piezoelectric d_{33} and electromechanical K_t coefficients as a function of x% displayed peak values of 423 pC/N and 68% for x=5%, as shown in Figure 4.2f.

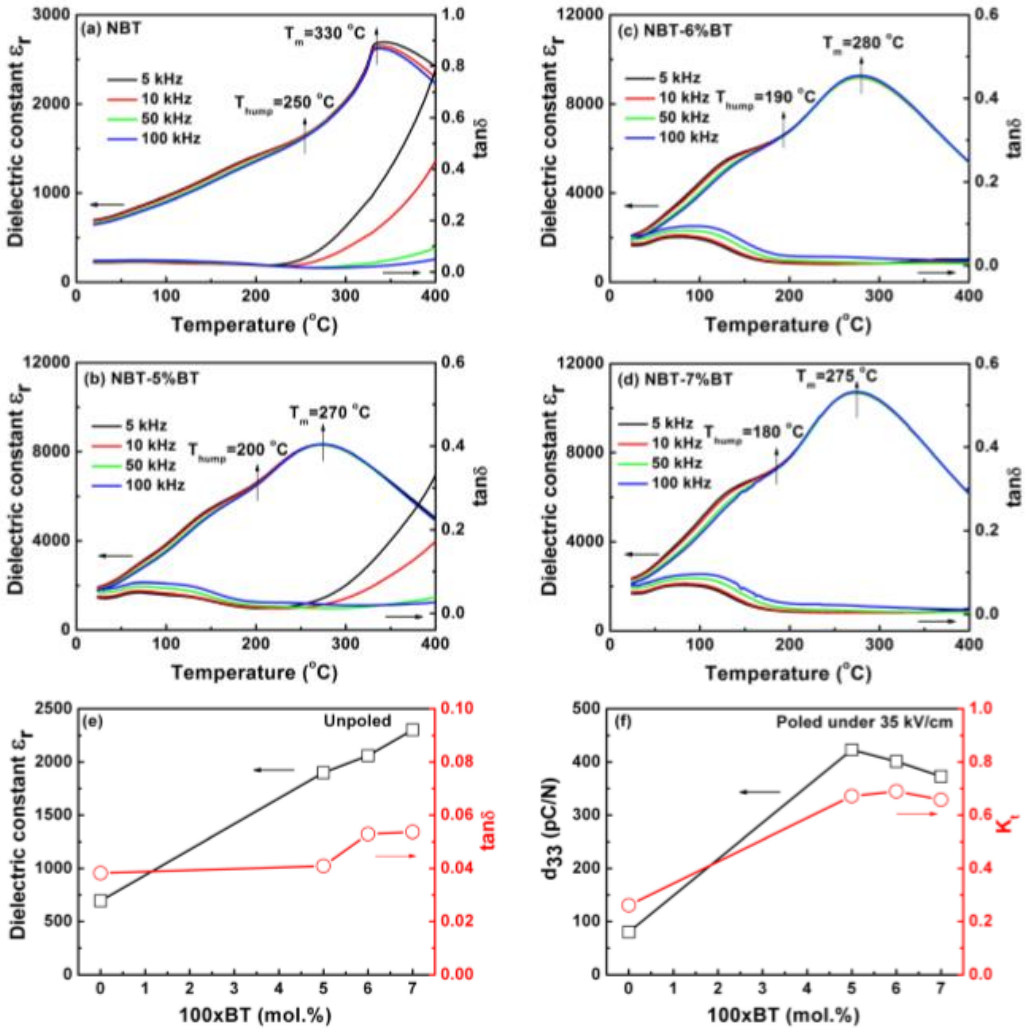

Figure 4.2: (a-d) Temperature dependence of the dielectric constant ε_r and loss factor tanδ for NBT, NBT-5%BT, NBT-6%BT, and NBT-7%BT. (e) Composition dependence of ε and tanδ. (f) Composition dependence of piezoelectric d_{33} constant and electromechanical coefficient K_t.

Figure 4.3a-c show Rietveld refinement structural analysis for NBT, NBT-5%BT, and NBT-7%BT. Observed and calculated diffraction profiles are indicated by cross markers and solid lines. The difference plots are shown below the data in each figure, and the short vertical markers represent the peak positions. For NBT, the refinement best fit the Cc space group, similar to previous reports by Aksel et al. [49-51], which produced a good fit with a profile R value of Rp=5.40% (see Figure 4.3a). For NBT-5%BT and NBT-7%BT, the refinement best fit to a combination of Cc and P4bm space groups—with Rp=5.91% and 6.51%, respectively (see Figure 4.3b-c). The volume fractions of the T (P4bm) phase were 6.11% and 6.53% for NBT-5%BT and NBT-7%BT, respectively. The refined lattice parameters are provided in Table 4.1, which confirms that the lattice parameters of the M (Cc) and T (P4bm) phases for NBT-x%BT increased with increasing BT content. This trend can be attributed to the fact that the ionic radius of Ba^{2+} (1.34Å) is 40% larger than that of Na^{+} and Bi^{3+} (0.97Å). The evolution of the $(110)_{PC}$, $(111)_{PC}$, and $(200)_{PC}$ profiles with BT content is shown in the insets of Figure 4.3a-c. The distortions for both $(110)_{PC}$ and $(200)_{PC}$ increased with increasing BT content. In fact, the $(200)_{PC}$ exhibited a clear splitting for NBT-7%BT. These data demonstrate a transformation from an M (Cc) phase to a T(P4bm) phase having a weak tetragonal distortion of $\sqrt{2}c/a$=0.051% and 0.087% for NBT-5%BT and NBT7%BT, respectively.

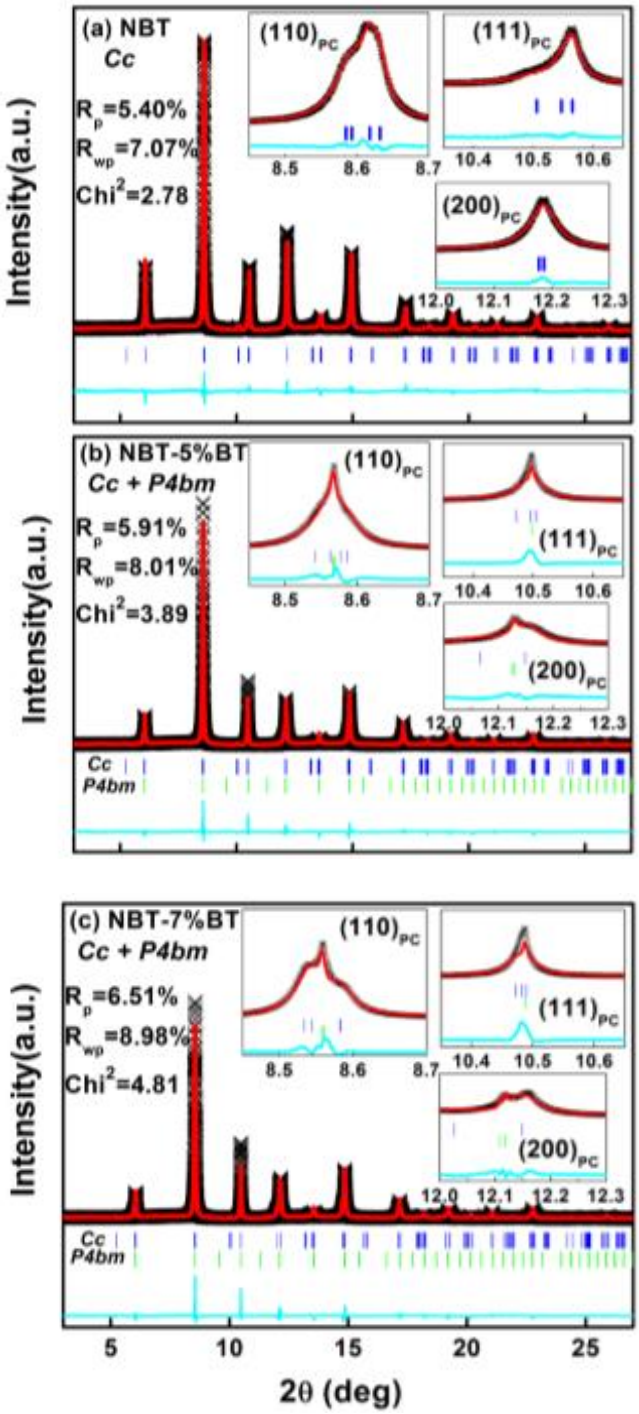

Figure 4.3: Observed and calculated (Rietveld refinements) diffraction profiles of (a) NBT, (b) NBT-5%BT, and (c) NBT-7%BT, respectively. Difference plots are shown below, where short vertical markers represent peak positions. The insets in each figure highlight the evolution of $(110)_{PC}$, $(111)_{PC}$, and $(200)_{PC}$ profiles with $BaTiO_3$.

The coexistence of R (R3c) and R (R3m) at x= 6 has previously been reported for NBT-x%BT [59]. In this investigation, the R3c and R3m space groups were considered during refinements, but subsequently dismissed as possible structural models for NBT-5%BT and NBT-7%BT. The observed intensity profiles could not be fully described using a model of R3c and R3m phase coexistence, as it afforded notably inferior profile R values (Rp=9.32%, Rwp=12.43%, and Chi2=9.39) in comparison to a model of Cc and P4bm phase coexistence (Rp=5.91%, Rwp=8.01%, and Chi2=3.89) for NBT-5%BT. We also considered the possibility of CcþR3m phase coexistence during refinements, which afforded higher profile R values (Rp=9.94%, Rwp=12.92%, and Chi2=10.13) for NBT-5%BT. Structural Rietveld refinements with a model of Cc + R3c was also considered for NBT 5%BT. However, this model also failed to describe the observed intensity profiles and higher profile R values (R p=6.91%, Rwp=9.73%, and Chi2=5.75), which, again, were inferior to best fit data associated with a Cc + P4bm model. Thus, the Cc + R3m and Cc + R3c models were both excluded in this work.

Symmetry	Lattice parameters	NBT	NBT-5%BT	NBT-7%BT
Cc	a (Å)	9.5473	9.6060	9.6183
	b (Å)	5.4788	5.5078	5.5107
	c (Å)	5.5091	5.5142	5.5111
	β (°)	125.477	125.226	125.060
	Cell volume (Å^3)	234.670	238.323	239.103
P4bm	a = b (Å)	…	5.5194	5.5245
	c (Å)	…	3.9048	3.9098
	Cell volume (Å^3)	…	118.955	119.328
Mass% of *P4bm* phase		0	6.11	6.53

Table 4.1: Structural results for the NBT-x%BT.

Figure 4.1 (shown earlier in this chapter) summarizes our structural results for NBT-x%BT. The open squares represent the work by Takenaka et al. [5]. The solid curves drawn through these data points serve as visual guides. The solid squares represent the temperature T_{max}, which corresponds to the dielectric maximum, and the triangles indicate the T_{hump} below which dielectric dispersion was observed (these data were obtained from Figure 4.2a-d). The dashed line represents the structural refinement using the Cc model for NBT. The bundle of dashed and dotted lines represents the structural refinements using the Cc + P4bm phase coexistence model for NBT-x%BT. The bracketed symbols of P, AF, FR, and F T represent the paraelectric, anti-ferroelectric, ferroelectric rhombohedral, and ferroelectric tetragonal phases of NBT-x%BT based on prior studies by Takenaka et al. [5]. The FM symbol represents the ferroelectric monoclinic (Cc) phase based on this work. The Cc phase has antiphase octahedral rotations of the $a^-a^-c^-$ (Ref. 38) along the $(100)_{PC}$, $(010)_{PC}$, and $(001)_{PC}$ directions. In contrat, the P4bm phase has in-phase octahedral rotations of the $a^0a^0c^+$ type along the $(001)_{PC}$ direction (Glazer notation [44]). These results indicate that substituting Na^+/Bi^{3+} ions with Ba^{2+} suppresses the anti-phase octahedral rotations in NBT, yielding a phase boundary between M (Cc) and T (P4bm) near x=5 to 7, which is the level at which enhanced piezoelectric and dielectric properties are facilitated. These findings indicate that the phase boundaries for unpoled NBT-x%BT near x=5–7 are neither R (R3c) → R(R3m) [59], nor R (R3c) → T(P4bm) [52, 53], as previously reported. However, both Jo et al. [59] and Ma et al. [52, 53] did report that NBT-x%BT would evolve into a T (P4mm) phase near x=10%. Combined with the present work, the MPB for NBT-x%BT might be described as a phase coexistence of weak polar T (P4bm) and M (Cc) phases for 5<x<7% that sandwiches the M (Cc) and T (P4mm) phases at lower and higher x%.

It should be noted that the MPB in NBT-x%BT is different than the MPB for the well-known PZT, PMN-PT, and PZN-PT compounds. In these lead-based piezoelectric solid solution systems, the M phases are structurally intermediate phases that bridge the R and T phases near the MPB [4]; however, the M phase in NBT-x%BT is not an intermediate phase. High piezoelectricity in Pb-based MPBs [63] can be attributed to the structural instability between the R and T phase, which occurs as a result of polarization rotation in an M phase [29,30]. However, for NBT-x%BT, piezoelectric property enhancement from structural instability via polarization rotation cannot be fully achieved due to the fact that a weakly polar T (P4bm) sandwiches the M (Cc) and T (P4mm) phases. In summary, the structure of NBT-x%BT was investigated using high-resolution synchrotron x-ray powder diffraction. Structural Rietveld refinement using GSAS revealed a phase boundary between M (Cc) and T (P4bm) near x=5–7, which is the point at which the dielectric and piezoelectric properties were enhanced.

5. Hierarchical domain structure of lead-free piezoelectric $(Na_{1/2}Bi_{1/2})TiO_3$-$(K_{1/2}Bi_{1/2})TiO_3$ single crystals.

Near the MPB in Pb-based single crystals, such as $Pb(Mg_{1/3}Nb_{2/3})O_3$-xat%$PbTiO_3$ (PMN-x%PT) and $Pb(Zn_{1/3}Nb_{2/3})O$- xat%$PbTiO_3$ (PZN-x%PT), various structurally bridging monoclinic (M) phases are known to exist [80]. These phases facilitate polarization rotation with significantly reduced hysteretic losses within a domain-engineered state [81] between the ferroelectric rhombohedral (R) and tetragonal (T) phases. Following the successful development of MPB compositions of PMN-x%PT and PZN-x%PT single crystals with high piezoelectric properties [1], investigations of next-generation Pb-free piezoelectrics have focused on NBT-xat%$BaTiO_3$ (NBT-x%BT) crystals [82], due to the presence of a similar MPB in its phase diagram between the R (R3c) and T (P4bm) phases, as illustrated in Figure 1.16a [24]. Significant enhancements in the piezoelectric properties (d_{33}=423pC/N after poling [24]) have been found in NBT-x%BT near the MPB composition. However, these enhancements have not yet been found to be as significant as those of Pb-based ones ($d_{33}\approx$2500pC/N [1]), whether at the MPB or not. The reasons for the reduced properties in the Pb-free crystals versus Pb-based crystals have yet to be elucidated.

It is widely believed that polar nanodomains (PNDs) play an important role in the MPB systems of both Pb-based and Pb-free piezoelectric. [45, 83]. In PMN-x%PT, the presence of PNDs that self-assemble into hierarchical domains over various length scales has been reported [41]. This phenomenon results in achieving the compatibility conditions of the elastically relaxed state [41]. In such instances, adaptive phase theory [38] predicts that the structurally bridging M phases are, in fact, composed of nanodomains of R and T phases, and that the high piezoelectric properties result from a redistribution of the PNDs. In NBT,

hierarchical domains have also been reported, where a high-temperature ferroelastic T domain structure is elastically inherited into the R ferroelectric phase field, and where polar domains of about micron-size form within this geometrical constraint, as illustrated Figure 1.16c [43]. With increasing BT content, and as NBT-x%BT approaches the MPB, the size of the polar domains was reported to be refined, and the degree of self-organization in the domain hierarchy enhanced [43, 45]. Furthermore, high-resolution transmission electron microscopy (HRTEM) images have confirmed the presence of multiple oxygen octahedral tilt domains (generally a few nanometers in size) within the lamellar domains [84]. Both types of superlattice reflections—in-phase tilt ½(ooe) and anti-phase tilt ½(ooo) (where o designates odd values of the Millers indices, and e even)—were reported in NBT-5.5%BT, as illustrated in Figure 1.16d [45]. The in-phase tilt reflection is believed to originate from a T (P4bm) structure with an a0a0c+ tilt system, while the anti-phase tilt reflection likely originates from an R (R3c) structure with an a-a-a- tilt system (Glazer notation [44]). With increasing BT content (approaching the MPB), the intensity of the ½(ooe) reflections and the volume fraction of the in-phase tilt domains were found to increase [45]. Both types of tilt domains were also found to be present over a large temperature range, with their respective volume fractions changing gradually with temperature [57]. These results indicate the presence of PNDs with a structural frustration on the nm-scale between tilt clusters, which gradually evolve with changes in temperature and composition.

Recently, solid solutions of NBT-x%$(K_{1/2}Bi_{1/2})TiO_3$ (NBT-x%KBT) in single crystalline form were found to achieve promising performance [27, 28, 54, 85, 86]. Table 5.1 summarizes the dielectric and piezoelectric properties of NBT-x%KBT crystals grown by a top-seed solution growth (TSSG) method, as well as other previously reported results [27, 87, 88]. As shown in this table, the value of d_{33} is enhanced in the vicinity of the MPB, while the

remnant polarization (P_r) is suppressed [27]. In particular, this material has a high depolarization temperature and a large k_t/k_p ratio (thickness-to-planar coupling coefficient) [27], both of which have been critically limiting issues for PMN-x%PT and PZN-x%PT [89]. In contrast, the characteristics of NBT-x%KBT solid solutions are promising for applications. Nonetheless, the domain structure of NBT-x%KBT single crystals are not yet fully understood, meriting further investigation.

Materials	*ε_r(1kHz)*	*tanδ(1kHz)*	*P_r($\mu C/cm^2$)*	*E_c(V/mm)*	*d_{33}(pC/N)*	*k_t*	*Reference*
NBT-50%KBT	~1000	-	-	-	160	0.49	[27]
Mn-NBT-8%KBT	732	0.018	29.4	4.4	196	0.56	[28]
NBT-5%KBT	909.4	0.038	18	4.2	148	0.38	[22]
NBT-8%KBT	876.5	0.039	13	4.0	175	0.52	

Table 5.1: Electrical properties of NBT-x%BT single crystals

Here, we present the results of our investigation into the domain hierarchy of NBT-x%KBT single crystals for x=0.05 and 0.08. Specifically, the domain structure of these compounds were studied via transmission electron microscopy (TEM) in the bright field (BF) mode, selected area electron diffraction (SAED), and dark field (DF) imaging. In addition to the similar polar domain structure previously reported for NBT [90], an even finer nano-sized sub-domain structure was observed by HRTEM, which self-assembled into a quadrant-like configuration. The density of these sub-domains was found to decrease with increasing KBT content, while SAED-derived patterns revealed that the octahedral tilt regions and phase coexistence did not significantly change.

As shown in Figure 5.1, bright field images were observed for NBT-5%KBT, which were taken along the [001] orientation. Parts (a) through (d) show increasingly higher resolution images, revealing the presence of hierarchical domains. The images with lower magnification (see Figure 5.1a-b, taken using EM 420) show a quadrant-like (i.e., square) domain morphology, with a domain width/length on the order of about 35nm. These quadrant domains displayed {110}-type orientations and were stacked together along similar directions. This configuration imparts a 4-fold texture symmetry to the domain morphology at length scales above 500nm; at finer length scales, however, this pattern is lost. With increasing magnification (see Figure 5.1c-d, taken using JEOL), each quadrant-like domain was found to have a sub-domain structure consisting of about four to six very fine polar lamellar domains, each of which was about 8~20nm in width and stacked along the same [100] and [010] directions. Although the width of these sub-domain structures width vary according to its location, it was almost the same in a single quadrant domain. Figure 5.1e-f illustrates (using yellow visual guidelines) how the domains and sub-domains are stacked together, establishing domain hierarchy.

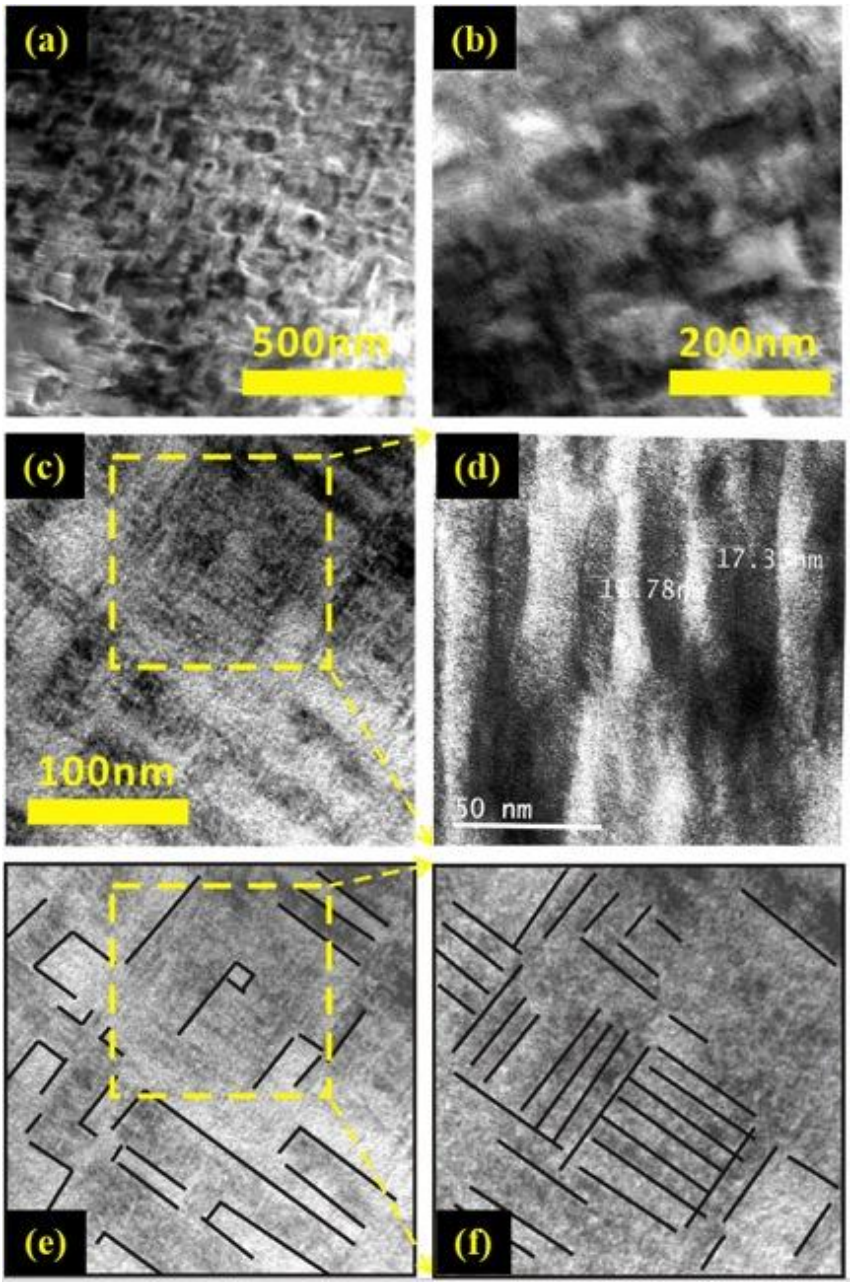

Figure 5.1: TEM images taken near the [001] direction showing the domain structures of NBT-5%KBT. (a) and (b) low magnification images from EM420 TEM; (c) high magnification images from JEOL TEM, showing the fine structure of the sub-domains; (d) partial enlarged image of (c), which illustrate the clear sub-domain boundaries; (e) outlines of domain boundaries showing the packing pattern of domains and sub-domains; (f) partial enlarged image of (e).

Figure 5.2 confirms that NBT-8%KBT shares a similar hierarchical domain structure as that found in NBT-5%KBT. Similarly, the nature of the self-assembly remains unchanged with KBT content. The width and density changes in the average quadrant domain and in the average sub-domain (lamellar) are provided in Table 5.2. Generally, the quadrant domains are relatively unchanged compared to the lamellar sub-domains. Specifically, the lamellar sub-domains in NBT-8%KBT are slightly in size, but feature much weaker domain wall contrast, which results in fewer sub-domains within a single quadrant domain. A schematic summarizing the hierarchical domain structure is shown in Figure 5.3. This schematic illustrates how multiple lamellar sub-domains having the same orientation and size stack together to form a quadrant-like domain, and how the orientation of the lamellar domains within neighboring quadrant changes. This pattern then self-assembles into macro-domain plates that fill the entire volume of the low temperature transformed phase.

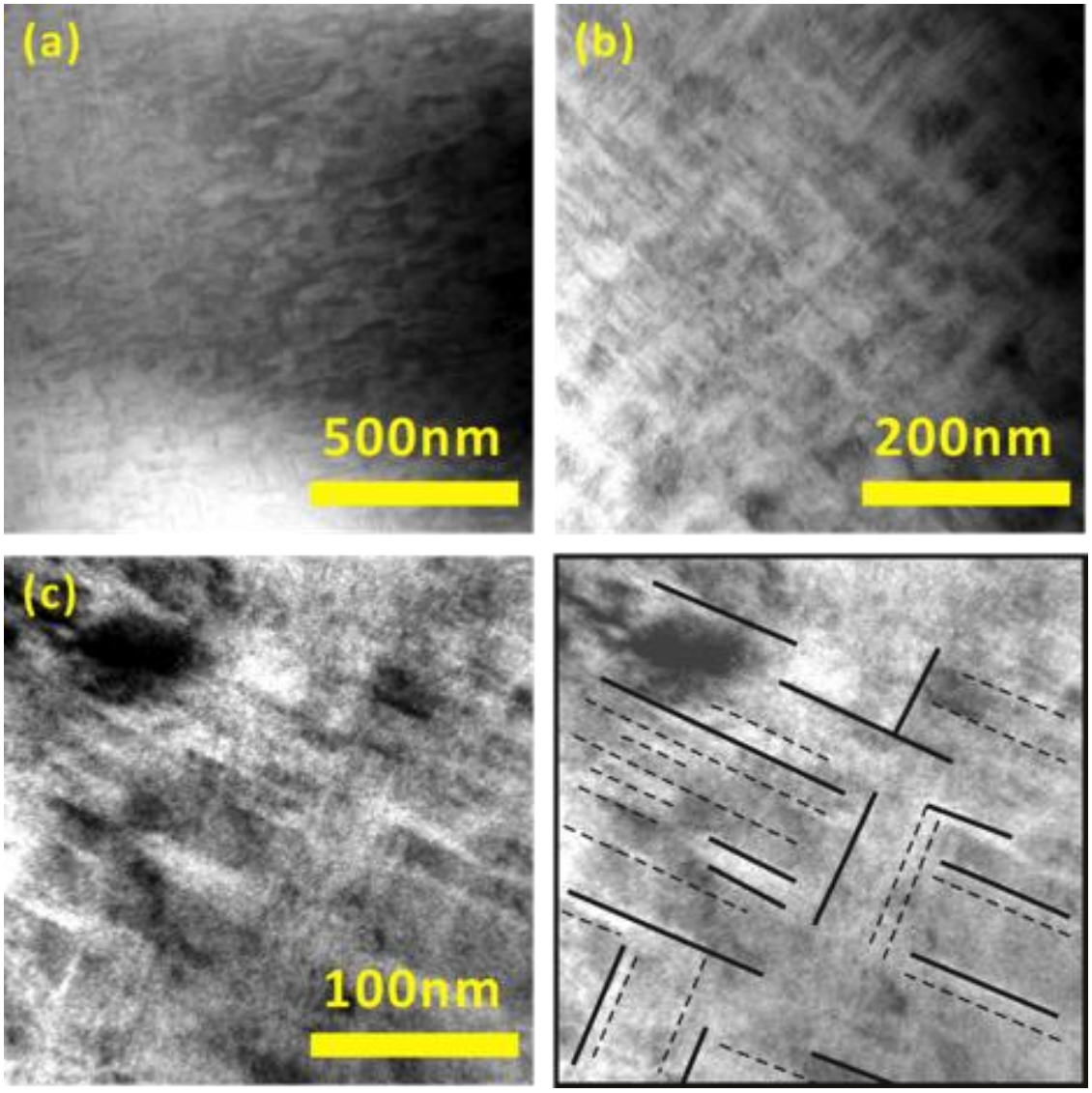

Figure 5.2: TEM images taken near [001] direction showing the domain structures of NBT-8%KBT. a) and (b) low magnification images from EM420 TEM; (c) high magnification images from JEOL TEM, showing the fine structure of the sub-domains; (d) outlines of domain boundaries showing the packing pattern of domains and sub-domains.

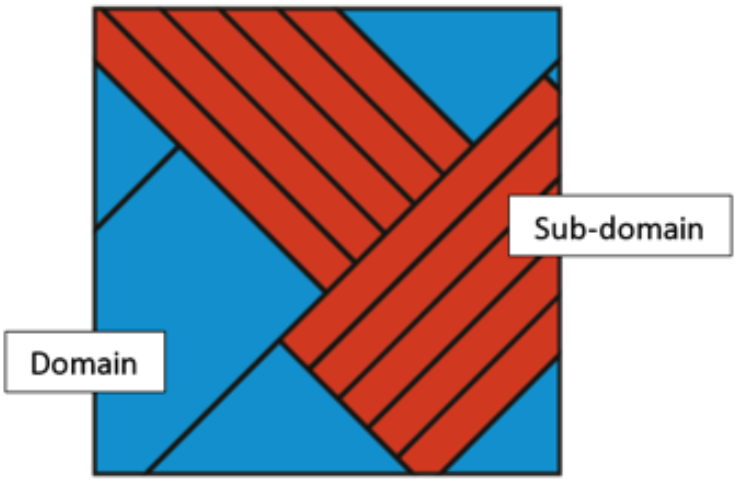

Figure 5.3: The sketch of domain packing pattern of NBT-x%KBT.

Similar square-like domains have previously been reported in NBT [43, 90, 91]. Specifically, small rhombohedral polar domains with a square-like morphology were found to nucleate on cooling within the geometrical constraints imposed by a tetragonal ferroelastic macro-domain structure inherited from high temperatures [91]. However, previous studies have not reported the presence of small lamellar sub-domains within the quadrant-like ones. This is the first report that demonstrates a high density of polar nano-twins in a NBT-type material that results in a hierarchical domain structure near the MPB.

	NBT-5%KBT	NBT-8%KBT
Quadrant domain width (nm)	36	43
average aspect ratio	2	2
density (per 100nm*100nm)	2.2	1.4
Lamellar sub-domain width (nm)	8	10
sub-domain density (per quadrant domain)	5	3
average aspect ratio	9	9

Table 5.2: Summary of hierarchical domain features.

It is relevant to note that geometrically arranged and stacked PNDs having a lamellar morphology have previously been reported within the macro-domain platelets for PMN-x%PT in the vicinity of its MPB [92]. These lamellar domains were situated along the [110] orientation and were much longer than those observed for our NBT-x%KBT compounds, but they did not assemble into a quadrant-like pattern at intermediate length scales. The domain self-assembly in PMN-x%PT is driven by geometrical invariant conditions that achieve elastic compatibility conditions [92]. Investigations of the hierarchical domains in PMN-x%PT under dc electric bias E_{DC} have shown a redistribution of the PNDs, which according to adaptive phase theory, can be used to account for its exceptionally high piezoelectric properties near its MPB.

On the other hand, similar quadrant-like morphologies have previously been reported in ferroelectric vortices [93]. Thermodynamically, true quadrant domains form with large declination stresses and are likely to be unstable for sizes above a few nanometers. However, partial stress relaxation has been reported via the formation of internal stripe-like domains [94]. Such quadrant-like morphologies are favored by large domain wall energies (γ) and low spontaneous elastic strains (ε) [95, 96]. Interestingly, even though the domain wall energy of MPB solid solutions is low [32], domains in the NBT-derived systems do not self-assemble into an elastically relaxed condition—instead preferring the quadrant-like structure over the adaptive state. This behavior presents a paradox for understanding the origins of the quadrant-like morphology in NBT-x%KBT. Other factors could complicate this self-assembly, such as, but not limited to, multiple competing order parameters – i.e., frustration.

Figure 5.4 illustrates SAED patterns for both NBT-5%KBT (Parts (a) and (b)) and NBT-8%KBT (Parts (c) and (d)). These patterns were obtained utilizing the EM420 TEM, focusing

on [11-2] (Parts (a) and (c)) and [001] (Parts (b) and (d)) zone axes. The SAED patterns from the two compositions were not noticeably different. As shown in this figure, the ½(ooe) and ½(ooo) superlattice reflections are identified in the patterns as open circles and squares, respectively. For both NBT-5%KBT and NBT-8%KBT, the most intense superlattice reflection was the ½(ooo) corresponding to anti-phase tilting, which is similar to prior reports for NBT-x%BT [45]. These results confirm that the dominant phase on a local scale for both compositions features the R structure, consistent with the left side of the MPB in the phase diagram of NBT-x%KBT (Figure 1.16b); however, there was clear evidence of the coexistence of the T-structure on a local scale. These findings are consistent with the SAED investigations shown in Figure 1.16d.

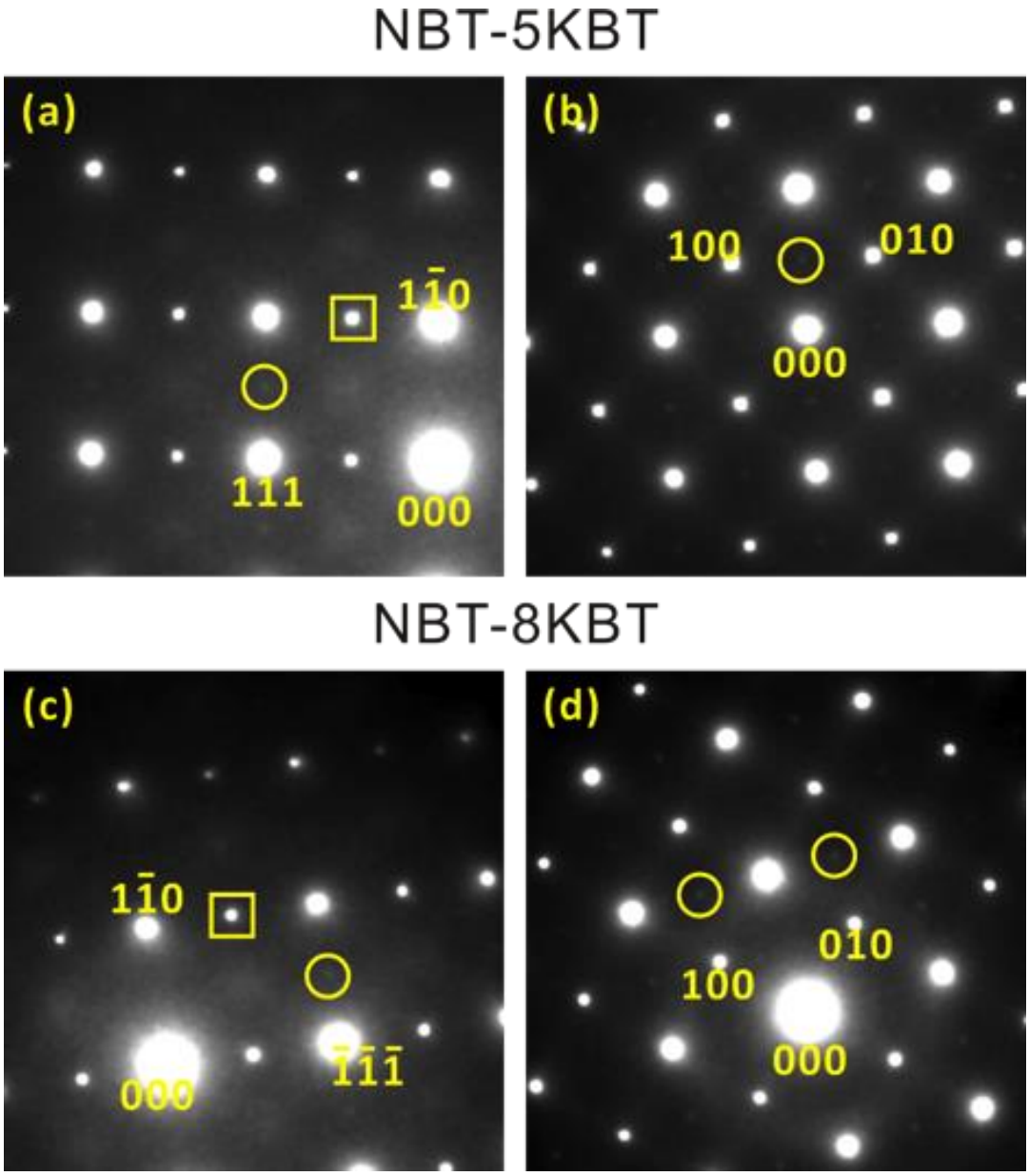

Figure 5.4: SAED patterns of NBT-5%KBT (top row) and NBT-8%KBT (bottom row) taken along: (a) and (c) [11-2], and (b) and (d) [001] zone axis, respectively. The ½(ooe) and ½(ooo) superlattice reflections are identified in the patterns as open circles and squares, respectively.

Recent x-ray diffraction (XRD) diffuse scattering analysis has also proven phase coexistence in NBT-x%BT solutions. On the R-phase side of the MPB, PNDs stacked along (001) and related L-shape diffuse scattering has been reported [97]. Close to the MPB, where the stability of the T-phase increased, oval-shaped diffuse scattering replaced the L-shaped scattering, after which PNDs correspondingly re-stacked along (110) [97]. In order to confirm whether or not similar changes in PND distribution occur for NBT-x%KBT, Figure 5.5 was developed to illustrate the different orientations of the hierarchical domain structure. The insets in the top-left of this figure are SAED patterns, where the selected reflections are marked by dashed squares. Figure 5.5a shows a dark field (DF) image taken along the [001] zone axis with filters purposefully selected to allow (110) contributions only. Large quadrant-like domain contours were found in the DF image, but had weak contrast; dashed lines are used in the figure to help better illustrate the contours. Figure 5.5b shows the corresponding bright field image taken from the same zone axis and same sample area. Here, the quadrant-like domain contours are no longer visible; instead, lamellar sub-domain structures appear. Clearly, the quadrant-like domains are oriented along the (110) axis; in contrast, the lamellar sub-domains are oriented along the (001) axis. Thus, it can be confirmed that the quadrant-like domains reported herein have elastic invariant conditions inherited from the T-phase, whereas the lamellar sub-domains represent those of the average structure of the polar R-phase. In considering in aggregate the domain morphology changes described above, the results confirm that the PNDs of NBT-x%KBT change as the composition approaches the MPB, supporting the adaptive theory previously applied in NBT-x%BT.

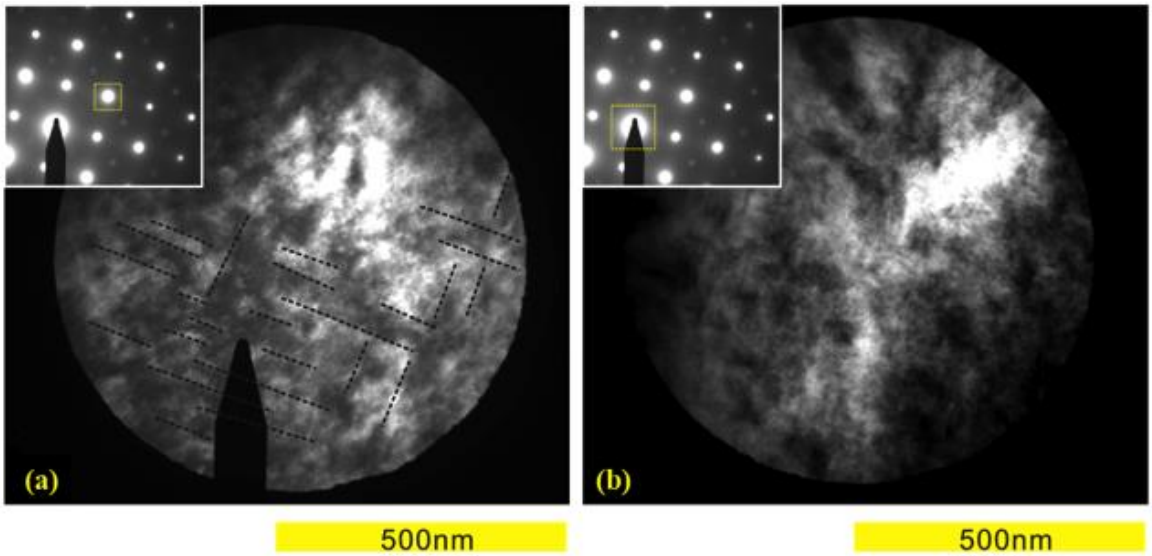

Figure 5.5: (a) Dark field images from (110) of NBT-8%KBT, taken along (001) zone axis SAED (see insert). Domain contours along the [100] direction are identified by dashed lines, which consisted of PNDs and (b) bright field images of NBT-8%KBT, taken from the same selected area and SAED pattern (see insert). No obvious domain contours can be identified, but the PNDs remain visible.

A number of versions of phase diagrams for NBT-x%KBT solid solutions have been reported [26]. However, most authors agree that the MPB region between the R phase of NBT and T phase of KBT is near $0.15<x<0.20$ (see Figure 1.16b). The difference in the location of the MPB, as well as disparities in the phase diagrams, are attributed to variations in single crystal growth methods. Recall that for this investigation we prepared our crystals utilizing the top seeded-solution method. The structural and electrical properties of similar TSSG-generated crystals have previously been published [27]. It is relevant to note the significant P_r decrease observed from changing composition from the R side to the T side of the phase diagram has previously been reported for NBT-x%BT [82], suggesting similar structure-property relationships. We believe that variations in the MPB location can be understood by examining the changes in the hierarchical domain distributions, which appear

to have coexisting T and R geometrical invariant conditions over a wide length scale, in addition to featuring coexisting R (½(ooo)) and T (½(ooe)) tilt domains of about several nm in size.

Considering the similarities between structure and resulting properties, R-T phase diagrams, and mixed A-site cation natures, a generic description of PNDs can be used to describe both NBT-x%BT and NBT-x%KBT. In the vicinity of the MPB, the polar lamellar orientation (and twin stacking) changes from the R phase (001) direction to the T phase (110) direction; correspondingly, contrast features of the R phase lamellar sub-domains are weakened. Nonetheless, the resulting changes in quadrant domains are not that obvious. These observations support the conclusion that the polar hierarchical, or quadrant-like, domain structure is not sensitive to domain distribution changes that achieve a lower elastic free energy, as characterized by compatibility conditions. We believe that this finding is due to the presence of competing domain structures with different order parameters. The interlocking of the tilted oxygen octahedra, which occurs internally within the polar lamellar domains, makes it difficult to achieve a fully relaxed elastic state. In this regard, the Pb-free NBT-type systems are notably different than the Pb-based ones typified by PMN-x%PT. Furthermore, the interlocking tilted octahedra make it difficult for the small polar lamellar domains to be redistributed under an applied E-field in NBT-type systems. Accordingly, the domain contribution to a given system's piezoelectric properties is likely to have resulted from a polarization extensional mode [98], rather than from a rotational one associated with either the adaptive [92] or homogenous M phases [80]. The residual elastic energy locked within the domain structure of NBT-type systems, typified by a quadrant-like morphology, may significantly reduce piezoelectric properties. Accordingly, to enhance the

piezoelectricity of Pb-free systems, future efforts should be directed at de-slaving the polar order parameter from the octahedral rotation order parameter for compositions near the MPB.

In summary, the ferroelectric domain and local structures of NBT-x%KBT single crystals were investigated by various TEM methods, with findings confirming the presence of a unique hierarchical domain structure. Small polar lamellar sub-domains exist that are oriented/stacked along (001), and which correspond to the R (R3c) phase. These fine lamellar sub-domains then self-assemble into a quadrant-like morphology oriented along the (110) that correspond to the T (P4bm) phase. Furthermore, these fine lamellar (polar) domains contain many nm-sized oxygen tilt (nonpolar) domains, where both in-phase (P4bm) and anti-phase (R3c) tilt regions coexist, as confirmed by SAED-generated patterns. The main change in the domain hierarchy with variations in KBT content is that size of the subdomains slightly increases with increasing x, which results in fewer subdomains per quadrant. A comparison of dark field and bright field images confirms that these domain changes correspond to a gradual PND evolution from average R3c to P4bm phases.

Similar to NBT-x%BT, the NBT-x%KBT system has a polar order parameter with a coherence length on the orders of 10-100nm, as well as both R- and M-type nonpolar rotational order parameters with a coherence length of a few nanometers. These ferroelectric polarization and oxygen rotational order parameters are known to be coupled through rotostriction [99]. Thus, domain frustration over multi-scales plays an important role in the hierarchical arrangement, resulting in similar quadrant-like domains. In turn, following adaptive phase theory [32], this behavior may restrict the piezoelectricity in NBT-type systems due to the increased difficulty of redistributing the domain distribution under an electric field.

6. Phase coexistence near the MPB in ternary Pb-based single crystals, and effect of polar nanodomain distribution.

The recently reported ternary modified system, $Pb(In_{1/2}Nb_{1/2})O_3$-$Pb(Mg_{1/3}Nb_{2/3})O_3$-$PbTiO_3$ (PIN-PMN-PT), represents an outstanding competitor amongst members of this family of newly emerging relaxor-PT piezo crystals [100, 101]. This novel ternary solid solution is capable of operating at higher temperatures, while maintaining its superior piezoelectric performance [100-104]. The various property improvements afforded by these ternary PIN-PMN-PT crystals have already attracted significant attention due to their typically high piezoelectric and electromechanical coefficients [103-107]. With regards to applications, investigators have started to simulate specific device performance outcomes of PIN-PMN-PT-based systems as a replacement for PMN-PT and PZN-PT [108-110]. However, as a newer member of the relaxor-PT family, PIN-PMN-PT is still in considerable need of more fundamental research focused on its complicated structure and phase transformational sequence [111]—and particularly how substituents affect the phase transformational sequence and structure-property relations via changes in PNR distribution.

This section describes efforts to establish patterns of electric field-induced phase transitions near the MPB, and then determining the system's phase stability under an applied electric field. Using X-ray diffraction, a phase transformational sequence of cubic (C) → tetragonal (T) → monoclinic-C (M_C) was identified, along with phase coexistence regions in the field-cooled (FC) condition. A detailed electric field-temperature (E-Temp.) phase diagram was developed to illustrate not only regions of the T+M_C and C+T phase coexistence, but also their extensions over a significant temperature range. Furthermore, a broadening of phase coexistence regions in E-Temp. space with an increase in the magnitude of E provides

indirect evidence of the presence of polar nanodomains (PNRs) within the C, T, and M_C phases.

The electric field-temperature measurements (E-Temp. diagram) of the phase stability of PIN-PMN-PT crystals obtained in this investigation are summarized in Figure 6.1. The left panel of Figure 6.1 shows the field-cooled E-Temp. diagram. The right panel summarizes the XRD data provided in the left panel for the (002) peaks at different temperatures and E. Due to experimental restrictions, investigations were not performed below room temperature. At room temperature, tetragonal peaks in the (002) scan persisted, which confirms that the $(M_C+T)\rightarrow M_C$ boundary is located below 25℃. In order to determine the approximate location of the $(M_C+T)\rightarrow M_C$ boundary, (200) line scans were also measured. However, due to dielectric breakdown, we were limited in measuring these (200) scans for E>2kV/cm applied to the 3×0.5 mm^2 side of the sample. Consequently, two data points were utilized as an experimental means to approximate the $(M_C+T)\rightarrow M_C$ boundary, where the dashed line is simply an extrapolation to higher fields. More detailed data will be provided in the following section.

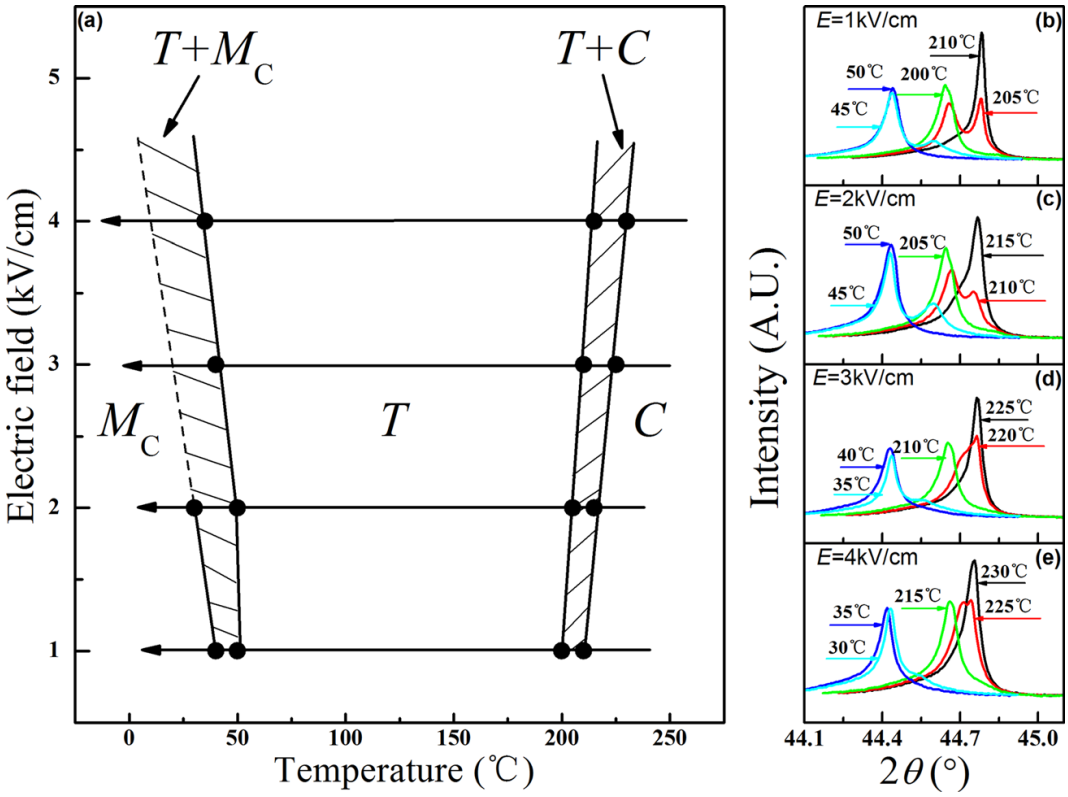

Figure 6.1: Left panel (a) shows an E-Temperature diagram obtained from the FC structural measurements. The solid dots were determined on the basis of the XRD scanning, and the horizontal arrows are used to indicate the direction along which the temperature was changed. Round dots are from XRD result on the left panel, and the square dots are from XRD results on (200) and (220). The right panel shows XRD line scans along the (002) under four different electric fields: (b) 1 kV/cm; (c) 2 kV/cm; (d) 3 kV/cm; (e) 4 kV/cm.

By comparing this E-Temp. diagram for the ternary PIN-PMN-PT to other binary relaxor-PT crystals, one can see that the ternary system studied in this investigation demonstrated a similar phase transformational sequence to those previously reported for PMN-35%PT [36] and PZN-8%PT [112]. With decreasing temperature, the lattice symmetry changed from cubic to tetragonal, and subsequently from tetragonal to monoclinic-C. A line

broadening was also observed in the T phase of PIN-PMN-PT with increasing E//[001], similar to that previously reported for binary PMN-33%PT and PZN-8%PT crystals. With increasing E—in addition to $T_{C\rightarrow T}$ (i.e. C→T phase transition temperature) increasing and $T_{T\rightarrow Mc}$ (i.e. T→M_C phase transition temperature) decreasing—regions of phase coexistence were found over a notable temperature range, whose range was broadening with increasing E. For example, under E=1kV/cm, the C→T transition began at 210℃ and was completed at 200℃. The width of the C and T phase coexistence region was ΔT=10℃. In contrast, when E was increased to 3kV/cm, ΔTemp. was widened to ΔT=15℃.

The shift of the C→T boundary to higher temperatures, and that of the T→M_C one to lower ones, can be explained by thermodynamics. Specifically, an electric field applied along (001) will reduce the free energy of the T phase (P4mm, $a_0^0a_0^0c_+^0$), stabilizing it over a wider temperature range [36]. The paraelectric → ferroelectric transition temperature T_C, [111] for example, at various E can determined as

$$Tc(\mathrm{E}) = \mathrm{Tc} + \frac{4}{\alpha(\mathrm{x})}\sqrt{\frac{-\gamma(\mathrm{x})}{3\beta(\mathrm{x})}} \qquad (1)$$

where α(x), β(x), γ(x) are the coefficients of the various ordered terms in the free energy expansion of Landau theory. In short, increasing the electric field along (001) broadens the T phase region, raises $\mathrm{Temp.}_{C\text{-}T}$, and decreases $\mathrm{Temp.}_{T\text{-}Mc}$.

To explain the presence of a region of phase coexistence over ΔT, as well as how it is broadened by E, further study is needed that also considers the role of polar nanoregions (PNRs). Generally, single crystals inevitably have defects, residual internal strain, and other types of imperfections. Specifically, relaxor-PT type single crystals have a B-site cation disorder, which results in random fields [113]. This feature is believed to be the origin of PNRs in relaxor-PT crystals. Now, consider the possible influence of PNRs on the C→T

phase boundary, as schematically illustrated in Figure 6.2. For $T_C<T<T_D$, where T_D is the Burns temperature [112] and T_C the Curie temperature, Figure 6.2a shows the presence of a few small PNRs (No.1 to 4) that do not significantly strain the lattice. This region is typically a non-polar C phase. Figure 6.2b illustrates how PNRs respond to the application of E//[001] (note numbers 1-4). The PNR (marked as 1), whose polarization is parallel to E, is favored by E, while its polarization this is anti-parallel to E (marked as 2) is suppressed [112]. The PNR whose polarization orientation is different, but close to, the direction of E (marked as 3) is rotated towards E, while its polarization at 90° to E (marked as 4) is nearly unchanged [112]. Generally, E//[001] lowers the lattice nonuniformity along [001] and results in a non-zero sum of the PNR polarizations along that direction.

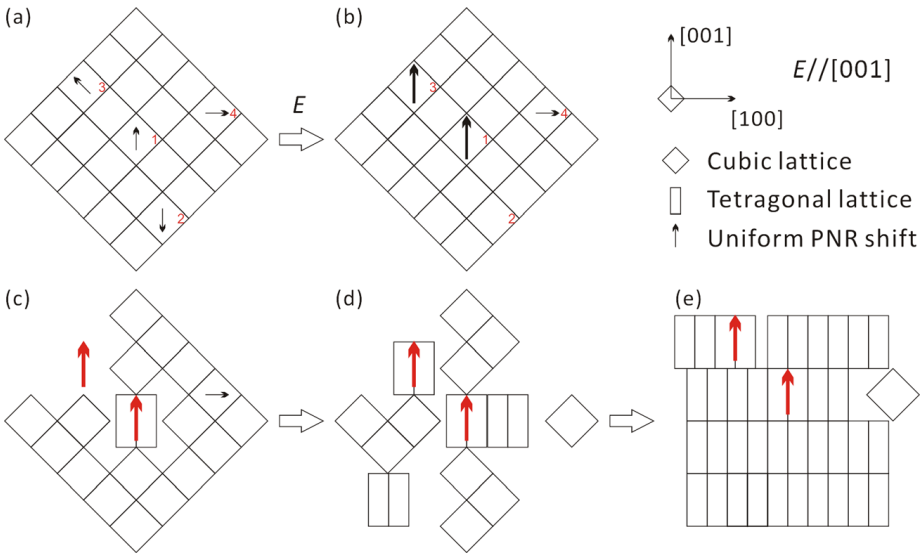

Figure 6.2: Sketch of PNR model: (a) zero field condition for $T_c<T<T_D$. The PNRs are embedded in a cubic matrix. PNRs are marked by Nos.1–4 to represent the different orientations comparing to the applied electric field. (b) E//[001] is applied. (c)–(e) The FC process within the C!T phase transition region.

Figure 6.2c-e illustrates how the C phase transforms to the T phase during an FC process (note that single phase C and T regions are not shown in these illustrations). As the temperature is decreased towards $Temp._C$, the PNRs begin to strain and distort the lattice in its vicinity, and the C→T transition tends towards its onset. The growth of the T phase begins near these distortions of the lattice around the PNRs (see Figure 6.2c), and eventually dominates the entire volume of the sample (see Figure 6.2e) when the transition is complete. As shown in Figure 6.2c-e under a constant E, the volume fractions of the T and C phases continuously change with temperature, where the lattice mismatch and internal strain first increase and then subsequently decrease with decreasing temperature. The continuous changes in intensity and FWHM of the diffraction peaks between those of the T and C phases confirm analogous changes in phase volume fractions and lattice mismatches, as shown above in the right panel of Figure 6.1.

Following the concept of the model in Figure 6.2, increased E//[001] will result in larger PNR polarizations along the same direction, while at the same time inducing neighboring lattice regions to begin their C→T transition at ever increasing temperatures above Temp.c. Accordingly, this internal strain between PNRs and neighboring matrices helps explain the broadening of the phase coexistence region with increasing E.

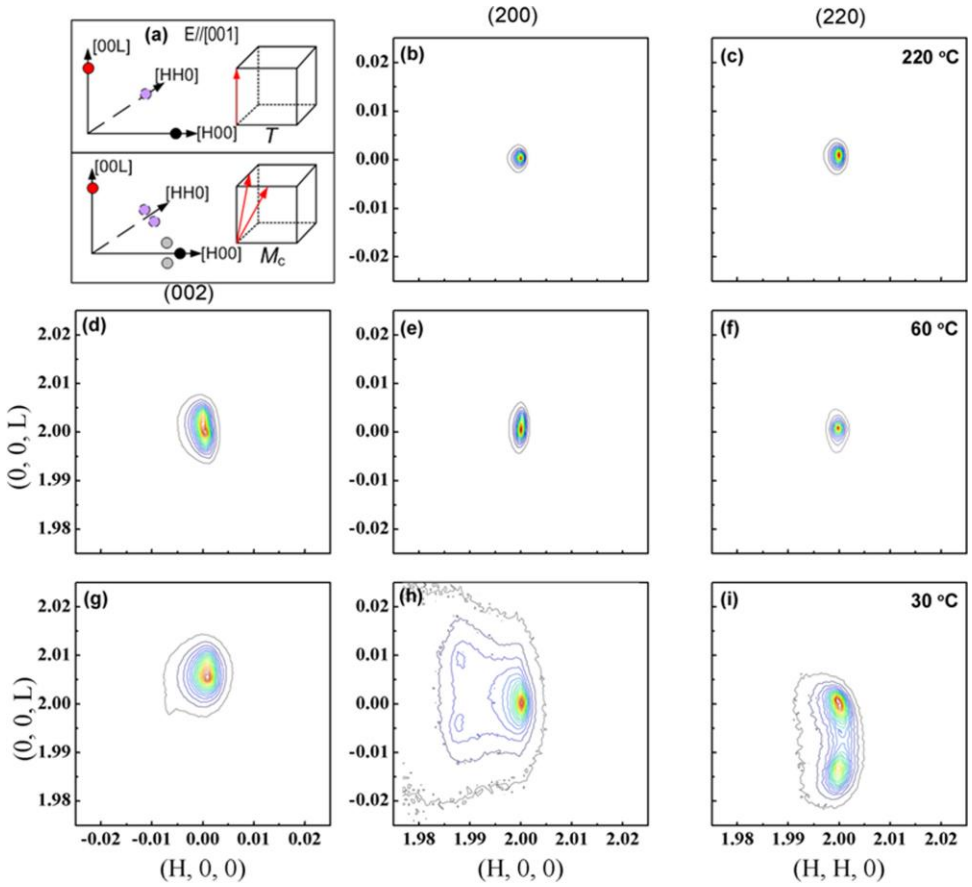

Figure 6.3: XRD mesh scans along the (002)/(200)/(220) in the FC condition (E=1 kV/cm//[001]). (a) sketch of difference between T phase and MC phase along (200)/(220). (b) and (c) C phase at 220℃. (d)–(f) T phase at 60℃. (g)–(i) MC phase at 30℃. The intensity in (h) is in log scale because the peaks of the a-domain were weak. The other mesh scans are in linear scale.

Although the right panel of Figure 6.1 provides sufficient XRD data evidencing how the C→T boundary depends on E, more data is needed in order to understand how the T→M_C boundary shifts with E. And indeed, this information is provided by the XRD data taken about (200) and (220), as shown in Figure 6.3 and Figure 6.4. Specifically, Figure 6.3

contains mesh scans to help with phase identification, and Figure 6.4 provides line scans obtained at various zones at different temperatures for E= 1kV/cm//[001]. Figure 6.3a shows a schematic of the characteristic splitting in the mesh scans for both the T and M_C phases. The patterns along (00H)/(H00)/(HH0) in the T phase are all single peaks, whereas those along (H00)/(HH0) in the M_C phase consist of multiple peaks. Under E//[001], the (00H) zone of M_C is fixed by E and only features a single peak; in contrast, along (H00) a triplet splitting is found that consists of two (200) peaks representing two a-domains, and one single (020) peak representing one b-domain. In addition, the patterns shown along the (HH0) zone are indicative of the distinct T and M phases. Following the splitting shown in the schematic of Figure 6.3a, data in Figure 6.3b-c reveal the presence of the C phase at 220℃; Figure 6.3d-f shows the T phase at 60℃; and Figure 6.3g-i demonstrates the M_C phase at 30℃. Thus, the FC phase transformational sequence is $C \rightarrow T \rightarrow M_C$. In order to determine transition temperatures more accurately—and in particular for $T \rightarrow M_C$—Figure 6.4 shows (200)/(220) line scans compared to that of (002). Figure 6.4a reveals the presence of a C phase at 210℃, while Figure 6.4b shows the T phase at 200℃. Note that the peaks of the (200)/(200) line scans shifted differently with temperature: the lattice parameter c_T increased and a_T decreased when cooling in the T phase. The T phase remained stable at 50℃, as shown in Figure 6.4c; in contrast, at 45℃ the M_C phase became apparent (see Figure 6.4d). Finally, Figure 6.4e, which was taken at 40℃, illustrates the coexistence of the T and M_C phases for the (002) and (200)/(220) scans. Along the (002), the T-phase (002) peak can be seen to coexist with the M_C phase (002) one, whereas no such T peak was found along (200)/(200). This phenomenon can be explained by the fact that E applied along (002) fixes that axis; conversely, for (200)/(220) the polydomain T state is stable. Our data clearly evidence the coexistence of T and M_C phases under E=1kV/cm for temperatures between 45℃ and 25℃. To achieve a single phase M_C state, the sample needs to be cooled below room temperature.

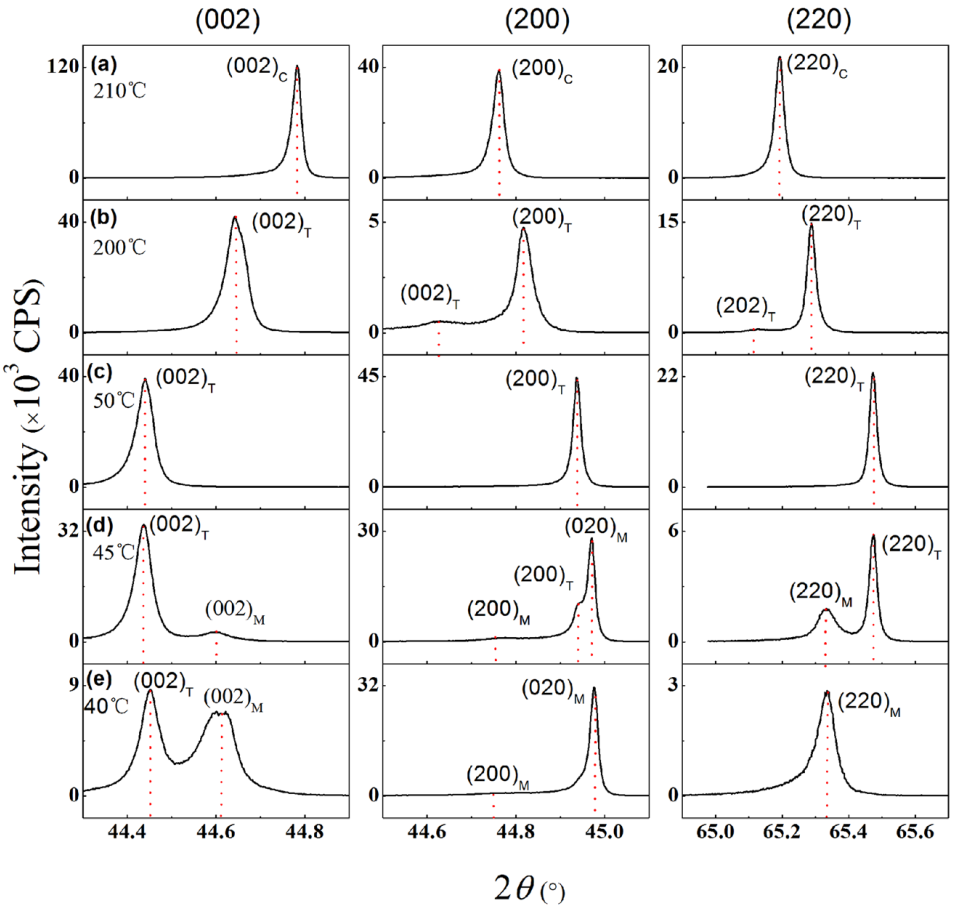

Figure 6.4: XRD profiles in the FC condition. (a) C phase at 210 ℃. (b) and (c) T phase between 200 ℃ and 50 ℃. (d) MC phase appears at 45 ℃. (e) T phase still exists in (002) but disappears in (200)/(220).

Figure 6.5 illustrates the temperature-dependent lattice parameters calculated from the data presented in Figure 6.4. The value of a_T was determined from the $(200)_T$ peaks in Figure 6.4 and c_T from the $(002)_T$, whereas the $(202)/(200)_T$ peaks were used to confirm the consistency of the calculated values for a_T and c_T. The value of b_M was calculated from the $(020)_M$ and b angular splitting in the (200) mesh scans. With known values of b_M and b, the values of a_M and c_M can then be calculated by combining with the $(200)_M$ and $(002)_M$ peak

positions. In addition, the $(220)_M$ and (220) mesh scans were again utilized to confirm the consistency of the lattice parameter values.

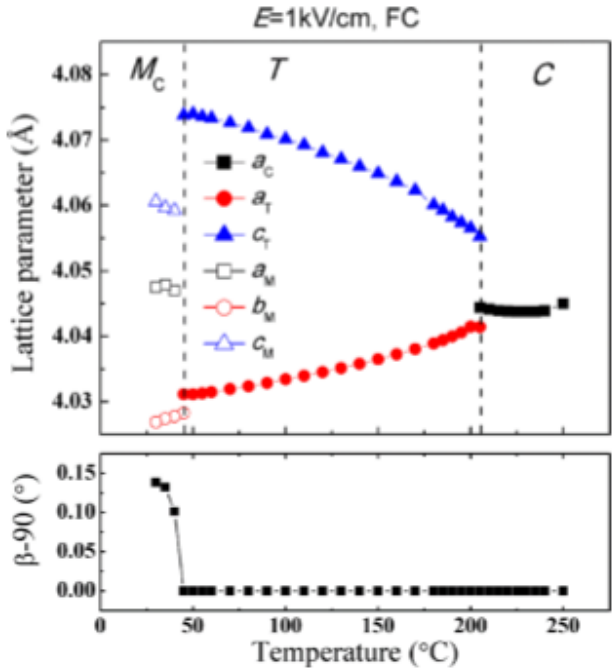

Figure 6.5: Temperature dependence of the lattice parameters (top panel) and -90o (bottom panel) observed in the FC condition. Solid lines drawn through the data points represent visual guides.

In summary, a phase transition sequence of C→T→M_C was found for PIN-PMN-PT crystals in the FC condition. A detailed E-Temp diagram was constructed to summarize the findings, which illustrates how the phase boundaries shifted and new regions of phase coexistence between the C, T and M_C phases occur in the ternary systems. The regions of C-T and M_C-T phase coexistence were found to be broadened in temperature space with increasing E, which provides indirect evidence of the importance polar nanoregions within the average symmetry of these phases over the entire transformational sequence.

The concept that provided the impetus for developing the PNR model shown in Figure 6.2 is based on conventional thermodynamic theory. Here, the PNR ensembling structure is also a form of the adaptive phase within the lattice.The study of PMN-PIN-PT near the MPB is advocated due to three principal reasons:

- The electric field-induced phase transition is much easier to achieve in PMN-PIN-PT.
- The heterogeneous structure is common in both lead-based and lead-free materials, making it easier to develop a universal model describing these heterogeneous states.
- PMN-PIN-PT was developed in order to achieve higher T_C in perovskite ferroelectric relaxors.

These types of requirements are also common in the NBT-derived system.

7. Superlattice point-linking diffuse scattering network and its dynamical mechanism in lead-free NBT-xBT single crystals

7.1. Background

It has been nearly 50 years since the first atomic-level ferroelectric microscopic theory was published by Cochran and Anderson [114], which was based on their study of lattice dynamics. The concept of soft modes was introduced to describe the slowing of vibrational frequency, all the way to freezing, for transverse optical phonon modes (TO) during ferroelectric transformations. This softening of the TO mode results in the displacements of the ions becoming static on cooling, thereby producing large permanent spontaneous polarizations and crystal lattice distortions. The concept of the soft mode underscores important characteristics of all ferroelectric transformations—namely, that most types of such polar transformations, including anti-ferroelectric ones, are special conditions of structural phase transformations. The soft mode concept is strongly supported by experimental results obtained by neutron scattering and Raman scattering, mostly in conventional ferroelectric systems such as $PbTiO_3$ [115, 116]. Neutron and x-ray diffuse scattering on and inelastic neutron scattering are powerful experimental techniques for investigating the specific microstructure and mechanisms underpinning piezoelectric behavior through phonon analysis.

Based on the unique characteristics of “relaxor” ferroelectrics—and in particular the ultrahigh piezoelectric properties of $Pb(Mg_{1/3}Nb_{2/3})O3$-$PbTiO_3$ (PMN-PT) and $Pb(Zn_{1/3}Nb_{2/3})O_3$-$PbTiO_3$ (PZN-PT)—significant efforts have been directed at modifying the soft mode theory in order to account for their unusual slow dynamical transition and relaxation mechanism [41, 57, 117, 118]. Furthermore, relaxor solid solutions have been developed in Pb-free perovskite solid solutions, which contain many of the properties of Pb-

based systems [16]. (These Pb-free piezoelectrics are described in detail in Chapter I.1.5.) Following the success of adding $PbTiO_3$ (PT) to PMN to produce a solid solution of PMN-PT, NBT was also found to form an analogous solid solution between relaxor and normal ferroelectrics, where an MPB between rhombohedral (R) and tetragonal (T) phases resides in the solid solution [16]. Consequently, $(Bi_{1/2}Na_{1/2})TiO_3$–xat%$BaTiO_3$ (NBT-xBT) and $(Bi_{1/2}Na_{1/2})TiO_3$–xat%$(Bi_{1/2}K_{1/2})TiO_3$ (NBT-xKBT) ceramics and single crystals have been developed [5]. The ternary system, NBT-BT-KBT, has also been investigated in an attempt to bring together unique aspects of NBT- and KBT-based solutions into a common ternary solution [5].

On the tetragonal side of the MPB, NBT-xBT belongs to the space group P4bm (Figure 7.1a), which differs from the P4mm space group symmetry of tetragonal Pb-based relaxors, such as PMN-PT [119]. Along with the R3c space group on the rhombohedral side of the MPB, our results show that NBT-xBT features two types of oxygen octahedral tilt systems, which can be identified by characteristic superlattice structures (P4bm/R3c), as shown in Figure 7.1a. In crystallographic notation, these oxygen octahedral tilt systems are designated as in-phase a0a0c+ and anti-phase a-a-a- [44]. In diffraction experiments, these tilt systems result in different superlattice reflections in reciprocal space. The in-phase M-point and anti-phase R-point can be represented by their general crystallographic indices of ½(ooe) and ½(ooo), respectively. The reciprocal space locations of both the M- and R-point are shown in Figure 7.1b in the case of a cubic lattice [120]. These rotational modes are the result of acoustical phonon modes that condense at the Brillouin zone boundaries. Although they are typically non-polar modes, they have been reported to be coupled with polarization through rotostriction [121].

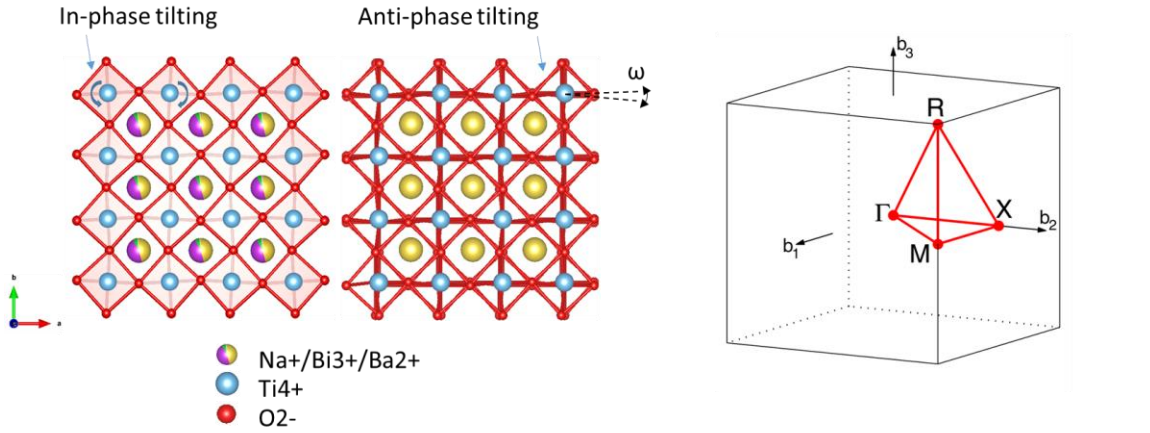

(a) P4bm for NBT-7BT and R3c for NBT

(b) Critical points in reciprocal space

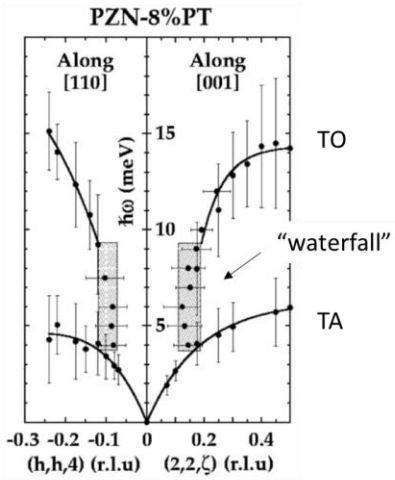

(c) Neutron inelastic diffuse scattering study of PZN-PT

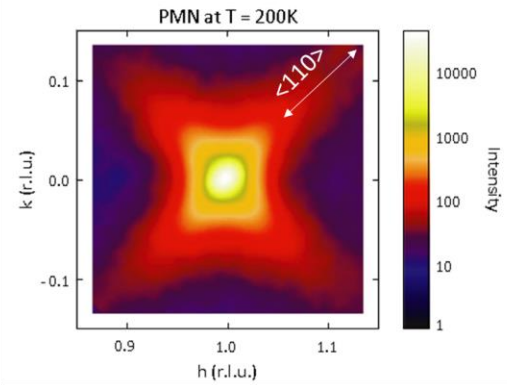

(d) Neutron elastic diffuse scattering study of PMN

Figure 7.1: Background figures: (a) NBT-BT superlattice structure; (b) critical points notation in reciprocal space for pseudocubic NBT-BT. Reprint with permission from [120]. Copyright © 2010, Elsevier B.V.; (c) neutron inelastic diffuse scattering of PZN-PT that demonstrates a "waterfall" effect between transverse optic (TO) and transverse acoustic (TA) modes. Reprint with permission from [122]. Copyright © 2000, American Physical Society; (d) neutron elastic diffuse scattering of PMN that demonstrate ridges along <110>. Reprint with permission from [41]. Copyright © 2004, American Physical Society.

Analyzing the static displacements of these oxygen octahedral tilt systems is usually achieved via XRD [82, 98] and electron diffraction [43, 123], which enable one to track the phase transition and domain structures. Electron diffraction studies [43] of NBT-xBT have shown that M-point and R-point superlattice reflections coexist with each other—where the R-point is increasingly favored with decreasing xat% on the left side of the MPB, and where the M-point is increasingly favored with increasing xat%. Inverse FFT imaging of the superlattice points has revealed multiple nm-sized tilt regions coexisting within PNRs [31]. A more detailed comparison of PMN-xPT and NBT-xBT has already been provided in Chapters I.1.3 and I.1.5. One of the main differences between these two solid solutions is that NBT-xBT requires further investigation to understand the interaction between the two different oxygen tilt systems, as well as their interaction with the polar nanodomain distribution.

Gehring et al. [122] make important strides in understanding the phonon dynamics of PZN-8PT relaxors by using neutron inelastic diffuse scattering, as shown in Figure 7.1c. Specifically, he observed that the TO phonon branch dropped into the transverse acoustic (TA) phonon branch over a short range of reduced wavevectors q. This so-called "waterfall" effect helps to link together the microscopic structure of polar nanoregions (PNRs), and the intrinsic characteristic of the solid solution near the MPB. PNRs have been proven to be the origin of relaxor behavior on the basis of inelastic neutron scattering experiments utilizing multiple kinds of A(B'B")O3 (B-site) perovskite crystals [124].

Neutron diffuse scattering has been widely used to study different types of relaxors [57, 125-127]. For NBT-xBT solid solutions, different diffuse pattern shapes are understood to characterize the different phases. NBT, on the rhombohedral side of the MPB, has been reported to have "L" shape diffuse scattering patterns near $(012)_{PC}$ (PC: pseudocubic) [125];

in contrast, NBT-5/7.5BT on the tetragonal side of the MPB features patterns that are oval shaped along the <110> direction. Another study using neutron diffuse scattering by Ge et al. [57] compared A-site NBT and B-site PMN relaxors. The authors reported both similarities and differences in the geometry of the diffuse scattering patterns and the morphologies of the PNR distributions. It is important to note that this study supports the similar diffuse scattering patterns for both NBT and NBT-5.6BT. Specifically, prominent ridges in the elastic diffuse scattering intensity resulted in different types of contours. The ridges along the [100] and [010] directions cross at (HH0)/(-HH0) and generated "L" shaped patterns for NBT; conversely, the ridges along the [110] direction crossed at (H00)/(0K0) and generated the X-shaped patterns for NBT-5/7.5BT and PMN (see Figure 7.1d) [41]. These ridges disappeared gradually upon heating above the cubic-to-tetragonal phase transition temperature of T_{CT} =523°C. It was concluded that these ridges are linked to different types of PNRs, which are common to both A-site and B-site relaxors.

Another published study of inelastic neutron scattering of NBT at a variety of temperatures focused on the softening of multiple phonon modes, including longitudinal optical (LO) and TO modes at (200) reflections and TO modes at (220) reflections [128]. A different type of "waterfall" feature was observed in the LO and TO mode dispersions, which did not directly correlate to the formation of PNRs, as identified by a mismatch with the structural phase transition temperature. Intense inelastic diffuse scattering was found at the zone boundary M-point (1.5, 0.5, 0), demonstrating in-phase oxygen octahedral tilting and indicating tetragonal phase stability. Diffuse scattering from the zone corner R-point (1.5, 1.5,0.5) gradually developed upon cooling through the tetragonal (T)- rhombohedral (R), T-R, phase boundary below the temperature of the dielectric maximum T_{max}. Elucidating these kinds of changes in mode softening, superlattice points, and diffuse scattering in more detail

will be essential to understanding the dynamic mechanism of piezoelectric/relaxor behavior in the NBT-xBT system, which this chapter was designed to accomplish.

7.2. Experiment

All neutron experiments were done using the hybrid spectrometer (HYSPEC, BL-14B), which is located at the spallation neutron source (SNS) at Oak Ridge National Lab (ORNL). The background of HYSPEC was already introduced in Chapter. 2.2. During the first beam time at HYSPEC, crystals of NBBT5 and NBBT6.5 were studied in the (HK0) plane at room temperature and at 600K. During the second beam time, crystals of NBBT4/NBBT5/NBBT7.5 were measured in the (HHL) plane at 300K/540K/700K. (See Chapter 2 for additional details on experimental settings.)

High-quality single-crystals of NBT-x%BT (x=0, 4, 5, 6.5,7%) were grown in Prof. Haosu Luo's group (Shanghai Institute of Ceramics, Chinese Academy of Science). The compositions of the solid solutions in the as-grown condition were determined by inductively coupled plasma atomic emission spectrometry (ICPAES).

During the neutron scattering experiments, two different S(Q,E) datasets were separately collected at two beam times. The first one focused on the (HK0) plane, and the second one focused on the (HH0) plane. Because each dataset contains both elastic and inelastic information at the same time, the results described herein will first be sequentially arranged by the two beam times, and then subsequently by showing elastic and inelastic results for each beam times.

The elastic results, such as shown in Figure 7.1d, are similar to those in 2D-XRD scans and SAED images. All results consist of slices integrated into energy from -1meV to 1meV.

The analysis of the elastic diffuse scattering focused on the shape of the diffuse scattering and superlattice points. These data will also be compared with data from high-energy XRD, which featured a wider range of vector q coverings and a broader temperature range.

The inelastic results shown in Figure 7.1c focused on multiple phonons. For example, the acoustic modes describe the oscillation of adjacent atoms in the same direction; thus, the softening of acoustic modes cannot lead to a net spontaneous polarization. However, the freezing of acoustic modes at the Brillouin center may result in spontaneous strain, corresponding to a ferroelectric transformation. On the other hand, the freezing of acoustic modes at the Brillouin zone edges results in adjacent strain dipoles oriented in the opposite directions which could be anti-ferroelectric.

7.3. Results

The neutron elastic scattering patterns in Figure 7.2a-c focused on the (HK0) planes of NBT-5BT at 300K (a), NBT-6.5BT at 300K (b), and NBT-5BT at 600K (c), which were indexed under the pseudocubic lattice. The slices were centered on the (200)pc zone and contained multiple M-points. Due to the fact that the ½(3±10) points overlapped with an Al powder diffraction ring from the sample holder, the M-point data discussed later will only consider the ½(5±10) reflections

In general, changes in temperature and composition did not appear to significantly impact the resulting neutron elastic scattering patterns shown for these slices. Similar diffuse scattering near (200)pc and (210)pc were already observed in prior XRD [97] and neutron [125] studies. In both compositions investigated herein, the scans showed oval-shaped scattering patterns near (210)pc with a <110> orientation and half-X-shaped scattering near

(200)pc in right panels of Figure 7.2b. These diffuse scattering features are characteristic of being on the tetragonal side of the MPB [57, 125]. Generally, the diffuse scattering for NBT-5BT was more intense than analogous results for NBT-6.5BT. Note that NBT-5BT is closer to the MPB, and features enhanced piezoelectric properties.

In-phase oxygen tilting superlattice reflections or M-points were evident in all slices. These M-points were isolated with little diffuse scattering surrounding them in the (HK0) plane, which distinguishes them from the Bragg peaks. Note the presence of diffuse scattering connecting the (120) and (210) zones, which crossed the forbidden point ½(330), as shown by the dashed white line with arrows and red cross in the top-right panel of Figure 7.2b. Here the dashed white line with arrows are parallel to the actual diffuse scattering and used for marking the directions only. This type of diffuse scattering connection was not observed toward the M-point ½(510), as will be further discussed with respect to inelastic studies.

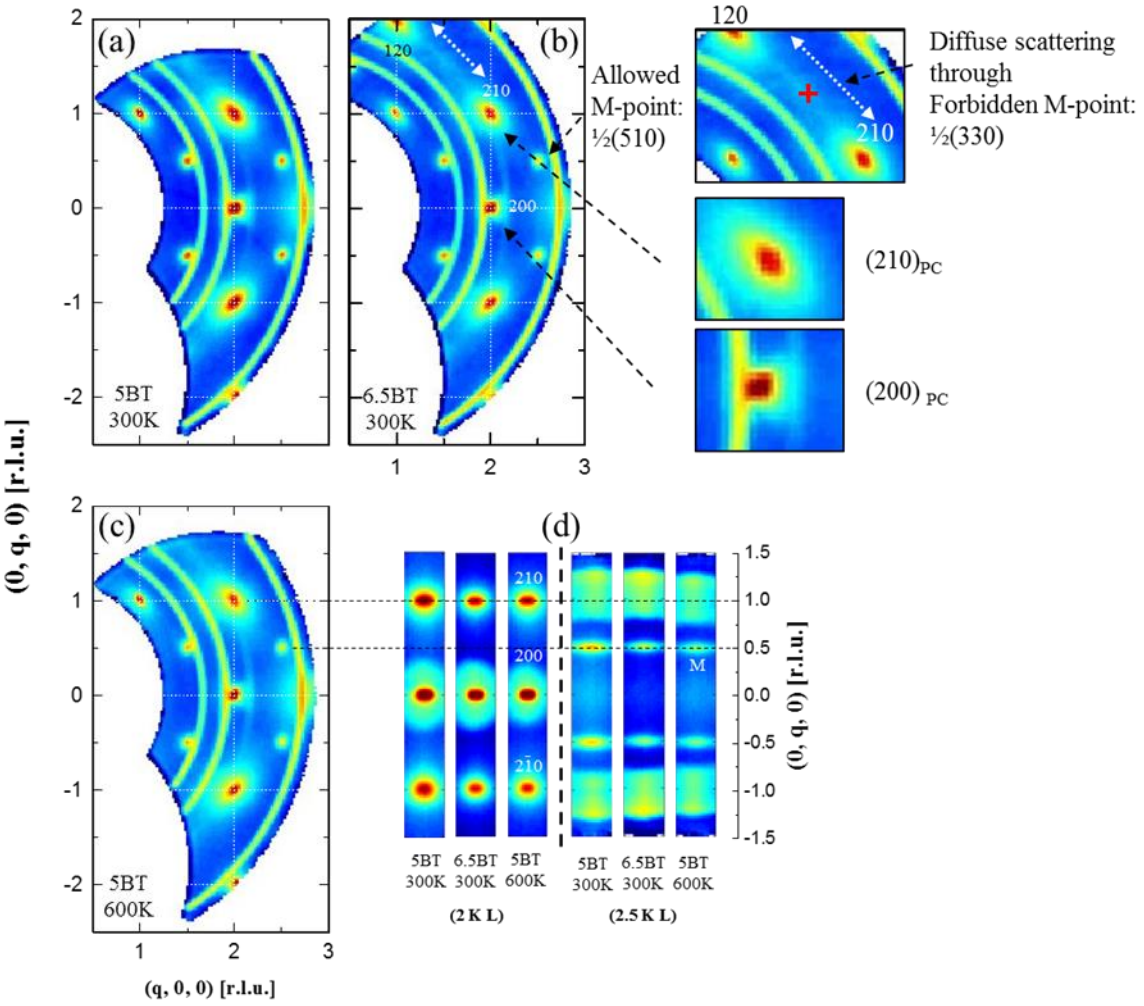

Figure 7.2: Neutron elastic scattering patterns of (a) NBT-5BT at 300K, (b) NBT-6.5BT at 300K, (c) NBT-5BT at 600K on the (HK0) plane and (d) (2KL)/(2.5KL) plane. The horizontal and vertical axes are along [0K0]/[H00] directions in the (HK0) planes and [00L]/[0K0] directions in the (2KL)/(2.5KL) planes, respectively. The intensity scales are normalized from different sample mass at (200).

We observed both symmetry-allowed (½(510), ½(310)) and symmetry-forbidden (½(330)) superlattice reflections in the tetragonal phase field of NBT-x%BT with the P4bm space group symmetry. The forbidden M-point ½(HHL)/(-HHL) is due to the unique oxygen octahedron connection (see Figure 7.1a). In the (HK0) plane and for the case of P4bm, neighboring oxygen octahedrons have opposite tilting directions, which generates from the superlattice structure a0a0c+; this finding also indicates that the oxygen octahedrons along (HH0)/(-HH0) direction share the same tilting direction. Therefore, the related superlattice points at ½(HH0)/(-HH0) are forbidden. Although this feature is not common in SAED [129, 130], it has been observed in results generated by high-energy XRD and software simulation. In continuing this discussion, I refer to two types of M-points: allowed and forbidden. Both types of M-points are shown in Figure 7.2b, while the forbidden ½(330) is marked by a red cross.

In order to further compare the elastic scattering between the Bragg peaks and the M-points, more slices (Figure 7.2d) along different directions were extracted from the same S(Q, E) dataset. The slices on the left part of Figure 7.2d illustrate the (2KL) planes covering the Bragg peak (200)/(2±10), and those on the right one show the (2.5KL) plane covering the M-point ½(5 ±1 0). Note that Figure 7.2d shares the vertical [0K0] axes with Figure 7.2c, where dashed lines were drawn to help align the same Bragg peaks and M-points within. On the horizontal [00L]pc axes of Figure 7.2d, the q range was uniform between -0.2 and 0.2. The scattering patterns in the (2KL) plane and the (2.5KL) plane were notably different from each other. The scattering near the Bragg peaks was isotropic, whereas the scattering near the M-points had a spindle-shaped feature along the [001] direction. The isotropic (200) diffuse scattering was also different from the half-X-shape ones in the (HK0) plane, whose [110] features in the diffuse scattering pattern restricted it to only the (HK0) plane.

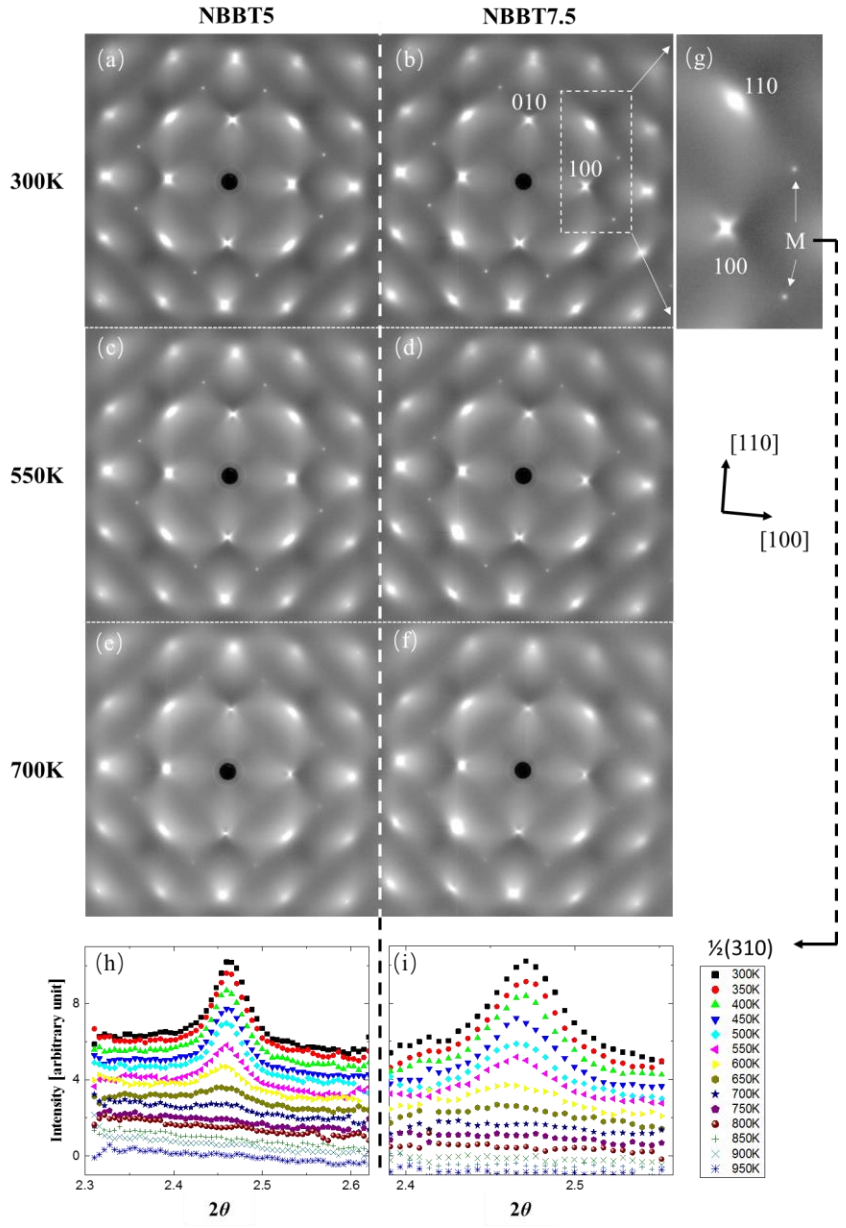

Figure 7.3: XRD elastic scattering patterns along the (HK0) planes from (a)(c)(e) NBT-5BT, and (b)(d)(f) NBT-7.5BT at (a)(b) 300K, (c)(d) 550K and (e)(f) 700K. One area in (b) is enlarged in (g) to provide higher resolution pictures of the diffuse scatterings features and M-points ½(3±10). Integration of the intensity for ½(310) peak was made over a broad temperature range, as summarized in (h) NBT-5BT and (i) NBT-7.5BT. Fixed offsets were used between two neighboring curves, in order to make comparisons easier.

Diffuse X-ray scattering investigations focusing on NBT-5BT and NBT-7.5BT at different temperatures were also performed at the Advanced Phonon Source (APS) at Argonne National Lab. Figure 7.3a-f illustrates the resulting diffuse scatterings patterns observed in the (HK0) zone. These data revealed diffuse ridges along the (110) directions, X-shaped patterns around (H00), and M-points as illustrated in the zoomed-in area in Figure 7.3g. These elastic diffuse scattering pattern results demonstrate similar features as those noted from the neutron investigations provided in Figure 7.2.

As shown in Figure 7.3, a significant (110)-oriented diffuse scattering pattern can be seen for both (x=5, 7.5) crystals. Strong X-shaped diffuse scatting features around the (q00)/(0q0) reflections in Figure 7.3 confirm that the elastic diffuse scattering features in the neutron data taken near (200) were incomplete due to the fact that they were half covered by aluminum rings. Unlike NBT [125], neither NBT-5BT nor NBT-7.5BT exhibited sharp changes in their diffuse scattering patterns with increasing temperature. Although XRD measurements were performed over a temperature range from 300K to 950K, Figure 7.3a-f only illustrates three temperatures conditions: one at room temperature, a second near the dielectric constant maximum temperature, and a third at 700K.

A detailed tracking of the temperature-dependent ½(310) intensities of the M-points is given in Figure 7.3h-i. These intensities were 2D-integrated around the ½(310) reflections along 2θ and shared the same integration area. Also provided are fixed offsets between the two neighboring curves to make comparisons easier. A common feature of the two datasets was the lack of intensity jumps with changes in temperature. This finding demonstrates that changes in the M-point oxygen octahedral rotations are gradual, and that there are no characteristic changes associated with the dielectric maximum or ferroelectric phase transformation. Comparing the data from different compositions reveals that the integrated intensities of the M-point are stronger at room temperature for NBT-7.5BT, while the peaks

for NBT-5BT were narrower in FWHM. This comparison reveals an essential feature that we observed near the MPB, which will be discussed in a subsequent section along with studies of the R-point.

Inelastic neutron scattering features near (200) are shown in Figure 7.4, which are divided into two panels. The top row presents the transverse Δ_5 phonon modes, which have already been folded along the [H00] axis to improve the statistical quality of the data; the bottom row presents the longitudinal Δ_1 phonon modes. Within these maps, the fitting results from both constant-q cuts and constant-E cuts are presented together. Specifically, the constant-q cut results are marked by white squares with vertical error bars, and results pertaining to constant-E cut findings are indicated by the black squares with horizontal error bars.

In Figure 7.4a, the NBT-5BT crystal at 300K exhibited a "waterfall" effect, where the TO phonon drops from 11meV to 7meV at q~0.17 into the TA mode. This feature has been reported to be common for both NBT [128] and PMN [131]. At temperatures in excess of 600K (see Figure 7.4b), this waterfall effect was significantly weakened, although the TO mode still softened into the TA mode at the same q. In Figure 7.4c, the TO phonon of NBT-6.5BT can be seen to have a similar "fall" at the same q~0.17; however, the degree of this fall was not as steep as that in Figure 7.4a. In PMN [131] and other relaxors, it is believed that the waterfall effect is closely related to PNRs

Note that 600K exceeds the ferroelastic transition temperature into the M-point in-phase oxygen tilted tetragonal phase region of NBT. The persistence of the waterfall effect at high temperatures indicates that the small/local oxygen tilt domains may play an important role in the lattice dynamics of the TO mode. On cooling, the effect becomes stronger as evidenced by the fact that PNRs form below T_{max}. A comparison of the data for NBT-5BT and NBT-6.5BT indicates that the waterfall effect becomes more pronounced near the MPB.

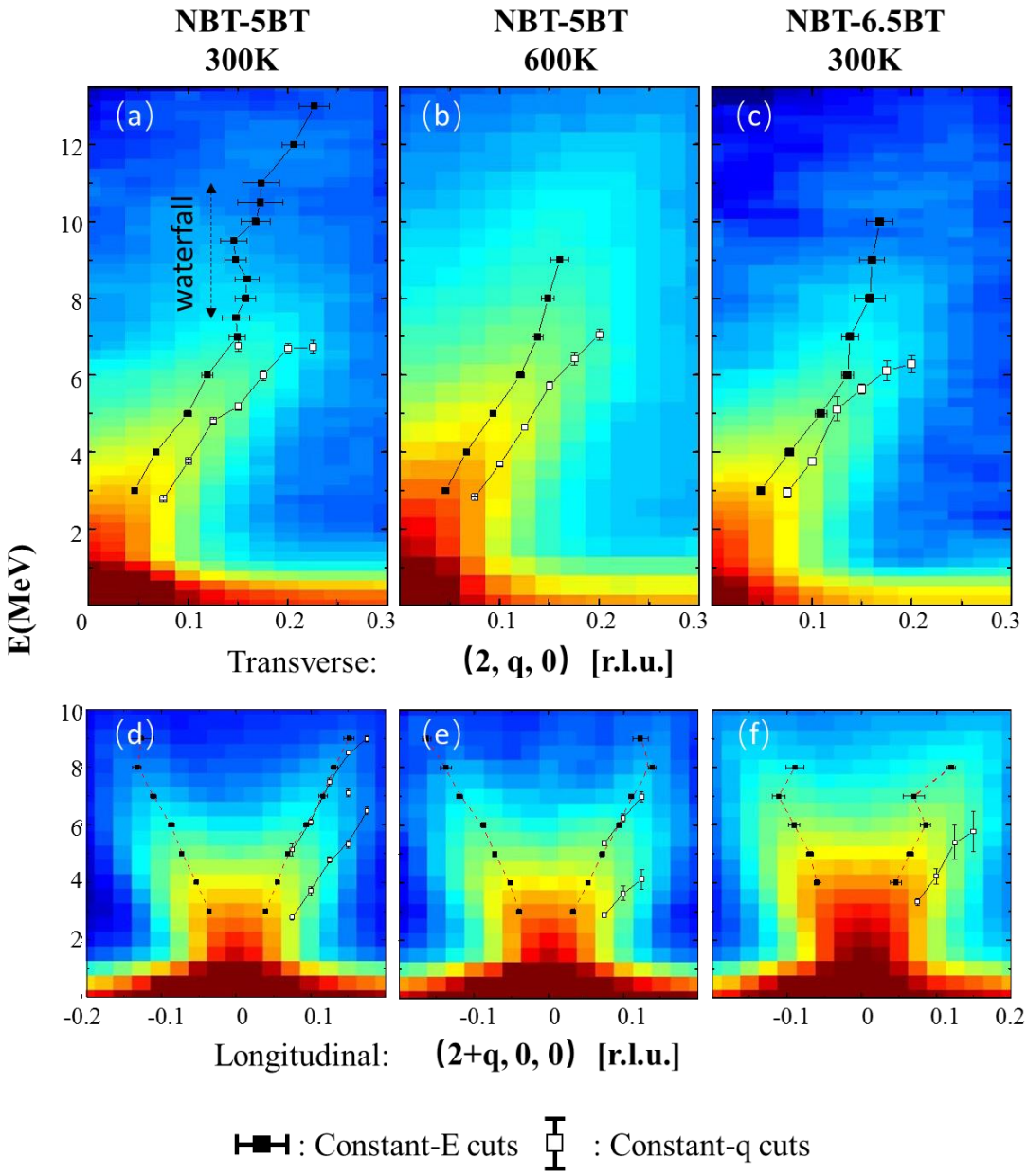

Figure 7.4: Inelastic neutron scattering taken near the (200) zone. The figure is divided into three rows for (a)(d) NBT-5BT at 300K, (b)(e) NBT-5BT at 600K and (c)(f) NBT-6.5BT at 300K. Likewise, it is divided into two columns for phonons in (a)(b)(c) transverse modes and (d)(e)(f) longitudinal modes.

For the longitudinal Δ_1 phonon modes, observed changes based on temperature and composition variations were quite small, as can be seen in Figure 7.4d-f. Unlike previous studies involving NBT [128], the LO branches in Figure 7.4d-f never dropped into the LA branches at room temperature; nor was any LA branch splitting observed. We did, however, observe strong inelastic diffuse scattering near the in-phase superlattice reflections, or M-points, as shown in Figure 7.5. Intense scattering "columns" (intensity signal spread over a range of energies at a fixed wave vector) were observed above the allowed M-points up to at least 7meV. Along the [2.5K0] direction (Figure 7.5a-c), these M-point columns had no distinguished dispersion along q. The intensity and height of these columns were not significantly impacted by changes in temperature or BT content.

In addition to the strong diffuse scattering columns along (110) (see Figure 7.5d-f), transverse $\sum 5$ phonons near the (210) zone were found that connect the M-point columns. In contrast, elastic slices from both neutron and XRD data revealed that the M-points were not connected to any Bragg peaks by diffuse scatterings in the (HK0) planes. Because the optic phonons shown in Figure 7.5 being too weak to be distinguished, the combination of two acoustic modes (marked by a dashed line in Figure 7.5d) was only distinguishable between the M-points and $\sum 5$ TA branches. Figure 7.5d-f illustrates changes in these combinations with changes in temperature and composition—specifically, it was stronger for NBT-5BT than NBT-6.5BT, but nearly dampened out when NBT-5BT was heated to 600K. As mentioned in connection to Figure 7.2, the diffuse scattering connecting the (120) and the (210) reflections did not touch the allowed M-point. This observation demonstrates that the allowed M-points are isolated in the elastic scatterings, but exhibit the combinations of zone-center and zone-boundary acoustic modes along the [110] direction. To better understand the importance of these energy columns, it will be necessary to consider them together with inelastic diffuse scatterings data taken near the R-points.

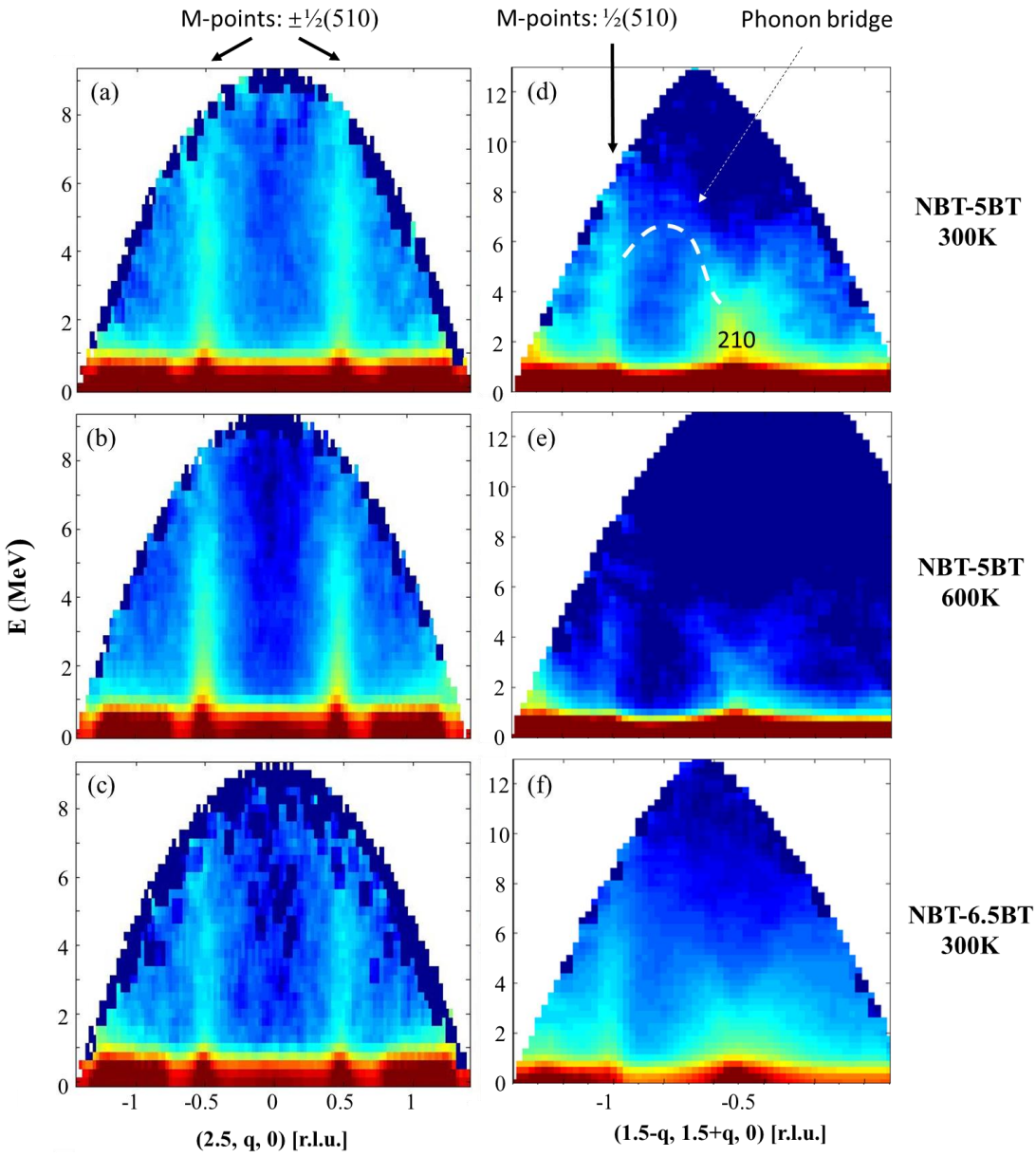

Figure 7.5: Inelastic neutron scattering of (a)(d) NBT-5BT at 300K, (b)(e) NBT-6.5BT at 300K and (c)(f) NBT-5BT at 600K. These data were taken along the (a)(b)(c) (2.5, q, 0) and (d)(e)(f) (1.5-q, 1.5+q, 0). The energy columns near the allowed M-points ½(5±10) are marked by arrows in (a) and (d). The polarizations of the phonons in the two columns are different.

An experiment conducted in the second beam time tested samples of larger size and quantity compared to the first beam time. Figure 7.6a-f show a panel of neutron elastic scattering patterns for NBT-7.5/5/4BT at temperatures of 300/540/700K. These data were taken along the (HHL) plane. The horizontal and vertical axes are along the (00L) direction and the (HH0) direction, respectively.

First, multiple arc-shaped elastic diffuse scatterings can be seen for both NBT-5BT and NBT-7.5BT, which are connected to the different sample mosaics, sizes, and packages. Second, both M-points and R-points can clearly be seen to coexist. Detailed 1-D cuts across different zones are plotted in Figure 7.6h-j. It is necessary to again mention that the M-points ½(330) are forbidden in a perfect P4bm space group, as indicated in reference to Figure 7.2.

Figure 7.6h-j focus on the (-1.5, -1.5, q) direction in 1-D cuts. These cuts cross both the forbidden M-points and the R-points. In each sub-figure, the peaks from left to right are the R-point ½(-3, -3, 1), the forbidden M-point ½(-3, -3, 0) and the R-point ½(-3, -3, -1), as indicated. Please note that the all the M-points in the (HHL) plane were strongly damped; only the ½(-3, -3, 0) reflections had a weak, broad and isotropic diffuse scattering shape. These results confirmed that although the M-point ½(330) is forbidden, it was still observable in the results of the second beam time. This outcome is probably due to imperfections in the large crystals. Here, the result from the forbidden M-points is totally different from the sharper and more intense findings in the (HK0) plane for the allowed M-points.

The intensity and FWHM of the forbidden M-point peaks are principally connected to the local structure within the average symmetry. Furthermore, NBT-5BT at room temperature (red line in Figure 7.6i and black line in Figure 7.6j) featured strong mosaic rings that obscured normal peak intensities, making it difficult to extract them. So the 1-D cut of NBT-5BT at room temperature will not be discussed. Compared to prior data depicted in Figure 7.3, the forbidden M-points in Figure 7.6h-j had similar features with changes in temperature

between samples; specifically, the peak intensity decreased gradually with increasing temperature, but maintained the same FWHM.

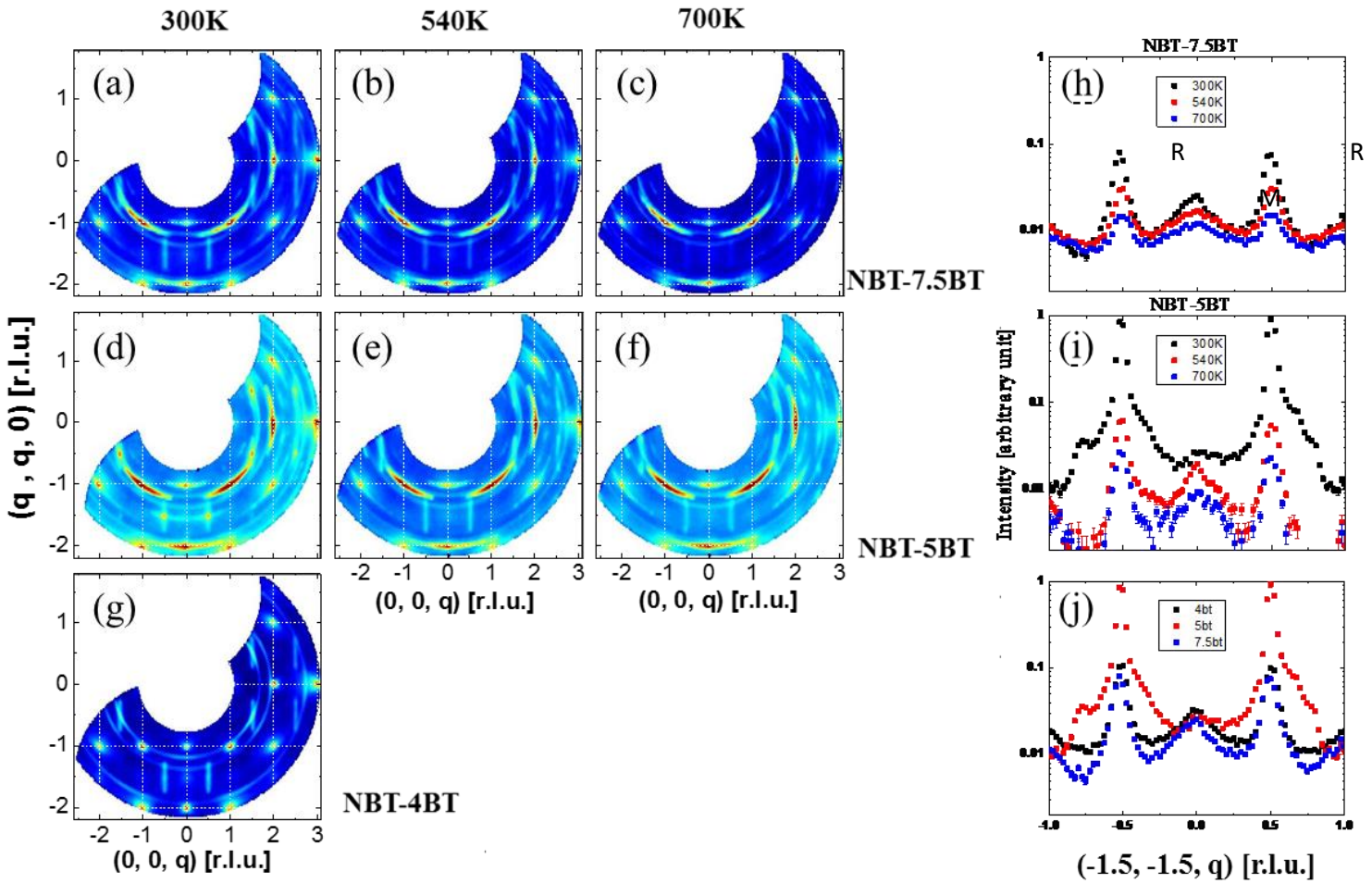

Figure 7.6: Left panel (a)~(g): Neutron elastic scattering patterns taken on the (HHL) plane for (a)-(c) NBT-7.5BT, (d)-(f) NBT-5BT and (g) NBT-4BT. The horizontal and vertical axes are along [00L] and [HH0], respectively. Right panel (h)-(j): Super-lattice changes for NBT-xBT based on the (HHL)

neutron data. Plots compare (h)(i) the same BT contents at different temperatures, and in (j) the various BT contents at room temperatures, respectively. The M-point in (h)-(j) are from the forbidden ½(-3, -3, 0) zone.

One additional feature that should be noted in Figure 7.6 is the unique vertical diffuse scattering around all the observable R-points. This rod-shaped diffraction near the R-points arises from the projection of the X-shaped diffuse scattering within the measurement volume (clarified in 3D views below). Note that this scattering is different from the analogous pattern near (200) in the (HK0) plane, as it is in the [0KL] plane and near the R-point.

Figure 7.7 shows the 3-D neutron elastic scattering patterns taken near the R-point ½(-3, -3, 1). The 3D plots were cut from the [HHL] dataset and their axes are along the [00L], [HH0] and [-HH0] directions. The diffuse scattering streaks across the R-point are along the [100] and [010] directions. Due to the limited [-HH0] range in the [HHL] dataset, the diffraction patterns are actually part of a much larger network. With changes in temperature, these diffuse scattering streaks followed the R-point in the center, and both were dampened out upon heating to between 540K and 700K.

These diffuse scattering streaks feature two main characteristics. They had [100]/[010] orientations, and they crossed the R-points. They were also observed in XRD measurements for NBT-5BT. Figure 7.8 shows the XRD elastic scattering patterns obtained at APS for NBT-5BT at different temperatures. The figures are tilted from the (HK0) plane in order to reach the nearest R-points at ½(511) and ½(531). Smaller images on the right of Figure 7.8a provide a magnified portion of the area focusing on the allowed M-points at ½(501) and the R-points at ½(511). Note also that Figure 7.8a clearly shows a diffuse scattering network. The streaks shown in the magnified image to the right along the [010] direction crossed the allowed M-points at ½(501) and the R-points at ½(511). Additionally, perpendicular [100]-orientated streaks can also be seen in the larger figures on the left side of Figure 7.8a.

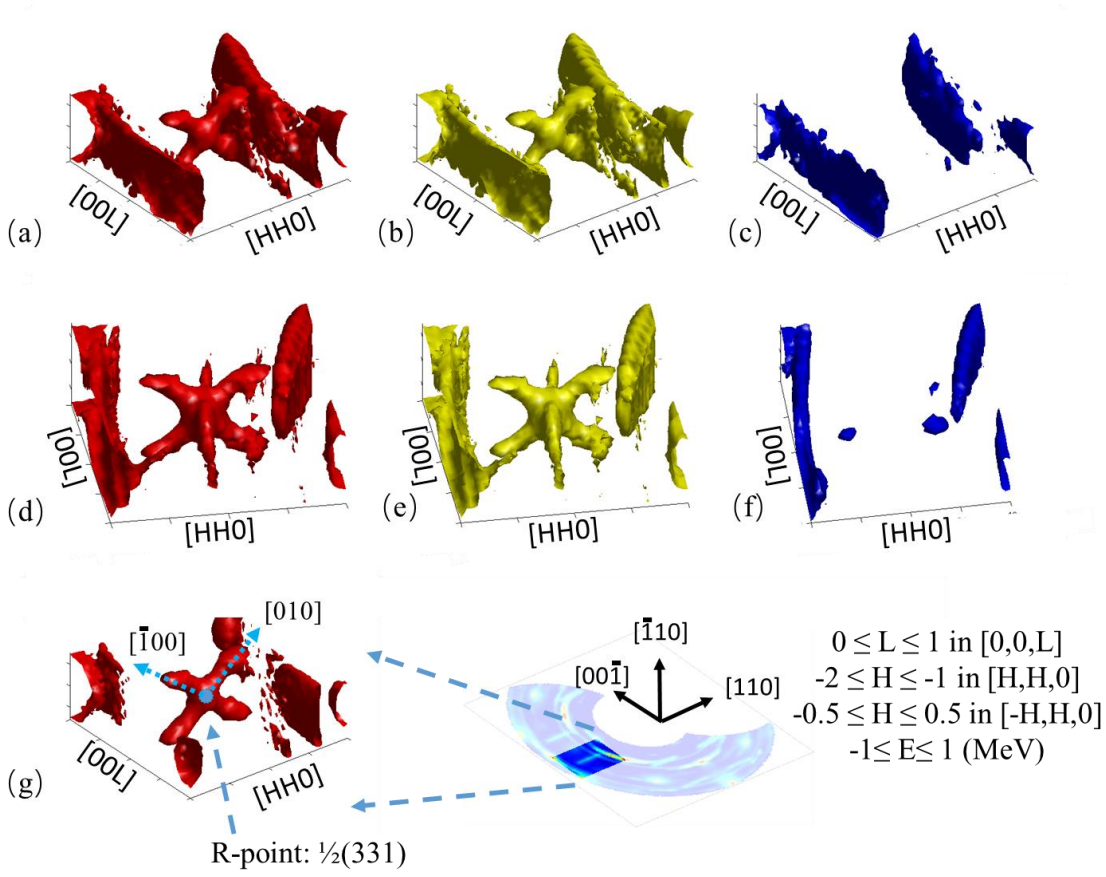

Figure 7.7: 3-D neutron elastic scattering patterns around the R-point (-3/2, -3/2, 0.5) for (a)-(c) NBT-7.5BT, (d)-(f) NBT-5BT and (g) NBT-4BT. The three axes on each figure are along the [00L], [HH0] and [-HH0] directions. All the plots share the same range of [0, 1] in [00L], [-2, -1] in [HH0] and [-0.5, 0.5] in [-HH0]. Colors mark different temperatures, (a)(d)(g) red at 300K, (b)(e) yellow at 540K, and (f)(h) blue at 700K.

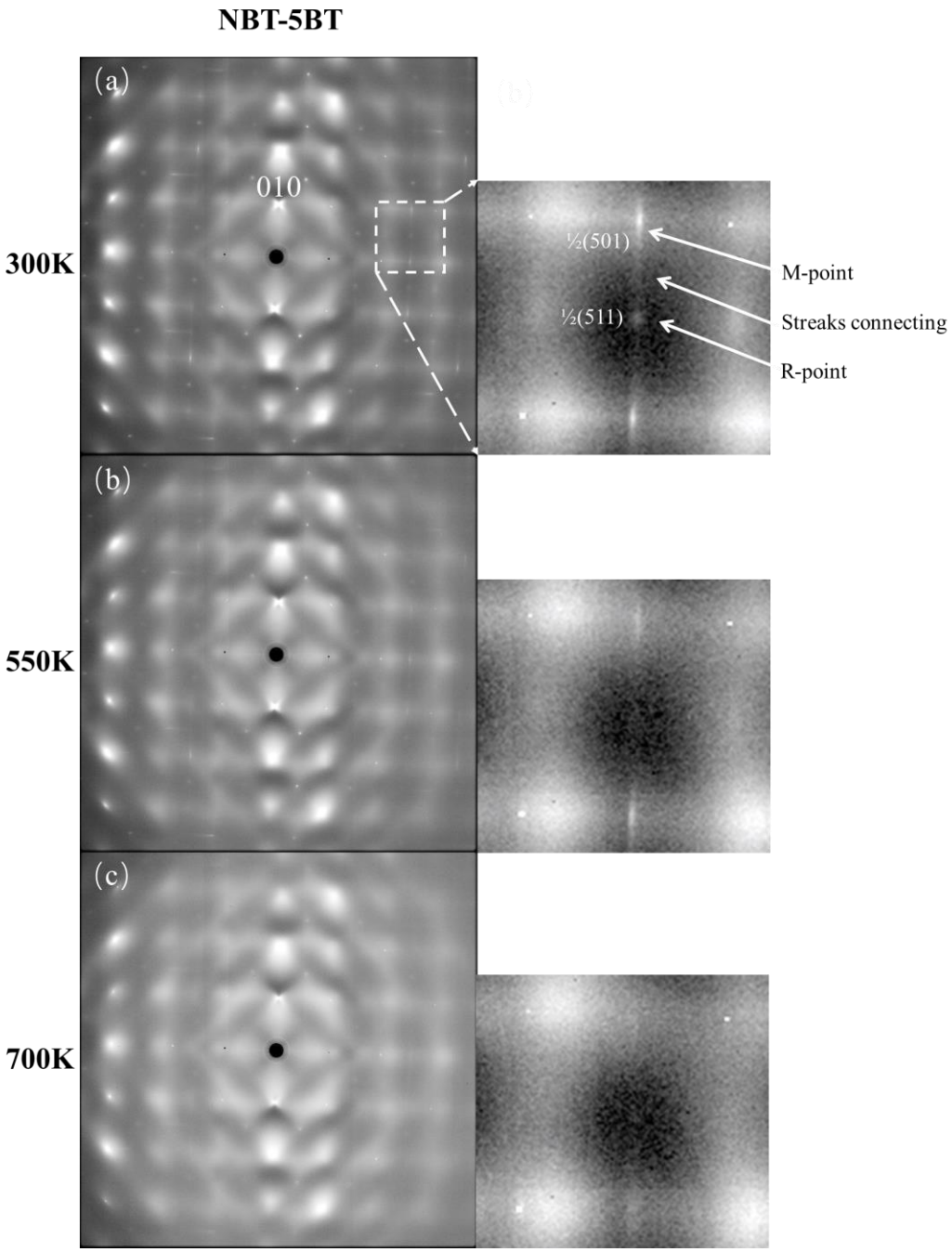

Figure 7.8: XRD elastic scattering patterns tilted from the (HK0) planes taken at APS for NBT-5BT at (a) 300K, (b) 550K and (c) 700K. The tilting angles were the same and were chosen by the maximum intensities of the R-points at ½(511) and ½(531). The smaller images on the right of each panel are higher resolution area images in order to better show the allowed M-points ½(501) and R-points ½(511).

The temperature dependence of the X-shaped diffraction patterns was also investigated. Figure 7.8b-c show the same mesh scans in the (HK0) plane taken at 550K (b) and 700K (c). At 550K (Figure 7.8b), the intensity along [100]/[010] decreased, the M-point intensity slightly decreased, and the R-point was dampened out. When heating to 700K (Figure 7.8c), both the diffuse scattering streaks and the M-point intensities strongly decreased to the point that they were essentially undetectable. Due to these gradual changes in intensity with increasing temperature, it was not necessary to further examine the slight differences in XRD and neutron results, with small relative intensities of both M-points and R-points with increasing temperature.

The remaining APS-XRD data is summarized in Figure 7.9a-b, which focus on two different R-points at ½(511) and ½(531) for various temperatures. The integration was accomplished in the same way as the M-point data processing illustrated in Figure 7.3. The results show similar features as the neutron data. In order to track the superlattice reflection intensity for the various M-points and R-points with temperature, Figure 7.9c plots the integrated intensity determined by Lorentzian peak function fittings. Red lines correspond to the same allowed M-points at ½(310) as shown in Figure 7.2 and Figure 7.3. Blue and black lines pertain to the same NBT-5BT crystal, but show results from two different R-points at ½(511) and ½(531).

Figure 7.9c illustrates an important difference between the integrated intensities associated with allowed M-points and the R-points. The M-points exhibited a nearly linear decrease in intensity with increasing temperature between 300K and 700K; moreover, no anomalies were found at any critical temperature. In contrast, the R-points demonstrated a significant drop in intensity in the vicinity of the ferroelectric transition. Thus, the data show that M-points and R-points coexist only in the ferroelectric phase region—but at higher temperatures, only M-points persist. Additionally, the broad and relative temperature-

independent peak widths indicate that the size of the related in-phase oxygen tilt domains are small and do not change much with temperature.

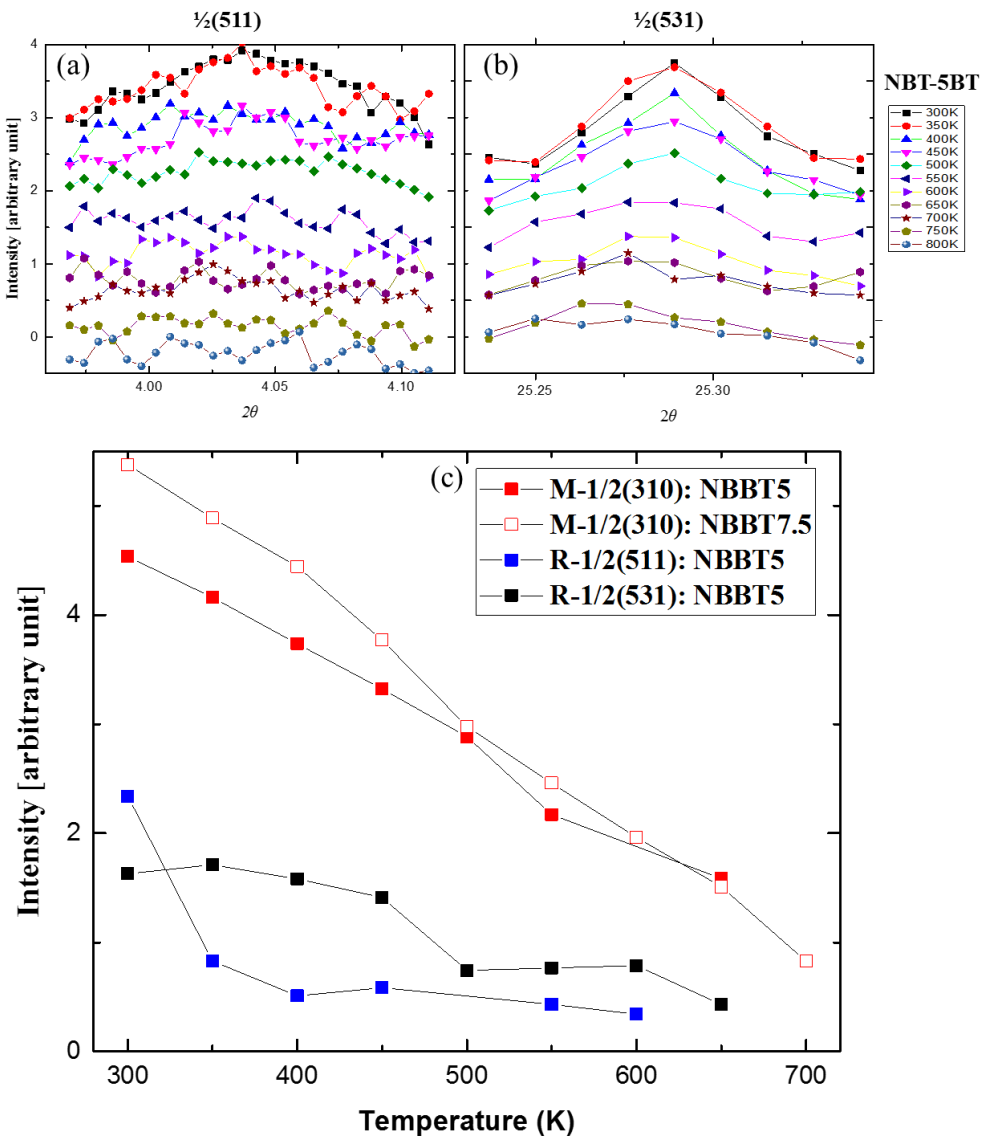

Figure 7.9: Top panel (a)(b): Temperature dependent anti-phase tilting (a) intensity changes of ½(511) reflection for NBT-5BT with increasing temperature, and (b) same for the ½(531) reflection. The intensities were integrated along 2θ. There are fixed offsets between the two neighboring curves to make comparison easier. Bottom panel (c): Temperature dependent super-lattice point intensity changes of NBT-5BT and NBT-7.5BT for the allowed M-point about ½(310) and R-point about ½(511)/ ½(531). The peaks were all fit by a Lorentzian function.

This section examines the inelastic portion of the neutron results based on the same (HHL) plane data. Near the Bragg peak, Figure 7.10 depicts transverse inelastic neutron scatterings

near the (002) zone on the (HHL). (Note that due to different polarizations, the phonons are different from those discussed in reference to Figure 7.4 and Figure 7.5.) The individual images (a-g) illustrate the transverse phonons and related fitting results, with solid dots indicating results from constant-q cuts, and open dots indicating results from constant-E cuts. It should be noted that the red dots represent findings from thinner cuts during the fitting work in comparison to the black ones, and the triangular dots indicate larger fitting errors. Despite these minor differences, there are three important points to note in this figure: (a) the TO phonons never recovered at q=0, (b) the TO phonons shared a flat top at E=16meV, and (c) the TA phonons were also nearly flat in E for q>0.15. Crystals of NBT-5BT and NBT-7.5BT had additional optical phonons near q=0 and E=13meV. And although other phonons were not significantly impacted by temperature changes, the low-q phonons were quite sensitive to temperature. Specifically, for NBT-5BT at 300K, the low-q phonons merged with the TO ones and broadened the entire TO branch.

Similar to the right panel of Figure 7.4, the longitudinal phonons, which was represented by NBT-5BT at 300K in Figure 7.10h, showed little response to changes in temperature or composition. The LA branches were short and steep, while the LO branches had a similar shape to each other. There were no fittings carried out at this point due to the poor phonon resolution.

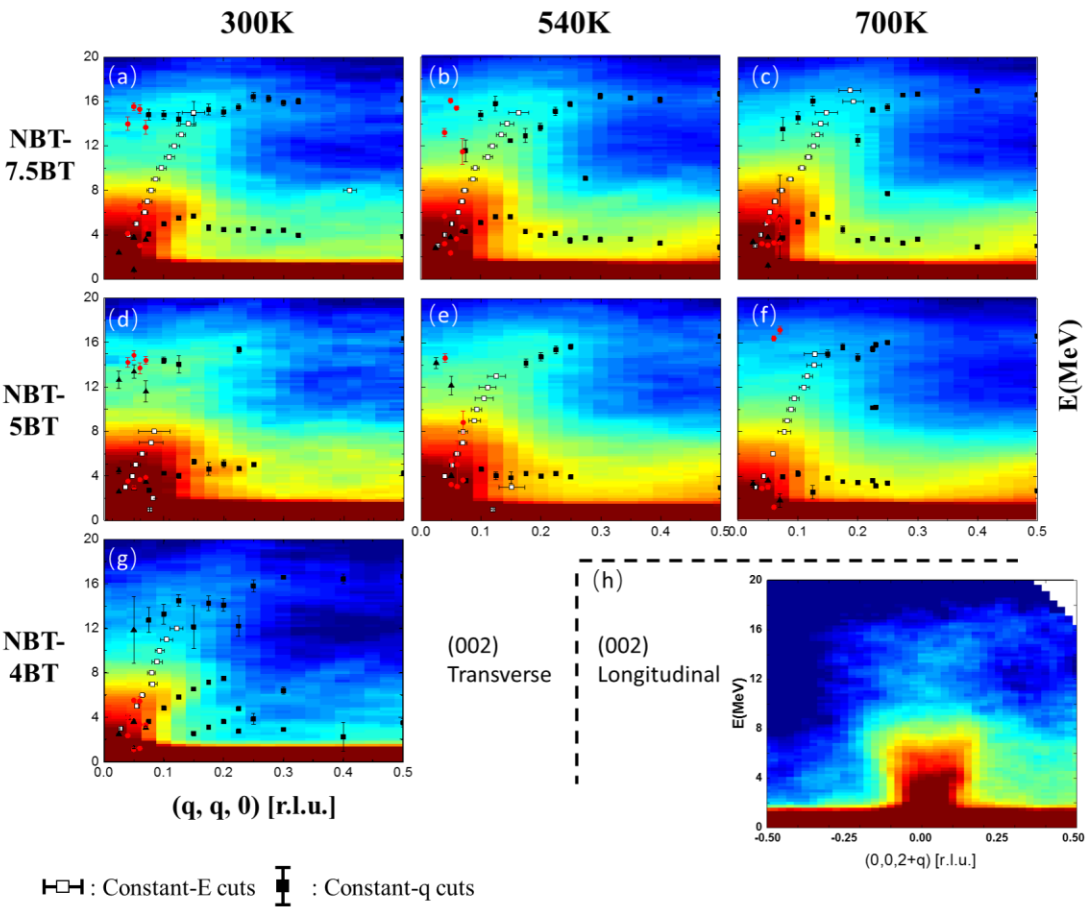

Figure 7.10: Transverse inelastic neutron scatterings near the (002) zone on the (HHL) plane. The main image is divided into three rows for (a)(b)(c) NBT-7.5BT, (d)(e)(f) NBT-5BT and (g) NBT-4BT, as well as three columns for (a)(d)(g) 300K, (b)(e) 540K and (c)(f) 700K. Longitudinal phonons are represented by (h) NBT-5BT at 300K.

Finally, the phonons near the forbidden M-points were also investigated. Figure 7.11 shows the transverse inelastic neutron scatterings near the M-point ½(-3, -3, 0) on the (HHL) plane. Because this dataset is already folded along the [HH0] axis, the R-point and its phonons are located in the middle, and the M-point is situated on the right side. The TO phonon mode of NBT-5BT at 300K had a unique shape in that it featured a flat top of E=16meV, similar to those in Figure 7.10.

Figure 7.11 also shows that in addition to the elastic diffuse scattering streaks across the R-points and the M-points, we also identified an inelastic “phonon band” between these superlattice reflections. Here I use “phonon band” to describe this new feature of soft tilt modes merging from two zone-boundary points. In contrast to the phonons observed near the Bragg peaks (see Figure 7.10), these phonon bands showed a high dependence on changes in temperature and composition. With increasing temperature, the acoustic phonon intensities were enhanced and merged together to make a phonon band whose intensity was significantly stronger. The acoustic phonon band shape did not noticeably change, indicating that the band height of 6~7meV was not affected by temperature.

The composition-dependent band changes reported herein are more noticeable in their shape and intensity characteristics. Most importantly, on both sides of the MPB (i.e. NBT-4BT and NBT-7.5BT), the phonon bands were weak and broken. However, for NBT-5BT near the MPB, the phonon bands were pronounced and continuous. The intrinsic relationship between these phonon bands at the MPB can be described as a type of lattice energy transfer tunnel. This is an important feature to note since the highest piezoelectric properties are always found in any solid solutions near the MPB. This phonon band provides the bridge between microscopic structure and physical performance. The phonon bands also help to explain the M-point energy columns (see Figure 7.5). The intense scattering columns actually represent the side cuts of the phonon bands (see Figure 7.11), and thus have the same energy height.

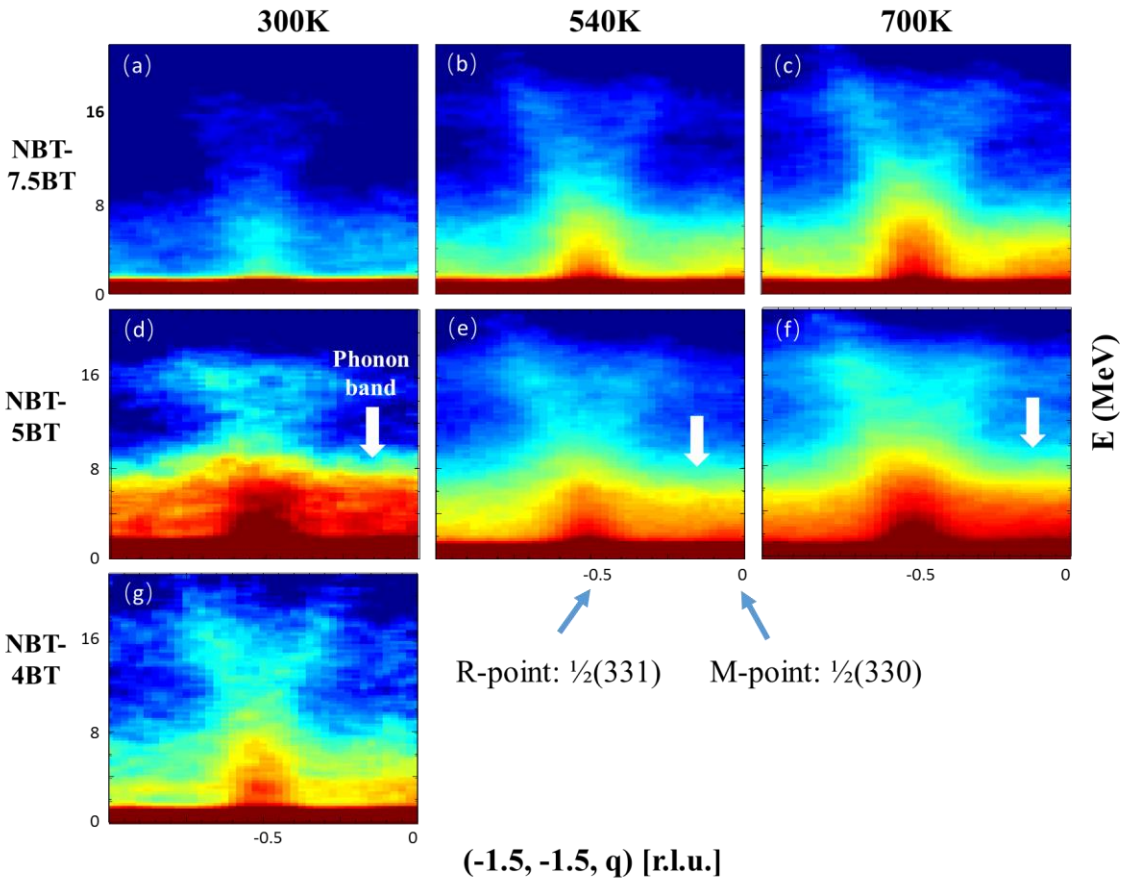

Figure 7.11: Transverse inelastic neutron scattering near the forbidden M-point ½(-3, -3, 0) zone on the (HHL) plane. The figure is divided into three rows for compositions of (a)(b)(c) NBT-7.5BT, (d)(e)(f) NBT-5BT and (g) NBT-4BT; as well as three columns for temperatures of (a)(d)(g) 300K, (b)(e) 540K and (c)(f) 700K. All the images are plotted after being folded along [HH0] axis.

7.4. Data summary

Neutron studies represent a powerful approach in the study of NBT-based solution with an examination of both their elastic and inelastic scattering components. The elastic features that I observed via synchrotron XRD were similar to those I found by neutron investigations. First, I provide a summary of independent observations, which are also highlighted in the last section and related figures.

- There were elastic diffuse ridges along (110) that resulted in oval-shaped and X-shaped diffuse scatterings around different Bragg peaks in the (HK0) plane. Such ridges have previously been reported in connection with the principles of Bragg reflections [57].
- The ½(HH0) M-point is forbidden in both neutron and XRD elastic patterns, as previously reported [97]. However, my neutron results showed weak and isotropic ½(-3,-3,0) reflections on the (HHL) plane, while diffuse ridges crossed the forbidden ½(330) on the (HK0) plane. Additionally, these ridges were damped towards the allowed M-point ½(510).
- There was a "waterfall" effect in the inelastic neutron scattering near the (200) zone in the vicinity of q=0.17 (see Figure 7.4). This waterfall feature had previously been reported in PMN and NBT relaxor-type solid solutions [128, 131]. The waterfall feature was most pronounced near the MPB of NBT-5BT, which heretofore had not been reported, but became less pronounced with increasing temperature.
- There were phonon columns in the vicinity of the allowed M-points only (see Figure 7.5), which were nearly temperature- and composition-independent over the ranges investigated for NBT-xBT. Similar diffuse columns have previously been reported for PMN by Swainson et al. [132], but had not been reported for

NBT-xBT solutions before. Near the (210) zone, transverse acoustic modes were found that connected the allowed M-points columns along the (110) direction; however, elastic scattering studies did not reveal any diffuse scattering connection between them. The diffuse ridge was damped between the allowed M-points and the nearest Γ points. This inelastic-only phonon connectivity with M-points was previously unknown.

- Diffuse streaks were found in the elastic scattering in the vicinity of the R-points that were oriented along [100] and [010] (see Figure 7.7). This feature decreased significantly with increasing temperature near the dielectric constant maximum. These X-shaped features about the R-point superlattice reflections were previously unreported, and differ from those around the Bragg peaks.
- Area integration of the diffraction intensity (see Figure 7.9) around the superlattice reflections revealed that the R-points experienced an abrupt change in the vicinity of the ferroelectric phase transformation at T_{max}. In contrast, the intensity of the allowed M-points gradually decreased with increasing temperature between 300K and 700K. These findings demonstrate that in the high-temperature phase, the M-points exist by themselves; conversely, on cooling into the ferroelectric phase, the M-points and R-points coexist. FHWM analyses confirmed that the M-point and R-point peaks were both very broad and nearly temperature-independent. These features had previously not been known.
- Diffuse streaks in the elastic scattering were observed between the R-points and allowed M-points along [100]/[010] (see Figure 7.8). Such streaks had previously not been reported. These streaks appeared to track with changes in the diffraction intensity from the R-points and M-points

- A phonon band was observed that connected the R-points and forbidden M-points (see Figure 7.11) by inelastic neutron scattering. This phonon band exhibited a strong intensity only near the MPB, which is where maximum piezoelectric properties are found. Note that the M-point at the end of this band is that of the transverse acoustic mode of the forbidden ½(330). In contrast, I found no direct evidence of similar phonon bands between the R-points and allowed M-point. Although the acoustic mode was enhanced at higher temperatures, the phonon band maintained the same height. This finding indicates that the phonon band and phonon columns (see Figure 7.5) may have the same origin, where the phonon columns represent the side cuts of the phonon band across the M-points.

Figure 7.12 provides a schematic illustrating a model that helps to better visualize a number of the observations. In particular, it considers the contributions of both elastic scattering (Figure 7.12a) and inelastic diffuse scattering (Figure 7.12b). In Figure 7.12a, the white spheres represent the Bragg peaks at the pseudocubic lattice points. The cyan sphere center is the R-point. The M-points are divided into two types. First, the blue spheres represent the forbidden M-points shown in Figure 7.6, which are forbidden by the P4bm space group symmetry. They were not observed from either XRD or (HK0) neutron data. However, along (HHL) the neutron data obtained from the larger and more mosaic samples revealed weak M-points at ½(-3,-3,0), which featured broad and isotropic diffuse scattering. Secondly, the allowed M-points (in purple) exhibited a spindle-shaped diffuse scattering (see Figure 7.2d). Furthermore, in addition to the superlattice reflections, strong elastic diffuse scattering streaks were identified between them, which resulted in the apparent formation of a network along the (100)/(010) directions (see Figure 7.7/Figure 7.8). The streaking network is illustrated in Figure 7.12a by the red rods that connect the R-points and allowed M-points. Several rotations of the elastic diffuse scattering schematic model of Figure 7.12a are

provided in Figure 7.12c, which shows different 2-D and 3-D projections of the streaking network.

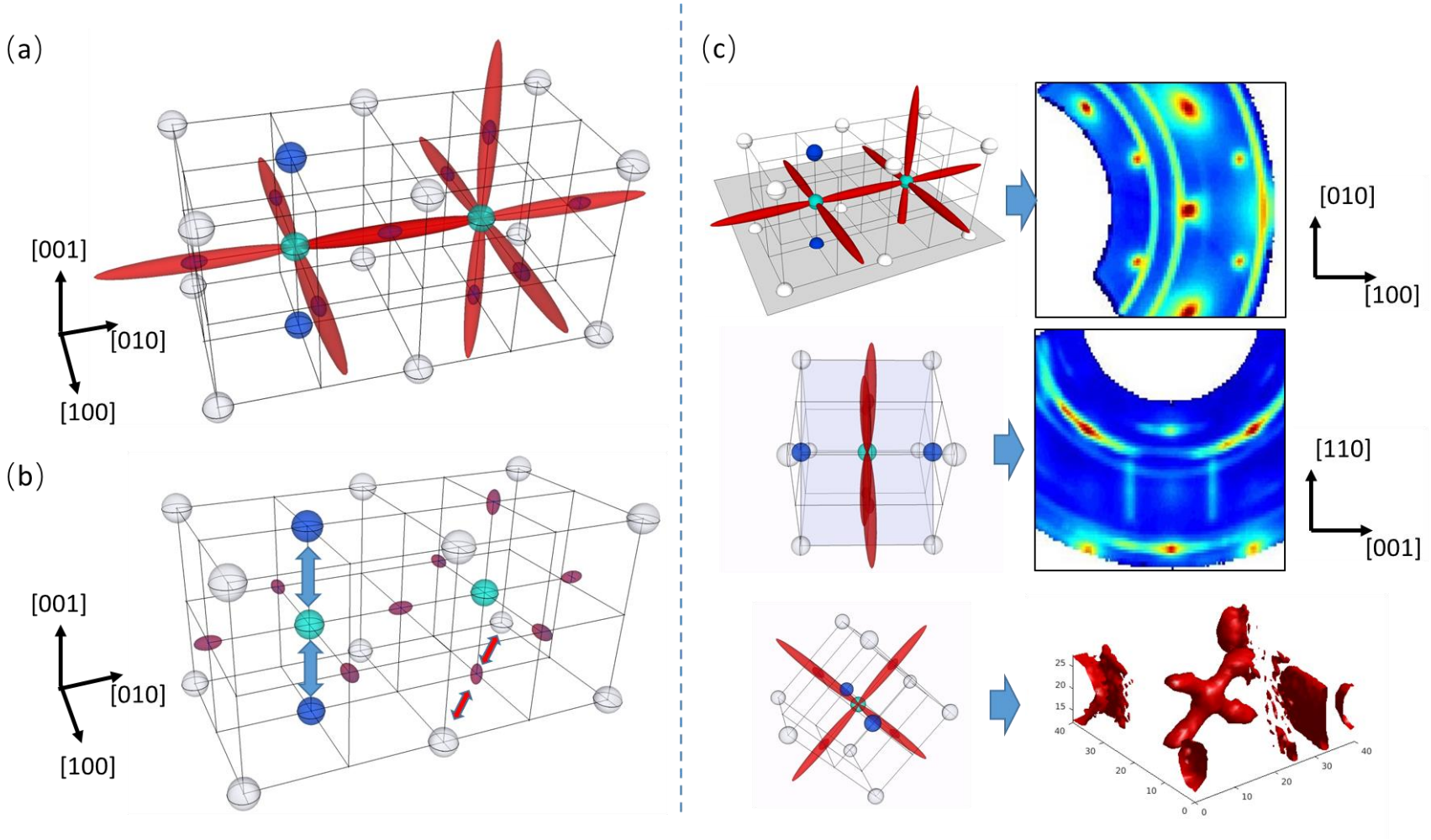

Figure 7.12: Schematic of diffuse scattering streaks for NBT-xBT: (a) Elastic network across the super-lattice points. (b) Inelastic phonon bands (blue) and phonon links (red). (c) Demonstrations of how to offer the elastic slices from the schematic in (a). White spheres are Bragg peaks in the pseudocubic lattice, the R-point is marked by cyan spheres, the different types of M-points are marked by blue spheres and purple spindle-shape spheres.

Neutron and XRD measurements provide complementary perspectives of the same diffuse scattering streaking networks. First, the top panel of Figure 7.12c shows the elastic network projected onto the (HK0) plane (see data in Figure 7.2 and Figure 7.3). The network penetrated the (HK0) plane at the allowed M-points and featured spindle-shaped diffuse scattering (see Figure 7.12d). Secondly, the middle panel shows another projection onto the (HHL) plane. The rod-shaped diffuse scattering around the R-points result from the streaking networks, which are integrated along a limited [-HH0] range. Finally, 3-D projections (see data in Figure 7.7) are shown in the bottom panel of Figure 7.12c, which illustrates that the X-shaped diffuse scattering near the R-points is actually a part of a larger diffuse scattering network. Overall, the elastic diffuse scattering network had a pseudocubic lattice with the R-points located at the cell corners, the allowed M-points located at the middle of each edge, while leaving the forbidden M-points isolated.

As shown in Figure 7.12b, the phonons that crossed the superlattice points are summarized and their locations are marked. The weak phonon links between the M-points and Bragg peaks (see Figure 7.5) are illustrated in Figure 7.12b by red arrows. Also, the phonon band between the forbidden M-points and R-points (see Figure 7.11) are shown as blue arrows in Figure 7.12b. In particular, the phonon bands were found to be sensitive to both temperature and composition changes, unlike the classic waterfall effect or other phonon features. Furthermore, phonon columns were observed along the allowed M-points. These columns were of the same height and also showed the supplementary characteristics of phonon bands due to their same origin. The composition near the MPB displayed the strongest phonon band intensity. I believe that these results are critical for providing an understanding of the dynamical relationship between macroscopic piezoelectric properties and microscopic PNRs, as discussed in the next section.

With respect to MPB composition, the phonon band is the strongest and two different types of PNRs can easily use it to transfer energy between them. Thus, in addition to the importance of phase coexistence, a better understanding of phonon bands represents a key avenue for developing the applications potential of next-generation piezoelectric materials. On the MPB composition, the band is the strongest and two different kinds of PNR can easily use it to transfer energy between each other. In other word, phase coexistence alone, which is a characteristic of many Pb-based and Pb-free compositions even away from MPB, cannot ensure high piezoelectric properties.

7.5. Discussion

Diffuse scattering ridges about the (100) zone along the (110) are well known in both PMN-PT and NBT-BT systems, as also observed herein. Indeed, diffuse scattering ridges are a common feature to both Pb-based and Pb-free perovskite relaxor solid solutions. These ridges have been attributed to nanoscale inhomogeneous polarization distributions along a given direction. They also reflect the presence in real space of polar nanoregions (PNR) that organize into hierarchical domain structures along (110). Another common point is that this type of diffuse scattering is suppressed in the high-temperature range (>Tc) for both Pb-based and Pb-free relaxors, which illustrates a close relationship to polarization. It should be noted, however, that for PMN-PT[133], the (110)-oriented diffuse scattering is significant in the PMN on the rhombohedral side of the MPB. In contrast, this strong diffuse scattering from PNRs is damped on the tetragonal side of the MPB in favor of a long-range, structurally-ordered ground state. However, in NBT-BT, such (110)-oriented diffuse scattering appears at the MPB composition instead of the (100)/(010)-oriented diffuse scattering of NBT along the same zone [57, 125]. Such a difference clearly shows that at the MPB composition of NBT-BT, the PNR distribution is essentially related to its ferroelectric properties. Furthermore, due

to the coexistence of different types of PNRs, NBT-BT has a unique hierarchical domain structure.

Among the elastic diffuse scattering results reported herein, the solid solution NBT-x%BT is also different from PMN-x%PT in one notable regard: it features multiple oxygen octahedral tilt systems, i.e., the M-points and R-points. Yao et al. [31, 43] reported a hierarchical domain structure, where PNRs form on cooling within the geometrical restrictions imposed by the inheritance of a high temperatures ferroelastic phase consisting of nm-sized oxygen tilt domains. Dark field imaging of the superlattice reflections revealed tilt domains of a few nm in size, which likely prevented a range of PNRs from achieving the elastic compatibility conditions of the relaxed state. Rather, a PNR distribution with a vortex morphology was shown to have formed, as described in Chapter V (see Figure 5.3).

Yao et al. [129] further discovered that both M-point and R-point tilt domains co-existed in NBT-x%BT for compositions around the MPB. The researchers indicated that the presence of both types of tilt domains (a) increased Ti-content, which favored the tetragonal phase and M-tilt domains, and (b) decreased Ti, which favored the rhombohedral phase and R-tilt domains. My results show that with increasing temperature between 300K and 700K, the intensity of the allowed M-points gradually decreased, but the R-point intensity disappeared near the ferroelectric phase transformation. These findings suggest two conclusions: (a) in the high-temperature phase, the M-points exist by themselves, and (b) upon cooling into the ferroelectric phase, the M-points and R-points coexist. FHWM-based analyses revealed that the M-point and R-point peaks were both very broad and nearly temperature-independent. These features had previously not been reported.

It should also be noted that the diffuse streaks in the vicinity of the R-points, resulting in X-shaped features, have also previously not been reported. I propose that they are a result of the stacking of neighboring tilt domains. The fact that the [100]/[010] orientation of the

streaks was notably different than the (110) ridges along the principle (100) zone indicates that the oxygen tilt domains tend to organize differently in comparison to the PNRs. Furthermore, streaking along the [100]/[010] extended across the entire reciprocal space range between the R-points and allowed M-points. This phenomenon reflects the fact that the M-points and R-points coexist, and that they may be stacked along the [100]/[010] together. The broad streaking along this direction then demonstrates that the stacking sequence is not regular and that the sizes of the tilt domains are not the same. This streaking results in the R-points and allowed M-points being interconnected through their elastic diffuse scattering (i.e., static distortions).

The net result of these competing processes could, unfortunately, prevent multiple domain states from reaching their relaxed condition. If that be the case, the polarization and different oxygen tilt systems would then constrain each other. Unlike the case for the PMN-x%PT system, PNR distribution cannot be altered by applied field or stress (following adaptive phase theory)—nor can the polarization of the monoclinic phase rotate in an easy plane (following homogeneous theory). Rather, the primary tool for shape change is the length extensional mechanism, as recently shown by Ge et al. [57]. As a consequence, the piezoelectric properties of NBT-x%BT are significantly lower than the analogous properties reported for lead-based relaxor single crystal systems. To enhance the piezoelectricity in these Pb-free system, therefore, one must begin to liberate polarization from the oxygen tilt system.

In addition to the allowed M-points, weak and isotropic ½(330) M-points were also found. These points are forbidden by the P4bm symmetry of the tetragonal phase. This forbidden point was found to be located in the middle of the diffuse scattering ridge between the (210)

and (120) reflections. This weak superlattice reflection is undoubtedly due to the imperfections associated with the translational invariance of the tetragonal phase with average P4bm symmetry, and reflects the inherent inhomogeneity of the oxygen tilt and polarization subsystems. The stacking of M-tilt and R-tilt domains of nm-size, along with the presence of a high density of PNR boundaries, is far from the perfect symmetry for P4bm. Additionally, these forbidden M-points were not interconnected to either the R-points or allowed M-points via elastic diffuse scattering. However, this discussion only considers the static distortions determined from elastic diffuse scattering. In fact, one also needs to consider the phonon dynamics of the inelastic diffuse scattering in order to fully understand how the different modes are interconnected.

I discovered that the lattice dynamics of NBT-x%BT are similar to those previously reported for PMN [132], except in a few important details. Specifically, the lattice dynamics of both these solid solutions were different than conventional ferroelectrics in two notable ways. The first is the presence of the waterfall effect, which is characterized by the broadening in the energy of the lowest energy TO mode. The second is the presence of phonon columns in the vicinity of the allowed M-points, which are very unusual given the fact that the line shape is localized in momentum, but broad in energy. No physical reason has yet been given to explain the existence of phonon columns in PMN—and thus, by inference, with our report of their presence in NBT-x%BT. Columns of diffuse scattering have been associated with a coupling of the lattice with other degrees of freedom [132]. Therefore, it is reasonable to attribute them in NBT-x%BT to the coupling between polarization and oxygen tilt through rotostriction [134] over limited length scales in an inhomogeneous relaxor-like system. This speculation is supported by the fact that the presence of these phonon columns was clearly temperature-independent over the temperature

range that we investigated (300-700K). In prior research of PMN compounds, the phonon columns were found to soften with decreasing temperature below the dielectric maximum due to a softening of the optic phonon mode [132]. This outcome demonstrates that the phonon columns in NBT-x%BT were not directly related to the formation of polarization, but rather persisted into the high-temperature phase region where the M-type oxygen rotations remain present, even at temperatures exceeding 700K.

One detail concerning phonon columns that was different for NBT-x%BT (compared to PMN) is the presence of a phonon bridge that linked the allowed M-points to the (210) zone (see Figure 7.5d). This features indicates that vibration energy was transferred between the allowed M-points and this principal zone, along which diffuse elastic scattering ridges were observed. Thus, the allowed M-points are not dynamically isolated. This Σ-type (linking Γ and M points) phonon bridge is strongest near the MPB, where the piezoelectric properties were also the strongest. Furthermore, the phonon bridge was found to be notably temperature-dependent, quite similar to the T-type (linking R and M points) in PMN [132], which was found to disappear upon heating above the ferroelectric transition temperature. The temperature- and composition-dependent phonon bridge represents a unique ferroelectric mode at the MPB.

Another characteristic phonon signature of the MPB region, which was not observed for the other compositions, must be noted. This feature is the presence of phonon bands connecting the R-points to the forbidden M-points in the (HHL) plane, as shown in Figure 7.11. This band clearly demonstrates that the R-points and forbidden M-points are not dynamically isolated from each other. Due to its low energy and temperature-independence at the M points, one can infer that this phonon band is the result of the oxygen octahedral tilt

modes. Indeed, this band mode is distinctly different compared to the soft optic modes at the M point columns of PMN [132]. This finding may have important ramifications for the transfer of vibrational energy under application of an electric field or mechanical stress between different tilt modes, with regards to facilitating enhanced piezoelectricity.

Thus, in studies of compositions near the MPB and their acoustic mode combinations related to the superlattice reflections, two important findings emerged: (a) the R-points and forbidden M-points are interconnected through phonon bands, and (b) the allowed M-points are interconnected through the acoustic mode combination to the (210). These critical elements are not present in the other compositions away from the MPB, which may play an important role in the repartition of energy between the different modes. In addition to phase and PNR coexistence, the presence and behavior of phonon bands appear to play a key role in the development of next-generation Pb-free piezoelectric materials. These phonon bands may enable the transfer of energy between two oxygen octahedral tilt systems and within the relevant PNRs coexistence, which is critical to enhanced piezoelectricity. By redistributing energy between the different modes, the system can partially relax, and the oxygen tilt domains and PNRs can readjust and accommodate each other. This process, in turn, can allow the material to express higher induced shape changes in response to stimuli in comparison to a response facilitated by a length extensional mechanism.

8. Summary

In this dissertation, NBT-derived single crystals were analyzed using multiple methods such as XRD, TEM, and neutron scattering. Under the framework of polar nanoregions and adaptive phase theory, I sought to determine how nanostructure and typical structures change with temperature and composition—and most importantly, how these parameters impact resulting piezoelectric properties. Diffuse scattering, domain morphology, and phonon dispersions were used to connect the static and dynamic description of the heterogeneous structure.

First, the structure of NBT-x%BT was investigated to improve the phase diagrams using the XRD method. The crystallographic dependence of the DC electric field-induced strains and phase transitions in Na0.5Bi0.5TiO3-5.6%BaTiO3 single crystals were also investigated. The results indicated a largely static phase background for compositions at the the MPB.

Secondly, the ferroelectric domain and local structures of NBT-x%KBT single crystals were investigated by various TEM methods. The presence of a unique hierarchical domain structure was found.

In addition, the phase transition sequence of C→T→MC was found for PIN-PMN-PT crystals in the FC condition based on XRD results; a detailed E-Temp diagram was constructed to summarize the findings. A model of PNR was also developed to explain the phase coexistence during phase transitions.

Finally, neutron diffraction was used to study NBT-x%BT single crystals, including both their elastic and inelastic scattering components. The results show a unique diffuse scattering and phonon linkage through different types of superlattice points, revealing a close static/dynamic relationship between M-type and R-type oxygen octahedron tiltings. Furthermore, a phonon band appeared at the MPB, which may serve as energy transfer tunnel

that is highly composition-dependent. The findings described herein are expected to fill a scholarly gap in our understanding of the microstructure and the macro properties of NBT-x%BT.

9. Future work

First, XRD studies have already provided a huge amount of data on the phase transition behavior of Pb-free piezoelectric single crystals. However, traditional XRD approaches that reveal the "skin effects" of these crystals may be in conflict with other methods that can penetrate deeper into the crystal. Thus. future work needs to be done using high-energy XRD for more compositions and orientations of NBT-based single crystals. Also, using the developing technology of 3D modeling—and its unique advantages in elucidating PNR microstructure—additional research should focus on 3D diffuse scattering measurements and what they can tell us about the complex behavior of these crystals.

Secondly, our TEM studies have revealed the relationship between octahedral tiltings and unique domain structure changes in solid solution. Although high background noise tends to make TEM inadequate for tracking weak octahedral tiltings, *in situ* methods of TEM have already proven to be advantageous by tracking domain morphology changes in a fixed area. Future work will need to link domain structure with phase diagrams determined by XRD.

Finally, while emerging neutron studies bring new findings to the nature, behavior and applications potential of NBT-x%BT single crystals, additional questions remain to be answered. In addition to investigating bigger crystals for neutron measurements, future work involving neutron studies needs to focus on the following topics:

- More elastic plane types, in addition to the (HK0) and (HHL), need to be scanned—especially those containing multiple types of superlattice points. The diffuse scattering streak networks require additional scanning to elucidate their nature.

- Due to the fact that phonon bands were observed between the forbidden M-points and R-points, additional studies should be conducted to confirm the presence of analogous bands between the allowed M-points and R-points.
- Further group analysis needs to be conducted with the goal of producing more detailed phonon marking. Because it was restricted to a low-resolution investigation, the present study was unable to distinguish the acoustic and optic branches on the low-energy part clearly. Future studies should be designed to address this deficit.

Reference

1. Park, S.E. and T.R. Shrout, *Ultrahigh strain and piezoelectric behavior in relaxor based ferroelectric single crystals.* Journal of Applied Physics, 1997. **82**(4): p. 1804-1811.
2. Kanegae, T., K. Sakata, and T. Takenaka, *Pb(Zn1/3nb2/3)O3-Based Piezoelectric and Electrostrictive Ceramics.* Japanese Journal of Applied Physics Part 1-Regular Papers Short Notes & Review Papers, 1991. **30**(9b): p. 2232-2235.
3. Han, P.D., et al., *Cut directions for the optimization of piezoelectric coefficients of lead magnesium niobate-lead titanate ferroelectric crystals.* Applied Physics Letters, 2005. **86**(5): p. 3.
4. Noheda, B., *Structure and high-piezoelectricity in lead oxide solid solutions.* Current Opinion in Solid State & Materials Science, 2002. **6**(1): p. 27-34.
5. Takenaka, T. and H. Nagata, *Current status and prospects of lead-free piezoelectric ceramics.* Journal of the European Ceramic Society, 2005. **25**(12): p. 2693-2700.
6. Panda, P.K., *Review: environmental friendly lead-free piezoelectric materials.* Journal of Materials Science, 2009. **44**(19): p. 5049-5062.
7. Maeder, M.D., D. Damjanovic, and N. Setter, *Lead free piezoelectric materials.* Journal of Electroceramics, 2004. **13**(1-3): p. 385-392.
8. Shrout, T.R. and S.J. Zhang, *Lead-free piezoelectric ceramics: Alternatives for PZT?* Journal of Electroceramics, 2007. **19**(1): p. 113-126.
9. Zhang, Q.H., et al., *Enhanced piezoelectric and ferroelectric properties in Mn-doped Na0.5Bi0.5TiO3-BaTiO3 single crystals.* Applied Physics Letters, 2009. **95**(10): p. 102904, 3pp.
10. Damjanovic, D., *Comments on origins of enhanced piezoelectric properties in ferroelectrics.* IEEE Trans Ultrason Ferroelectr Freq Control, 2009. **56**(8): p. 1574-85.
11. Kasap, S.O., *Principles of Electronic Materials and Devices, 2nd edn.* 2002, New York: McGraw-Hill.
12. Jo, W., et al., *Giant electric-field-induced strains in lead-free ceramics for actuator applications – status and perspective.* Journal of Electroceramics, 2012. **29**(1): p. 71-93.
13. Fu, D. and M. Itoh, *Ferroelectricity in Silver Perovskite Oxides*. Ferroelectrics - Material Aspects. 2011.
14. Cross, L.E., *Relaxor Ferroelectrics.* Ferroelectrics, 1987. **76**(3-4): p. 241-267.
15. Shirane, G. and K. Suzuki, *Crystal Structure of Pb(Zr-Ti)O3.* Journal of the Physical Society of Japan, 1952. **7**(3): p. 333-333.
16. Leontsev, S.O. and R.E. Eitel, *Progress in engineering high strain lead-free piezoelectric ceramics.* Science and Technology of Advanced Materials, 2010. **11**(4): p. 044302.
17. Jaffe, B., R.S. Roth, and S. Marzullo, *Piezoelectric Properties of Lead Zirconate-Lead Titanate Solid-Solution Ceramics.* Journal of Applied Physics, 1954. **25**(6): p. 809-810.
18. Jaffe, H. and D.A. Berlincourt, *Piezoelectric Transducer Materials.* Proceedings of the Institute of Electrical and Electronics Engineers, 1965. **53**(10): p. 1372-+.
19. Jo, W., et al., *Giant electric-field-induced strains in lead-free ceramics for actuator applications - status and perspective.* Journal of Electroceramics, 2012. **29**(1): p. 71-93.
20. Smolenskii, G., et al., *New Ferroelectrics of Complex Composition.* Sov. Phys.-Solid State, 1960. **2**: p. 2651-2654.
21. Zhang, Q., et al., *Growth and electric properties of 0.96Na0.5Bi0.5TiO3–0.04BaTiO3 single crystal.* Journal of Crystal Growth, 2010. **312**(3): p. 457-460.

22. Takenaka, T., K. Maruyama, and K. Sakata, *$Na_{0.5}Bi_{0.5}TiO_3$-$BaTiO_3$ system for lead-free piezoelectric ceramics.* Japanese Journal of Applied Physics, 1991. **30**(9B): p. 2236-2239.
23. Sasaki, A., et al., *Dielectric and piezoelectric properties of (Bi0.5Na0.5)TiO3-(Bi0.5K0.5)TiO3 systems.* Japanese Journal of Applied Physics Part 1-Regular Papers Short Notes & Review Papers, 1999. **38**(9b): p. 5564-5567.
24. Ge, W.W., et al., *Evolution of structure in Na0.5Bi0.5TiO3 single crystals with BaTiO3.* Applied Physics Letters, 2014. **105**(16): p. 162913.
25. Chiang, Y.M., G.W. Farrey, and A.N. Soukhojak, *Lead-free high-strain single-crystal piezoelectrics in the alkaline-bismuth-titanate perovskite family.* Applied Physics Letters, 1998. **73**(25): p. 3683-3685.
26. Xie, H., et al., *Morphotropic phase boundary, segregation effect and crystal growth in the NBT–KBT system.* Journal of Crystal Growth, 2009. **311**(14): p. 3626-3630.
27. Zhang, H., et al., *Structure and electrical properties of Na1/2Bi1/2TiO3–xK1/2Bi1/2TiO3 lead-free ferroelectric single crystals.* Solid State Communications, 2015. **201**: p. 125-129.
28. Otoničar, M., et al., *Compositional range and electrical properties of the morphotropic phase boundary in the Na0.5Bi0.5TiO3–K0.5Bi0.5TiO3 system.* Journal of the European Ceramic Society, 2010. **30**(4): p. 971-979.
29. Lu, Y.-Q. and Y.-X. Li, *A Review on Lead-Free Piezoelectric Ceramics Studies in China.* Journal of Advanced Dielectrics, 2011. **01**(03): p. 269-288.
30. Mayergoyz, I. and G. Bertotti, *The Science of Hysteresis*. Vol. 3. 2005: Elsevier:.
31. Yao, J.J., et al., *Effect of Mn substituents on the domain and local structures of Na1/2Bi1/2TiO3-BaTiO3 single crystals near a morphotropic phase boundary.* Applied Physics Letters, 2011. **98**(13).
32. Zhang, H.W., et al., *Ultrahigh ferroelectric response in Fe modified 0.95(Na1/2Bi1/2)TiO3-0.05BaTiO(3) single crystals.* Journal of Materials Chemistry C, 2014. **2**(47): p. 10124-10128.
33. Cao, H., *PHD Dissertation: Phase transformations in highly electrostrictive and magnetostrictive crystals: structural heterogeneity and history dependent phase stability*, in *Materials Science and Engineering*. 2008, Virginia Polytechnic Institute and State University: Blacksburg.
34. Vanderbilt, D. and M.H. Cohen, *Monoclinic and triclinic phases in higher-order Devonshire theory.* Physical Review B, 2001. **63**(9): p. 094108.
35. Viehland, D., *Symmetry-adaptive ferroelectric mesostates in oriented Pb(BI1/3BII2/3)O-3-PbTiO3 crystals.* Journal of Applied Physics, 2000. **88**(8): p. 4794-4806.
36. Cao, H., et al., *Fragile phase stability in (1-x)Pb(Mg1/3Nb2/3O3)-xPbTiO(3) crystals: A comparison of [001] and [110] field-cooled phase diagrams.* Physical Review B, 2006. **73**(18): p. 184110.
37. Fu, H. and R.E. Cohen, *Polarization rotation mechanism for ultrahigh electromechanical response in single-crystal piezoelectrics.* Nature, 2000. **403**(6767): p. 281-3.
38. Jin, Y.M., et al., *Adaptive ferroelectric states in systems with low domain wall energy: Tetragonal microdomains.* Journal of Applied Physics, 2003. **94**(5): p. 3629-3640.
39. Wechsler, M.S., D.S. Lieberman, and T.A. Read, *On the Theory of the Formation of Martensite.* Transactions of the American Institute of Mining and Metallurgical Engineers, 1953. **197**(11): p. 1503-1515.
40. Burns, G. and F.H. Dacol, *Glassy Polarization Behavior in Ferroelectric Compounds Pb(Mg1/3nb2/3)O3 and Pb(Zn1/3nb2/3)O3.* Solid State Communications, 1983. **48**(10): p. 853-856.

41. Xu, G.Y., *Probing local polar structures in PZN-xPT and PMN-xPT relaxor ferroelectrics with neutron and x-ray scattering.* International Conference on Frustration in Condensed Matter (Icfcm), 2011. **320**: p. 012081.
42. Bai, F.M., J.F. Li, and D. Viehland, *Domain hierarchy in annealed (001)-oriented Pb(Mg1/3Nb2/3)O-3-x%PbTiO3 single crystals.* Applied Physics Letters, 2004. **85**(12): p. 2313-2315.
43. Yao, J., et al., *Evolution of domain structures in Na1/2Bi1/2TiO3single crystals with BaTiO3.* Physical Review B, 2011. **83**(5): p. 054107.
44. Glazer, A.M., *The classification of tilted octahedra in perovskites.* Acta Crystallographica Section B Structural Crystallography and Crystal Chemistry, 1972. **28**(11): p. 3384-3392.
45. Yao, J.J., et al., *Role of coexisting tetragonal regions in the rhombohedral phase of Na0.5Bi0.5TiO3-xat.%BaTiO3 crystals on enhanced piezoelectric properties on approaching the morphotropic phase boundary.* Applied Physics Letters, 2012. **100**(1): p. 012901.
46. Jones, G.O. and P.A. Thomas, *Investigation of the structure and phase transitions in the novel A-site substituted distorted perovskite compound Na0.5Bi0.5TiO3.* Acta Crystallographica Section B-Structural Science Crystal Engineering and Materials, 2002. **58**: p. 168-178.
47. Ma, C. and X. Tan, *In situ Transmission Electron Microscopy Study on the Phase Transitions in Lead-Free (1-x)(Bi1/2Na1/2)TiO3-xBaTiO(3) Ceramics.* Journal of the American Ceramic Society, 2011. **94**(11): p. 4040-4044.
48. Gorfman, S. and P.A. Thomas, *Evidence for a non-rhombohedral average structure in the lead-free piezoelectric material Na0.5Bi0.5TiO3.* Journal of Applied Crystallography, 2010. **43**(6): p. 1409-1414.
49. Aksel, E., et al., *Structure and properties of Fe-modified Na_{0.5}Bi_{0.5}TiO_{3} at ambient and elevated temperature.* Physical Review B, 2012. **85**(2): p. 024121.
50. Aksel, E., et al., *Phase transition sequence in sodium bismuth titanate observed using high-resolution x-ray diffraction.* Applied Physics Letters, 2011. **99**(22): p. 222901-3.
51. Aksel, E., et al., *Monoclinic crystal structure of polycrystalline $Na_{0.5}Bi_{0.5}TiO_3$.* Applied Physics Letters, 2011. **98**(15): p. 152901.
52. Ma, C. and X. Tan, *Phase diagram of unpoled lead-free (1-x)(Bi1/2Na1/2)TiO3-xBaTiO(3) ceramics.* Solid State Communications, 2010. **150**(33-34): p. 1497-1500.
53. Ma, C., et al., *Domain structure-dielectric property relationship in lead-free (1-x)(Bi1/2Na1/2)TiO3-xBaTiO(3) ceramics.* Journal of Applied Physics, 2010. **108**(10): p. 104105.
54. Schutz, D., et al., *Lone-Pair-Induced Covalency as the Cause of Temperature- and Field-Induced Instabilities in Bismuth Sodium Titanate.* Advanced Functional Materials, 2012. **22**(11): p. 2285-2294.
55. Tan, X.L., H. He, and J.K. Shang, *In situ transmission electron microscopy studies of electric-field-induced phenomena in ferroelectrics.* Journal of Materials Research, 2005. **20**(7): p. 1641-1653.
56. Shapiro, S.M., et al., *HYSPEC: A crystal time-of-flight hybrid spectrometer for the spallation neutron source with polarization capabilities.* Physica B-Condensed Matter, 2006. **385-86**: p. 1107-1109.
57. Ge, W., et al., *Lead-free and lead-basedABO3perovskite relaxors with mixed-valenceA-site andB-site disorder: Comparative neutron scattering structural study of (Na1/2Bi1/2)TiO3and Pb(Mg1/3Nb2/3)O3.* Physical Review B, 2013. **88**(17): p. 174115.

58. Phelan, D., et al., *Role of random electric fields in relaxors.* Proc Natl Acad Sci U S A, 2014. **111**(5): p. 1754-9.
59. Jo, W., et al., *Evolving morphotropic phase boundary in lead-free (Bi[sub 1/2]Na[sub 1/2])TiO[sub 3]–BaTiO[sub 3] piezoceramics.* Journal of Applied Physics, 2011. **109**(1): p. 014110.
60. Zhang, S.T., et al., *Giant strain in lead-free piezoceramics Bi0.5Na0.5TiO3-BaTiO3-K0.5Na0.5NbO3 system.* Applied Physics Letters, 2007. **91**(11): p. 112906.
61. Jo, W., et al., *Origin of the large strain response in (K[sub 0.5]Na[sub 0.5])NbO[sub 3]-modified (Bi[sub 0.5]Na[sub 0.5])TiO[sub 3]–BaTiO[sub 3] lead-free piezoceramics.* Journal of Applied Physics, 2009. **105**(9): p. 094102.
62. Daniels, J.E., et al., *Electric-field-induced phase transformation at a lead-free morphotropic phase boundary: Case study in a 93%(Bi0.5Na0.5)TiO3-7% BaTiO3 piezoelectric ceramic.* Applied Physics Letters, 2009. **95**(3).
63. Daniels, J.E., et al., *Electric-field-induced phase-change behavior in (Bi0.5Na0.5)TiO3-BaTiO3-(K0.5Na0.5)NbO3: A combinatorial investigation.* Acta Materialia, 2010. **58**(6): p. 2103-2111.
64. Hinterstein, M., et al., *Field-induced phase transition in Bi1/2Na1/2TiO3-based lead-free piezoelectric ceramics.* Journal of Applied Crystallography, 2010. **43**(6): p. 1314-1321.
65. Simons, H., et al., *Electric-field-induced strain mechanisms in lead-free 94%(Bi[sub 1/2]Na[sub 1/2])TiO[sub 3]–6%BaTiO[sub 3].* Applied Physics Letters, 2011. **98**(8): p. 082901.
66. Rodel, J., et al., *Perspective on the Development of Lead-free Piezoceramics.* Journal of the American Ceramic Society, 2009. **92**(6): p. 1153-1177.
67. Yao, J., et al., *Role of coexisting tetragonal regions in the rhombohedral phase of Na0.5Bi0.5TiO3-xat.%BaTiO3 crystals on enhanced piezoelectric properties on approaching the morphotropic phase boundary.* Applied Physics Letters, 2012. **100**(1): p. 012901.
68. Cao, H., et al., *Intermediate ferroelectric orthorhombic and monoclinic M-B phases in [110] electric-field-cooled Pb(Mg1/3Nb2/3)O-3-30%PbTiO3 crystals.* Physical Review B, 2005. **72**(6): p. 064104.
69. Cao, H., J.F. Li, and D. Viehland, *Electric-field-induced orthorhombic to monoclinic M-B phase transition in [111] electric field cooled Pb(Mg1/3Nb2/3O3)-30%PbTiO3 crystals.* Journal of Applied Physics, 2006. **100**(8): p. 084102.
70. Bai, F.M., et al., *X-ray and neutron diffraction investigations of the structural phase transformation sequence under electric field in 0.7Pb(Mg1/3Nb2/3)-0.3PbTiO(3) crystal.* Journal of Applied Physics, 2004. **96**(3): p. 1620-1627.
71. Guo, R., et al., *Origin of the high piezoelectric response in PbZr1-xTixO3.* Phys Rev Lett, 2000. **84**(23): p. 5423-6.
72. Schmitt, L.A., et al., *Structural investigations on lead-free Bi1/2Na1/2TiO3-based piezoceramics.* Journal of Materials Science, 2011. **46**(12): p. 4368-4376.
73. Wylie-van Eerd, B., et al., *Structural complexity of(Na0.5Bi0.5)TiO3-BaTiO3as revealed by Raman spectroscopy.* Physical Review B, 2010. **82**(10).
74. Cordero, F., et al., *Phase transitions and phase diagram of the ferroelectric perovskite (Na0.5Bi0.5)(1-x)BaxTiO3 by anelastic and dielectric measurements.* Physical Review B, 2010. **81**(14): p. 144124, 10pp.

75. Ma, C., H. Guo, and X. Tan, *A New Phase Boundary in (Bi1/2Na1/2)TiO3−BaTiO3Revealed via a Novel Method of Electron Diffraction Analysis.* Advanced Functional Materials, 2013. **23**(42): p. 5261-5266.
76. Cohen, R.E., *Materials science: relaxors go critical.* Nature, 2006. **441**(7096): p. 941-2.
77. *A. C. Larson and R. B. Von Dreele, Los Alamos National Laboratory Report LAUR, 2004, pp. 86–748.*
78. Finger, L.W., D.E. Cox, and A.P. Jephcoat, *A Correction for Powder Diffraction Peak Asymmetry Due to Axial Divergence.* Journal of Applied Crystallography, 1994. **27**(6): p. 892-900.
79. Jo, W., et al., *On the phase identity and its thermal evolution of lead free (Bi1/2Na1/2)TiO3-6 mol% BaTiO3.* Journal of Applied Physics, 2011. **110**(7): p. 074106.
80. Noheda, B., et al., *Polarization rotation via a monoclinic phase in the piezoelectric 92% $PbZn_{1/3}Nb_{2/3}O_3$-8% $PbTiO_3$.* Physical Review Letters, 2001. **86**(17): p. 3891-3894.
81. Bai, F., J. Li, and D. Viehland, *Domain engineered states over various length scales in (001)-oriented Pb(Mg[sub 1 ⁄ 3]Nb[sub 2 ⁄ 3])O[sub 3]-x%PbTiO[sub 3] crystals: Electrical history dependence of hierarchal domains.* Journal of Applied Physics, 2005. **97**(5): p. 054103.
82. Zhang, Q.H., et al., *Crystal growth and electric properties of lead-free NBT-BT at compositions near the morphotropic phase boundary.* Physica Status Solidi a-Applications and Materials Science, 2011. **208**(5): p. 1012-1020.
83. Xu, G., et al., *Electric-field-induced redistribution of polar nano-regions in a relaxor ferroelectric.* Nat Mater, 2006. **5**(2): p. 134-40.
84. Kling, J., et al., *A-site occupancy in the lead-free (Bi[sub 1/2]Na[sub 1/2]TiO[sub 3])[sub 0.94]–(BaTiO[sub 3])[sub 0.06] piezoceramic: Combining first-principles study and TEM.* Journal of Applied Physics, 2010. **107**(11): p. 114113.
85. Elkechai, O., M. Manier, and J.P. Mercurio, *Na0.5Bi0.5TiO3–K0.5Bi0.5TiO3 (NBT-KBT) system: A structural and electrical study.* Physica Status Solidi (a), 1996. **157**(2): p. 499-506.
86. Kreisel, J., et al., *An x-ray diffraction and Raman spectroscopy investigation of A-site substituted perovskite compounds: the (Na1-xKx)0.5Bi0.5TiO3(0lexle1) solid solution.* Journal of Physics: Condensed Matter, 2000. **12**(14): p. 3267-3280.
87. Yi, X., et al., *Flux growth and characterization of lead-free piezoelectric single crystal [Bi0.5(Na1−xKx)0.5]TiO3.* Journal of Crystal Growth, 2005. **281**(2-4): p. 364-369.
88. Zhang, H.W., et al., *Enhanced ferroelectric properties and thermal stability of nonstoichiometric 0.92(Na0.5Bi0.5)TiO3-0.08(K0.5Bi0.5)TiO3 single crystals.* Applied Physics Letters, 2013. **103**(21): p. 212906.
89. Zhang, S., C.A. Randall, and T.R. Shrout, *Recent developments in high curie temperature perovskite single crystals.* IEEE Trans Ultrason Ferroelectr Freq Control, 2005. **52**(4): p. 564-9.
90. Dorcet, V. and G. Trolliard, *A transmission electron microscopy study of the A-site disordered perovskite Na0.5Bi0.5TiO3.* Acta Materialia, 2008. **56**(8): p. 1753-1761.
91. Yao, J., et al., *Hierarchical domains in Na[sub 1/2]Bi[sub 1/2]TiO[sub 3] single crystals: Ferroelectric phase transformations within the geometrical restrictions of a ferroelastic inheritance.* Applied Physics Letters, 2010. **96**(22): p. 222905.
92. Viehland, D.D. and E.K.H. Salje, *Domain boundary-dominated systems: adaptive structures and functional twin boundaries.* Advances in Physics, 2014. **63**(4): p. 267-326.

93. Gruverman, A., et al., *Vortex ferroelectric domains.* Journal of Physics-Condensed Matter, 2008. **20**(34): p. 342201.
94. Schilling, A., et al., *Domains in ferroelectric nanodots.* Nano Lett, 2009. **9**(9): p. 3359-64.
95. Catalan, G., et al., *Domain wall nanoelectronics.* Reviews of Modern Physics, 2012. **84**(1): p. 119-156.
96. Arlt, G. and P. Sasko, *Domain Configuration and Equilibrium Size of Domains in Batio3 Ceramics.* Journal of Applied Physics, 1980. **51**(9): p. 4956-4960.
97. Ge, W.W., et al., *Direct evidence of correlations between relaxor behavior and polar nano-regions in relaxor ferroelectrics: A case study of lead-free piezoelectrics Na0.5Bi0.5TiO3-x%BaTiO3.* Applied Physics Letters, 2013. **103**(24): p. 241914.
98. Ge, W., et al., *Ultrahigh electromechanical response in (1−x)(Na0.5Bi0.5)TiO3-xBaTiO3 single-crystals via polarization extension.* Journal of Applied Physics, 2012. **111**(9): p. 093508.
99. Haun, M.J., et al., *Thermodynamic theory of the lead zirconate-titanate solid solution system.* Ferroelectrics, 1989. **94**(1): p. 313-313.
100. Zhang, S.J. and F. Li, *High performance ferroelectric relaxor-PbTiO3 single crystals: Status and perspective.* Journal of Applied Physics, 2012. **111**(3): p. 031301.
101. Zhang, S.J., et al., *Characterization of Pb(In1/2Nb1/2)O-3-Pb(Mg1/3Nb2/3)O-3-PbTiO3 ferroelectric crystal with enhanced phase transition temperatures.* Journal of Applied Physics, 2008. **104**(6): p. 064106.
102. Zhang, Y.Y., et al., *The compositional segregation, phase structure and properties of Pb(In1/2Nb1/2)O-3-Pb(Mg1/3Nb2/3)O-3-PbTiO3 single crystal.* Journal of Crystal Growth, 2011. **318**(1): p. 890-894.
103. Li, F., et al., *Electromechanical properties of tetragonal Pb(In1/2Nb1/2)O-3-Pb(Mg1/3Nb2/3)O-3-PbTiO3 ferroelectric crystals.* Journal of Applied Physics, 2010. **107**(5): p. 054107.
104. Zhang, Y., et al., *Complete Set of Material Constants of (011)-Poled Rhombohedral Single-Crystal 0.25Pb(In1/2Nb1/2)O3-0.47Pb(Mg1/3Nb2/3)O3-0.28PbTiO3.* Journal of Electronic Materials, 2010. **40**(1): p. 92-96.
105. Zhao, P., et al., *The strength of PIN-PMN-PT single crystals under bending with a longitudinal electric field.* Smart Materials & Structures, 2011. **20**(5): p. 055006.
106. Dong, W.D., et al., *Giant electro-mechanical energy conversion in [011] cut ferroelectric single crystals.* Applied Physics Letters, 2012. **100**(4): p. 042903.
107. Finkel, P., et al., *Phase switching at low field and large sustainable strain output in domain engineered ferroic crystals.* Physica Status Solidi a-Applications and Materials Science, 2012. **209**(11): p. 2108-2113.
108. Wang, W., et al., *Beam-Mode Piezoelectric Properties of Ternary Pb(In1/2Nb1/2)O-3-Pb(Mg1/3Nb2/3)O-3-PbTiO3 Single Crystals for Medical Linear Array Applications.* Journal of Electronic Materials, 2011. **40**(11): p. 2228-2233.
109. Hosono, Y. and Y. Yamashita, *Piezoelectric ceramics and single crystals for ultrasonic medical transducers.* Journal of Electroceramics, 2006. **17**(2-4): p. 577-583.
110. Wang, W., et al., *Broadband ultrasonic linear array using ternary PIN-PMN-PT single crystal.* Rev Sci Instrum, 2012. **83**(9): p. 095001.
111. Wang, Y.J., et al., *Temperature-induced and electric-field-induced phase transitions in rhombohedral Pb(In1/2Nb1/2)O-3-Pb(Mg1/3Nb2/3)O-3-PbTiO3 ternary single crystals (vol 90, 134107, 2014).* Physical Review B, 2014. **90**(17): p. 1.

112. Gehring, P.M., K. Ohwada, and G. Shirane, *Electric-field effects on the diffuse scattering in PbZn1/3Nb2/3O3 doped with 8% PbTiO3.* Physical Review B, 2004. **70**(1): p. 014110.
113. Kleemann, W., *Random-Field Induced Antiferromagnetic, Ferroelectric and Structural Domain States.* International Journal of Modern Physics B, 1993. **7**(13): p. 2469-2507.
114. Cochran, W., *Dynamical, Scattering and Dielectric Properties of Ferroelectric Crystals.* Advances in Physics, 1969. **18**(72): p. 157-&.
115. Foster, C.M., et al., *Anharmonicity of the lowest-frequency A1(TO) phonon in PbTiO3.* Phys Rev B Condens Matter, 1993. **48**(14): p. 10160-10167.
116. Tomeno, I., et al., *Simultaneous softening of acoustic and optical modes in cubic PbTiO${}_{3}$.* Physical Review B, 2012. **86**(13): p. 134306.
117. Hirota, K., et al., *Neutron diffuse scattering from polar nanoregions in the relaxor Pb(Mg1/3Nb2/3)O-3.* Physical Review B, 2002. **65**(10): p. 104105.
118. Stock, C., et al., *Neutron and x-ray diffraction study of cubic [111] field-cooled Pb(Mg1/3Nb2/3)O-3.* Physical Review B, 2007. **76**(6): p. -.
119. Singh, A.K. and D. Pandey, *Evidence for M-B and M-C phases in the morphotropic phase boundary region of (1-x)[Pb(Mg1/3Nb2/3)O-3]-xPbTiO(3): A Rietveld study.* Physical Review B, 2003. **67**(6): p. 12.
120. Setyawan, W. and S. Curtarolo, *High-throughput electronic band structure calculations: Challenges and tools.* Computational Materials Science, 2010. **49**(2): p. 299-312.
121. Acosta, M., et al., *Piezoelectricity and rotostriction through polar and non-polar coupled instabilities in bismuth-based piezoceramics.* Scientific Reports, 2016. **6**: p. 8.
122. Gehring, P.M., S. Park, and G. Shirane, *Soft phonon anomalies in the relaxor ferroelectric Pb(Zn(1/3)Nb(2/3))0.92Ti0.08O3.* Phys Rev Lett, 2000. **84**(22): p. 5216-9.
123. Soukhojak, A.N., et al., *Superlattice in single crystal barium-doped sodium bismuth titanate.* Journal of Physics and Chemistry of Solids, 2000. **61**(2): p. 301-304.
124. Xu, G., et al., *Phase instability induced by polar nanoregions in a relaxor ferroelectric system.* Nat Mater, 2008. **7**(7): p. 562-6.
125. Zhang, H.W., et al., *Neutron diffuse scattering of (1-x)(Na0.5Bi0.5)TiO3-xBaTiO(3) relaxor ferroelectric single crystals.* Scripta Materialia, 2014. **86**: p. 5-8.
126. Gehring, P.M., *Neutron Diffuse Scattering in Lead-Based Relaxor Ferroelectrics and Its Relationship to the Ultra-High Piezoelectricity.* Journal of Advanced Dielectrics, 2012. **02**(02): p. 1241005.
127. Xu, G.Y., et al., *Neutron elastic diffuse scattering study of Pb(Mg1/3Nb2/3)O-3.* Physical Review B, 2004. **69**(6): p. 064112.
128. Deng, G.C., et al., *Dynamical mechanism of phase transitions in A-site ferroelectric relaxor (Na1/2Bi1/2) TiO3.* Physical Review B, 2014. **90**(13).
129. Yao, J.J., et al., *Role of coexisting tetragonal regions in the rhombohedral phase of Na0.5Bi0.5TiO3-xat.%BaTiO3 crystals on enhanced piezoelectric properties on approaching the morphotropic phase boundary.* Applied Physics Letters, 2012. **100**(1).
130. Laijun, L., et al., *Structure and dielectric dispersion in cubic-like 0.5K 0.5 Na 0.5 NbO 3 - 0.5Na 1/2 Bi 1/2 TiO 3 ceramic.* EPL (Europhysics Letters), 2016. **114**(4): p. 47011.
131. Gehring, P.M., et al., *Soft mode dynamics above and below the Burns temperature in the relaxor Pb(Mg1/3Nb2/3)O3.* Phys Rev Lett, 2001. **87**(27 Pt 1): p. 277601.
132. Swainson, I.P., et al., *Soft phonon columns on the edge of the Brillouin zone in the relaxor PbMg1/3Nb2/3O3.* Physical Review B, 2009. **79**(22): p. -.
133. Stock, C., et al., *Damped soft phonons and diffuse scattering in 40%Pb(Mg1/3Nb2/3)O-3-60%PbTiO3.* Physical Review B, 2006. **73**(6): p. -.

134. Acosta, M., et al., *Piezoelectricity and rotostriction through polar and non-polar coupled instabilities in bismuth-based piezoceramics.* Sci Rep, 2016. **6**: p. 28742.